INTEGRATION OF PHOTOSYNTHETIC PIGMENT-PROTEIN COMPLEXES IN DYE SENSITIZED SOLAR CELLS TOWARDS PLASMONIC-ENHANCED BIOPHOTOVOLTAICS

by

YIQUN YANG

B. Eng., Jiangnan University, China, 2008
M.S., Jiangnan University, China, 2011

AN ABSTRACT OF A DISSERTATION

submitted in partial fulfillment of the requirements for the degree

DOCTOR OF PHILOSOPHY

Department of Chemistry
College of Arts and Sciences

KANSAS STATE UNIVERSITY
Manhattan, Kansas

2016

Abstract

Solar energy as a sustainable resource is a promising alternative to fossil fuels to solve the tremendous global energy crisis. Development of three generation of solar cells has promoted the best sunlight to electricity conversion efficiency above 40%. However, the most efficient solar cells rely on expensive nonsustainable raw materials in device fabrication. There is a trend to develop cost-effective biophotovoltaics that combines natural photosynthetic systems into artificial energy conversion devices such as dye sensitized solar cells (DSSCs). In this research, a model system employs natural extract light-harvesting complex II (LHCII) as a light-absorbing sensitizer to interface with semiconductive TiO_2 and plasmonic nanoparticles in DSSCs. The goal of this research is to understand the fundamental photon capture, energy transfer and charge separation processes of photosynthetic pigment-protein complexes along with improving biophotovoltaic performance based on this model system through tailoring engineering of TiO_2 nanostructures, attaching of the complexes, and incorporating plasmonic enhancement.

The first study reports a novel approach to linking the spectroscopic properties of nanostructured LHCII with the photovoltaic performance of LHCII-sensitized solar cells (LSSCs). The aggregation allowed reorganization between individual trimers which dramatically increased the photocurrent, correlating well with the formation of charge-transfer (CT) states observed by absorption and fluorescence spectroscopy. The assembled solar cells demonstrated remarkable stability in both aqueous buffer and acetonitrile electrolytes over 30 days after LHCII being electrostatically immobilized on amine-functionalized TiO_2 surface.

The motivation of the second study is to get insights into the plasmonic effects on the nature of energy/charge transfer processes at the interface of photosynthetic protein complexes and artificial photovoltaic materials. Three types of core-shell (metal@TiO_2) plasmonic nanoparticles

(PNPs) were conjugated with LHCII trimers to form hybrid systems and incorporated into a DSSC platform built on a unique open three-dimensional (3D) photoanode consisting of TiO_2 nanotrees. Enhanced photon harvesting capability, more efficient energy transfer and charge separation at the LHCII/TiO_2 interface were confirmed in the LHCII-PNP hybrids, as revealed by spectroscopic and photovoltaic measurements, demonstrating that interfacing photosynthesis systems with specific artificial materials is a promising approach for high-performance biosolar cells.

Furthermore, the final study reveals the mechanism of hot electron injection by employing a mesoporous core-shell (Au@TiO_2) network as a bridge material on a micro-gap electrode to conduct electricity under illumination and comparing the photoconductance to the photovolatic properties of the same material as photoanodes in DSSCs. Based on the correlation of the enhancements in photoconductance and photovoltaics, the contribution of hot electrons was deconvoluted from the plasmonic near-field effects.

INTEGRATION OF PHOTOSYNTHETIC PIGMENT-PROTEIN COMPLEXES IN DYE SENSITIZED SOLAR CELLS TOWARDS PLASMONIC-ENHANCED BIOPHOTOVOLTAICS

by

YIQUN YANG

B. Eng., Jiangnan University, China, 2008
M.S., Jiangnan University, China, 2011

A DISSERTATION

submitted in partial fulfillment of the requirements for the degree

DOCTOR OF PHILOSOPHY

Department of Chemistry
College of Arts and Sciences

KANSAS STATE UNIVERSITY
Manhattan, Kansas

2016

Approved by:

Major Professor
Dr. Jun Li

Copyright

Abstract

Solar energy as a sustainable resource is a promising alternative to fossil fuels to solve the tremendous global energy crisis. Development of three generation of solar cells has promoted the best sunlight to electricity conversion efficiency above 40%. However, the most efficient solar cells rely on expensive nonsustainable raw materials in device fabrication. There is a trend to develop cost-effective biophotovoltaics that combines natural photosynthetic systems into artificial energy conversion devices such as dye sensitized solar cells (DSSCs). In this research, a model system employs natural extract light-harvesting complex II (LHCII) as a light-absorbing sensitizer to interface with semiconductive TiO_2 and plasmonic nanoparticles in DSSCs. The goal of this research is to understand the fundamental photon capture, energy transfer and charge separation processes of photosynthetic pigment-protein complexes along with improving biophotovoltaic performance based on this model system through tailoring engineering of TiO_2 nanostructures, attaching of the complexes, and incorporating plasmonic enhancement.

The first study reports a novel approach to linking the spectroscopic properties of nanostructured LHCII with the photovoltaic performance of LHCII-sensitized solar cells (LSSCs). The aggregation allowed reorganization between individual trimers which dramatically increased the photocurrent, correlating well with the formation of charge-transfer (CT) states observed by absorption and fluorescence spectroscopy. The assembled solar cells demonstrated remarkable stability in both aqueous buffer and acetonitrile electrolytes over 30 days after LHCII being electrostatically immobilized on amine-functionalized TiO_2 surface.

The motivation of the second study is to get insights into the plasmonic effects on the nature of energy/charge transfer processes at the interface of photosynthetic protein complexes and artificial photovoltaic materials. Three types of core-shell (metal@TiO_2) plasmonic nanoparticles

(PNPs) were conjugated with LHCII trimers to form hybrid systems and incorporated into a DSSC platform built on a unique open three-dimensional (3D) photoanode consisting of TiO_2 nanotrees. Enhanced photon harvesting capability, more efficient energy transfer and charge separation at the LHCII/TiO_2 interface were confirmed in the LHCII-PNP hybrids, as revealed by spectroscopic and photovoltaic measurements, demonstrating that interfacing photosynthesis systems with specific artificial materials is a promising approach for high-performance biosolar cells.

Furthermore, the final study reveals the mechanism of hot electron injection by employing a mesoporous core-shell (Au@TiO_2) network as a bridge material on a micro-gap electrode to conduct electricity under illumination and comparing the photoconductance to the photovolatic properties of the same material as photoanodes in DSSCs. Based on the correlation of the enhancements in photoconductance and photovoltaics, the contribution of hot electrons was deconvoluted from the plasmonic near-field effects.

Table of Contents

List of Figures

List of Tables

List of Abbreviations

AuNS	Gold Nanosphere
AgNS	Silver Nanosphere
AgNP	Silver Nanoplate
AFM	Atomic Force Microscopy
APTES	3-Aminopropyltriethoxysilane
Chl	Chlorophyll
CT	Charge Transfer
CB	Conduction Band
DSSC	Dye Sensitized Solar Cell
ESC	Effective Surface Coverage
ET	Energy Transfer
FF	Fill Factor
FTO	Fluorine Doped Oxide
FESEM	Field Emission Scan Electron Microscopy
HB	Hold-Burning
HRTEM	High-Resolution Transmission Electron Microscopy
IPCE	Incident Photon-to-Current Efficiency
ICP-AES	Inductively Coupled Plasma-Atomic Emission Spectrometer
J_{SC}	Short Circuit Current
LHC	Light Harvesting Complex
LSSC	LHCII Sensitized Solar Cell
NPQ	Non-Photochemical Quenching

NHE	Normal Hydrogen Electrode
NW	Network
N3	(cis-Bis(isothiocyanato) bis(2,2’-bipyridyl-4,4’-dicarboxylato ruthenium(II))
N719	(Di-tetrabutylammonium cis-bis(isothiocyanato)bis(2,2’-bipyridyl-4,4’-dicarboxylato)ruthenium(II))
N749	(4,4’,4”-Tricarboxy-2,2’,6’,2’-terpyridine)tris(isocyanato)Ru(II)).
NTFB	Nitrosonium Tetrafluoroborate
PV	Photovoltaic
PCE	Power Conversion Efficiency
PS	Photosystem
PNP	Plasmonic Nanoparticle
P_{max}	Maximum Output Power
PIRET	Plasmon-Induced Resonance Energy Transfer
RC	Reaction Center
R_{SH}	Shunt Resistance
R_S	Series Resistance
SPR	Surface Plasmonic Resonance
TTIP	Titanium Tetrasioproxide
TLD	Through Lens Detector
TCSPC	Time-Correlated Single Photon Counting
V_{OC}	Open Circuit Voltage
*v*CD	Low Voltage High Contrast Detector
WSCP	Water Soluble Chlorophyll-Binding Protein

Acknowledgements

Five years of Ph.D. study is like a sailing on the ocean, and it would not have been possible to make a successful landing without the guidance and supports from professors, families and friends.

First and foremost, I would like to express my special appreciation and thanks to my advisor Professor Dr. Jun Li for his tremendous academic support throughout my Ph.D. career. His meticulous and rigorous attitude towards science impacts me a lot, and helps me to become a professional research scientist. I would also like to thank my supervisory committee members, Dr. Ryszard Jankowiak, Dr. Takashi Ito and Dr. James Edgar for attending my oral proposition, and final defense, spending time reading and revising my thesis, and for their helpful advice and encouragement. Special mention goes to Dr. Ryszard Jankowiak and his German collaborators for providing the samples and teaching the basics of photosynthetic proteins, to Dr. Dan Higgins for his support in fluorescence and AFM measurements, and to our collaborator Dr. Francis D'souza for his input and valuable discussions in the plasmon-enhanced bio-solar cell project.

Special thanks go to all former and present Li group members: Dr. Yifen Li, Dr. Luxi Zhang Swisher, Dr. Foram Madiyar, Dr. Steven Klankowski, Dr. Gaind Pandey, Yichen Zheng, Tao Liu, and Dr.Yueping Fang. This group has been a source of friendships as well as good advice and collaboration. Many thanks to my friends: Hao Xu, Hongfu Luo, and Zi Li, for the helps in my daily life and being my travel buddies to many places of interest. Additionally, I very much appreciate several people at Chemistry Department of, especially, Tobe Eggers, Ron Jackson, Jim Hodgson, Dr. Tingting Liu, Leila Maurmann, Mary Dooley, and Kim Ross.

I gratefully acknowledge the funding support from NSF EPSCoR Award EPS-0903806, NASA grant NNX13AD42A and the matching fund provided by the State of Kansas that made my

Ph.D. work possible. I would also like to thank Chemistry department for providing the Graduate Teaching Assistantship. It was wonderful to work with Michael Hinton and Dr. Tingting Liu during my teaching duties.

Finally, my deep heartfelt appreciation goes to all my families, especially my Mom, Dad and husband. I cannot be what I am today without their encouragement, understanding and support. Thank you Mom for taking care of me and our little Eric during my hard time for graduation preparation. And to my darling Eric for being such a nice little baby that past five months, and making it possible for me to complete the program.

Dedication

“To my parents Qing Yang & Ning Ye and loved ones.”

Preface

The dissertation comprises of the following major sections:

Chapter 1 – This chapter briefly introduces global energy crisis and solar energy as one of anticipative renewable resources which motivate the development of solar cells. Then it gives introduction of the working principle of the dye sensitized solar cell (DSSC), referring to the photosynthetic pigment-protein complexes as potential photosensitizer alternatives and the surface plasmonic effects on photovoltaic enhancement, followed by illustrations of measurements and terminologies related to photovoltaic characterization.

Chapter 2 – This chapter describes the preparation of TiO_2 as the photoanode material of DSSCs. The TiO_2 is specifically prepared into three morphologies, i.e. planar thin film, vertically aligned nanotree array and Au@TiO_2 core-shell network, for the applications in chapters 3 to 5, respectively, and the advantage of each morphology is discussed.

Chapter 3 – An accepted paper, published in *Physical Chemistry Chemical Physics*. This study is about employing light-harvesting complex II (LHCII) as light antenna in the thin-film sensitized TiO_2 solar cell (so-called LHCII sensitized solar cell, LSSC). The photovoltaic behavior of LHCII has been demonstrated, and the photocurrent improved by the charge transfer (CT) states due to the formation of LHCII aggregates are discussed correlated to the spectroscopy results.

Chapter 4 – An accepted paper, published in *Advanced Materials Interfaces*. This chapter focuses on the interplay between LHCII and plasmonic nanoparticles (PNPs). Enhanced photon harvesting capability and more efficient charge separation at the LHCII/TiO_2 interface have been demonstrated in the LHCII-PNP hybrids, leading to a more efficient LSSC built on three-dimensional TiO_2 nanotree photoanode with the core-shell metal@TiO_2 PNPs incorporated. This

work provides new insights into the plasmonic effects on the nature of energy/charge transfer processes at the interface of photosynthetic protein complexes and artificial photovoltaic materials.

Chapter 5 – A manuscript, submitted to *Applied Physics Letter*. In this work, the hot electron injection from metal NP to semiconductor are revealed based on the photoconductivity measurements performed on a micro-gap electrode with the synthesized core-shell Au@TiO_2 network and correlated with the photovoltaic characterizations of the corresponding DSSC.

Finally, **Chapter 6** concludes the main findings of this work and proposes the future prospects of biophotovoltaics. Appendix includes the supporting information for the discussed sections and some preliminary results for the prospective studies.

Chapter 1 - Introduction

1.1 Energy Crisis and Solar Energy

An ever growing demand for energy crisis is one of the greatest challenges to economic growth and climate change of our era. Fossil fuels, namely coal, petroleum and natural gas, are finite resources but dominate the worldwide energy supplies for hundred years. The energy crisis can be traced back to 1970's oil embargo; it has never ceased since.[1] According to the US Energy Information Administration (EIA), until 2014, at least 80 percent of total U.S. energy consumption still relied on three fossil fuel sources (Figure 1.1A).[2] At the same time, over combustion of fossil fuels causes an unbearable burden on environment; it is the main "culprit" causing global warming. It was responsible for the majority of energy-related greenhouse gas emissions on a carbon dioxide equivalent basis in 2013 (Figure 1.1B).[3] The total energy consumption keeps increasing, especially with the rising energy demand of developing countries such as China and India. The tremendous pollution and severe hazy weather associated with the use of fossil fuels have occurred in many areas of these countries. Discovering sustainable and environment-friendly energy sources becomes obligatory.

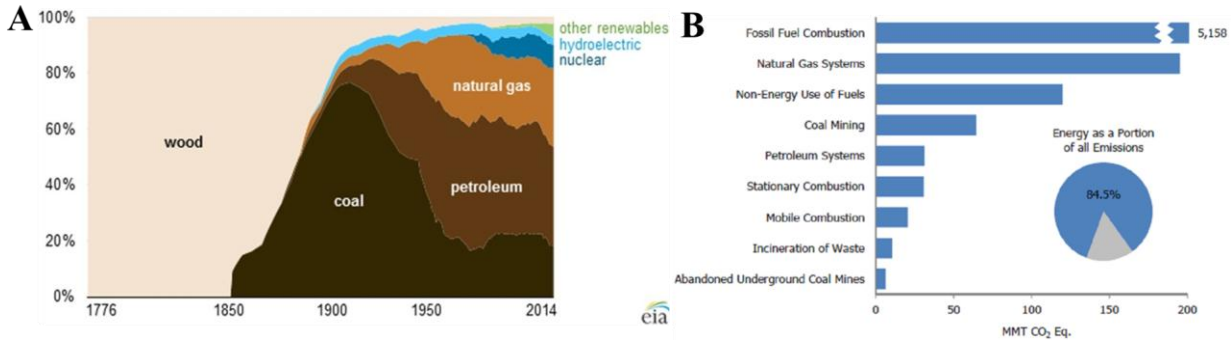

Figure 1.1 Energy consumption and greenhouse gas sources.

(A) Shares of energy consumption in United States (1777-2014). (Reprinted with permission from ref. 2. Copyright © 2015 EIA) (B) 2013 Energy chapter greenhouse gas sources: Emissions values are presented in units of million metric tons of carbon dioxide equivalent

(MMT CO_2 Eq.). (Reprinted with permission from ref. 3. Copyright © 2015 U.S. Environmental Protection Agency)

The prospect of using renewable energy, mainly based on wind, water and solar resources, to replace the traditional fuels for electricity generation has been projected, and the solar resource is highlighted for its abundant energy supply each year. Figure 1.2 displays the yearly energy supply potentials from the major renewable sources and the total reserves of the finite resources.[4] The solar resource beats all the other renewable and fossil-based energy resources combined, of which the annual energy potential was 1575 ~ 49387 exajoules (EJ, 1 EJ = 278 TWh) stated in 2000 World Energy Assessment, several times larger than the total world energy consumption which was 559.8 EJ in 2012.[5-6] Solar power is highly appealing for electricity generation because it is sustainable and free of by-product contamination. How to efficiently convert sun light into electricity is a hot topic of scientific research.

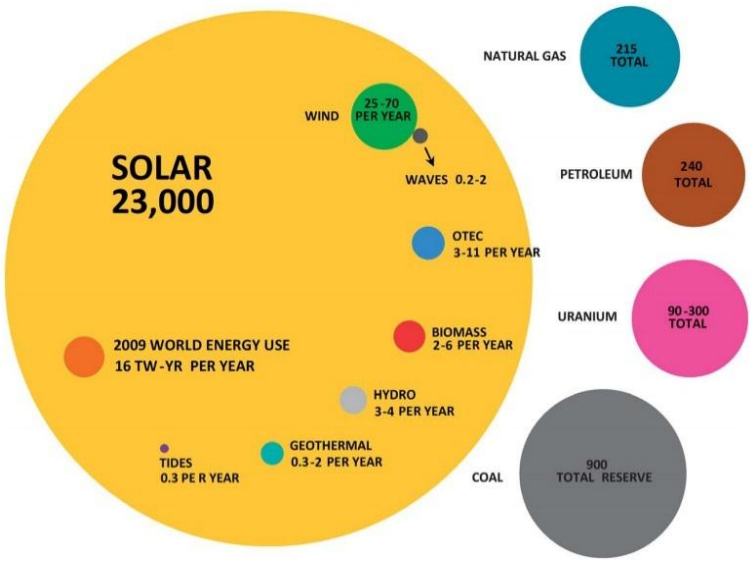

Figure 1.2 Comparing finite and renewable planetary energy reserves (Terawatt-years). Total recoverable reserves are shown for the finite resources. Yearly potential is shown for the renewables. (Reprinted with permission from ref. 4. Copyright © 2013 Royal Society of Chemistry)

1.2 Development of Solar Cells: Photovoltaic Generations

The systems to harvest incident sun light and convert it into electrical energy are photovoltaic devices, so-called solar cells, in which the photocurrent is generated through charge separation and collection of free electron and hole under solar irradiation. The portfolio of solar cells consists of a number of established and emerging technologies, employs different semiconductive and photosensitive materials, and involves three generations of which the updated best research-cell efficiencies are plotted in Figure 1.3.

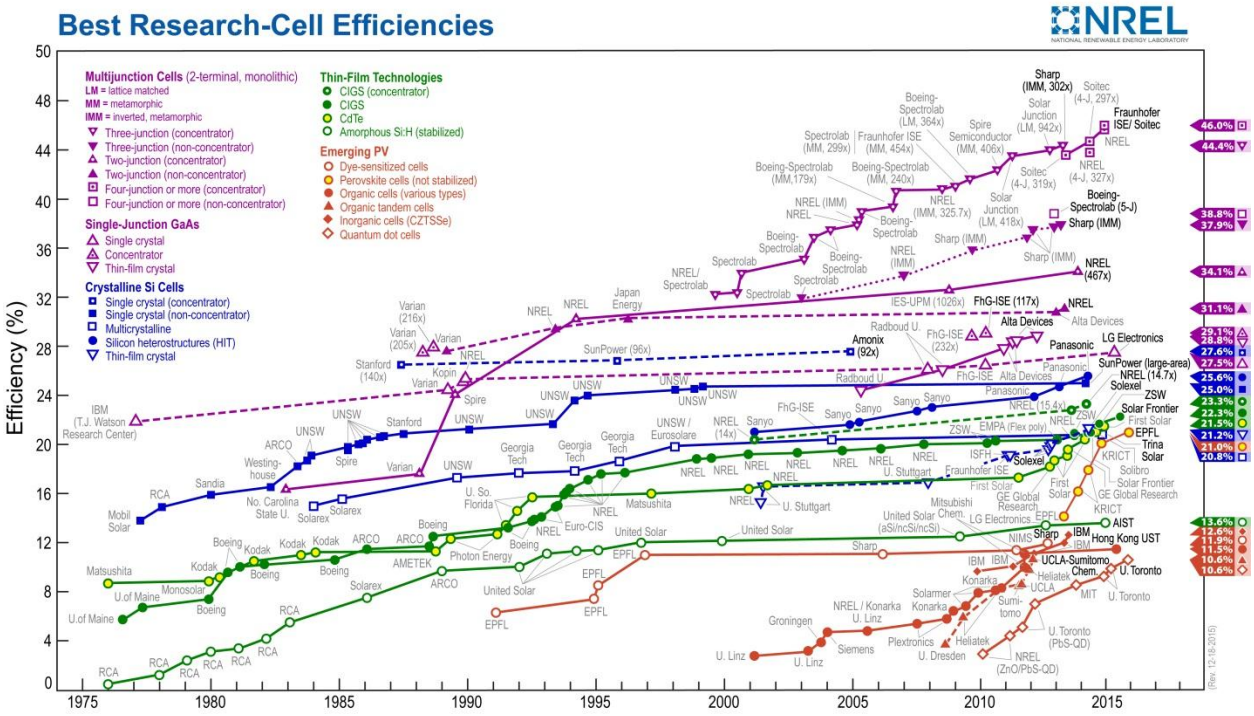

Figure 1.3 Best efficiencies obtained for research photovoltaic cells since 1975.

(Reprinted with permission from National Renewable Energy Laboratory (NREL). Copyright © 2016 NREL)

Solar cells based on silicon, that come in wafer-like monocrystalline, polycrystalline and amorphous forms, are categorized as the first generation. They are usually doped with phosphorus and boron in a P-N junction to achieve high-efficient charge separation of electron-hole pairs.

These solar cells demonstrate a good performance with more than 20% of the power conversion efficiency (PCE) as well as high stability, which currently dominate the markets, accounting for around 80% of the global share. Multi-junction cells, also named tandem cells, cooperating with concentrated solar power systems, raise the best laboratory-reported PCE above 40% to date. The cost of the first-generation solar cells keep decreasing with the development of manufacturing techniques and the surge in production volumes of silicon wafers.[7] However, they are rigid, and usually lose some efficiency under higher temperature or imperfect illumination angle, which restrain their applications.

The second-generation solar cells, thin film solar cells, are composed of amorphous silicon, cadmium telluride (CdTe), and copper indium gallium diselenide (CIGS), and have outstanding performance, as high as 20% PCE. They are made from layers of semiconductive materials with only a few micrometers thick that can make devices flexible and reduce the production cost. However, this technique is still limited by vacuum processes and high temperature treatments in manufacturing, and also restricted by resource scarcity.[8]

The emerging solar cells employing organic dye,[9-12] quantum dots,[13-16] conductive polymers[17-20] and perovskite materials[21-24] with new photovoltaic mechanisms are assigned into the third-generation solar cells, which are currently under laboratory investigations. Among this generation, dye sensitized solar cells (DSSCs) have many advantages over traditional silicon-based counterparts, such as low cost, mechanical robustness, and ability to operate under imperfect irradiation conditions. More importantly, the hybrid structure of DSSCs separates the charge transport from charge separation which reduces the efficiency loss by electron recombination. The structure and working principle of DSSCs will be discussed in details in the following section. Recently, perovskite solar cells evolving from DSSCs became competitive promising with an

unprecedented growth in PCE from 3.8% to more than 20% in less than 5 years. The perovskite thin film can also be used as top coating in tandem cells and improve the performance of the original solar cells with much lower extra cost.[25-26] Overall, the third-generation solar cells are promising for commercialization because of their low-cost, readily available source materials and low energy expenditure in fabrication. However, the reproducibility and the long-term stability of these solar cells are still the major concerns.

1.3 Dye Sensitized Solar Cells

The integral architecture of DSSCs was first proposed by Grätzel and O`Regan in 1991.[9] Since then improvement in device designs along with the surge in new materials for light absorbing sensitizers (i.e. dye molecules) and redox electrolytes have further improved their performance. Based on the NREL statistics in Figure 1.3, the highest lab-recorded efficiency of DSSCs to date is about 12%. Even though their efficiencies are still lower than the first- and second-generation cells, the fabrication of DSSCs is cost-effective by utilizing inexpensive and abundant wide-bandgap semiconductive materials in the photoanodes, such as Titania (TiO_2) and Zinc oxide (ZnO). However, these materials are inert to visible light, and thus need to be hybridized with electron transfer dye molecules that have large absorption coefficient in visible range. Some emerging solar cells have adopted a hybrid structure of DSSCs, such as quantum dots sensitized solar cells[27-28] and perovskite sensitized solar cells[29-30]. Quantum dots, perovskite crystals or the photosynthetic pigment-protein complexes as discussed in this dissertation are employed as novel light-absorbing sensitizers to replace the organic dye, and their fundamental properties involving photon capture, energy transfer and charge separation processes can be addressed straightforwardly based on the platform of DSSC.

1.3.1 Structure and Operation Principle

The traditional DSSC is constructed in a sandwich configuration (Figure 1.4).[31] A wide bandgap semiconductor layer (typically a mesoporous film made of sintered TiO_2 nanoparticles) is sensitized with a visible light absorbing organic dye and forms the core of the device which is deposited on a fluorine doped tin oxide (FTO) coated glass as photoanode. A platinized FTO coated glass is applied as cathode (i.e. counter electrode). An electrolyte usually containing iodine/triiodine (I^-/I_3^-) redox species in organic solvent is filled in between the photoanode and the cathode, serving as mediators for hole transport and dye regeneration.

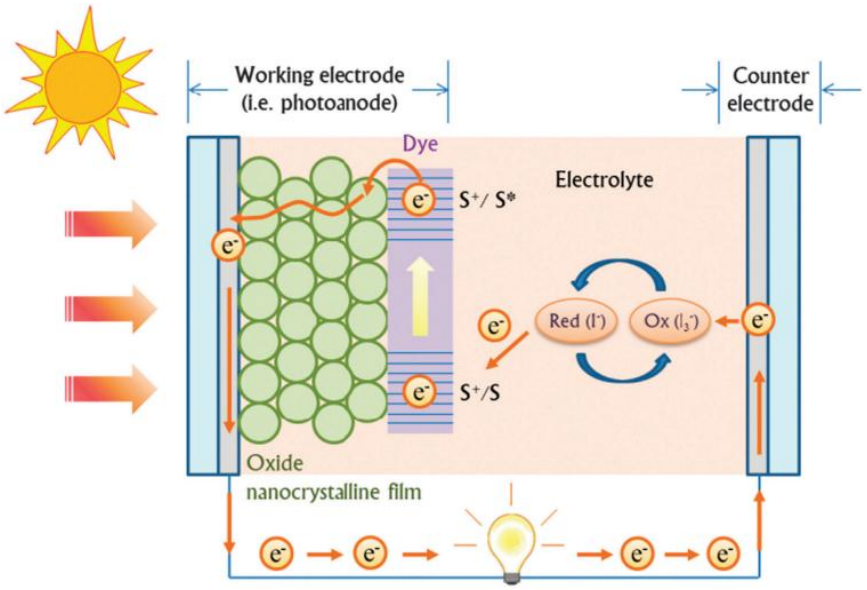

Figure 1.4 Structure and operating mechanism of a DSSC.[31]
(Image adapted from ref. 31. Copyright © 2012 Royal Society of Chemistry)

DSSC is a mimic of natural photosynthesis to convert sunlight into electricity. The operation principle of DSSCs differs from the conventional P-N junction based solar cells. Briefly, the photosynthesis processes take place in the chloroplast where solar energy is absorbed by the pigments (such as chlorophylls (Chls)) in the photosystems (PSs) and converted into electrons in the reaction centers (RCs) to trigger a series of chemical reactions.[32] In DSSCs, the dye molecules

similar to the Chls in green leaves are excited by absorbing visible light. In contrast to conventional P-N junction solar cells, the charge separation occurs at the sensitizer/TiO_2 interface by injecting electrons from the excited dye molecules into the TiO_2 layer to generate electrons in analogue to the function of RCs, and then followed by electron diffusion in the TiO_2 network, finally flowing to the cathode through the external circuit as photocurrent. DSSCs utilizes separate media for charge generation (occurs within the dye) and charge transport (occurs in the TiO_2 matrix), which greatly reduces the possibility of charge recombination.[33] Concurrently, the oxidized dye is reduced to its ground state by the oxidation of I^- into I_3^-, then I_3^- will be reduced at the cathode by accepting electrons from the electron flow from photoanode to complete the whole regeneration process. Overall, this system converts solar energy into electricity without any net consumption of chemicals, thus the DSSC can continuous supply power.

1.3.2 Photosynthetic Protein Complexes as Photosensitizers

The capability of light harvesting is directly related to the performance of the solar cells, and an effective photosensitizer for DSSCs requires the following fundamental features. AM1.5 Global curve plotted in Figure 1.5 is defined as the standard solar spectrum for Sun simulation measurements, which shows that the strongest solar power occurs in visible range. In order to capture the most solar energy, an ideal photosensitizer should have broad absorption band with high absorptivity in the same wavelength range. Anchoring groups, such as carboxylate (–COOH), phosphonate ($–H_2PO_3$) or siloxy moiety ($–O–SiR_3$), are preferable for photosensitizer molecules to increase the binding affinity towards oxide semiconductor surface.[34-35] More importantly, the energy level of the excited state of the photosensitizer should be higher than the edge of the conduction band of the semiconductor to ensure an energetically favorable electron transfer.[36] Meanwhile, the redox potential of the photosensitizer should be high enough for the regeneration

by accepting electrons from the redox electrolyte.[36] Finally, the photosensitizer should also have good chemical stability under solar irradiation, heat and electrical actions.

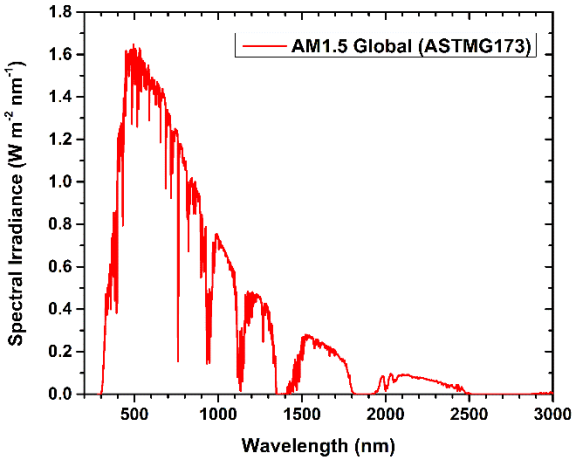

Figure 1.5 The standard One-sun AM1.5G spectrum.

The AM1.5 stands for 1.5 atmosphere thickness, corresponding to a solar zenith angle of z=48.2°; the G stands for global including both direct and diffuse radiation. The spectrum represents the standard irradiance of 100 mW/cm^2 used for photovoltaic characterizations. (Replotted with permission from an online source:

http://rredc.nrel.gov/solar/spectra/am1.5/ASTMG173/ASTMG173.html)

Polybipyridyl ruthenium (Ru) complex dyes are the most common photosensitizers used in DSSCs. Figure 1.6 illustrates the molecular structure of three classic Ru dyes, **N3** (cis-Bis(isothiocyanato) bis(2,2'-bipyridyl-4,4'-dicarboxylato ruthenium(II)), **N719** (Di-tetrabutylammonium cis-bis(isothiocyanato)bis(2,2'-bipyridyl-4,4'-dicarboxylato)ruthenium(II)), and **N749** also named black dye (4,4',4"-tricarboxy-2,2':6',2'-terpyridine)tris(isocyanato)Ru(II)). They are eligible for effective electron transfer photosensitizers and have demonstrated good photovoltaic properties in the DSSCs with the PCE over 10%.[37-39] Considering the limited reserve of Ru in nature, metal-free organic dyes with tailored molecular designs are exploited as substitutes of Ru dyes, which also show good performance in the DSSCs with various redox electrolyte

systems.[40] However, the raw chemicals to synthesize these organic dyes mostly come from petroleum cracking, and it actually deviates from the motivation of sustainability of solar cells.

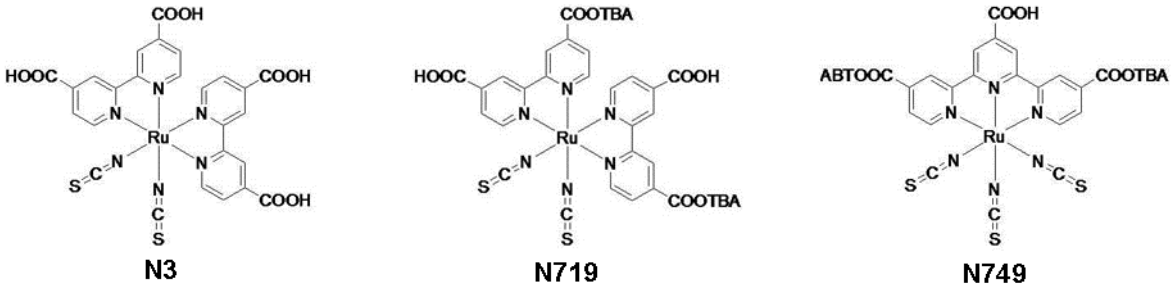

Figure 1.6 Molecular structure of classic Ru-dyes used in DSSCs.

Along the same lines, the natural pigments extracted from plants such as chlorophyll, carotenoid, anthocyanin, flavonoid, cyanine, and tannin have been considered as promising "green" alternative to synthetic dye because they are abundant, low cost, biodegradable and sustainable.[41-42] However, most DSSCs employing natural pigments are much less efficient comparing to the conventional DSSCs using synthesized dyes. In addition, the stability of these plant pigments during DSSC operation is still under debate. The plant pigments are very sensitive to light and heat, and their chemical structures easily mutate or degrade under moisture and atmosphere.[43-44] To avoid degradation, these natural pigments are usually assembled into DSSCs under an inert gas atomosphere,[42] which makes device fabrication more difficult. In addition, due to the relatively weak binding force, desorption of the pigments from metal oxide surface might be another reason that results in a decrease of perfomance in the corresponding DSSCs.[45-46]

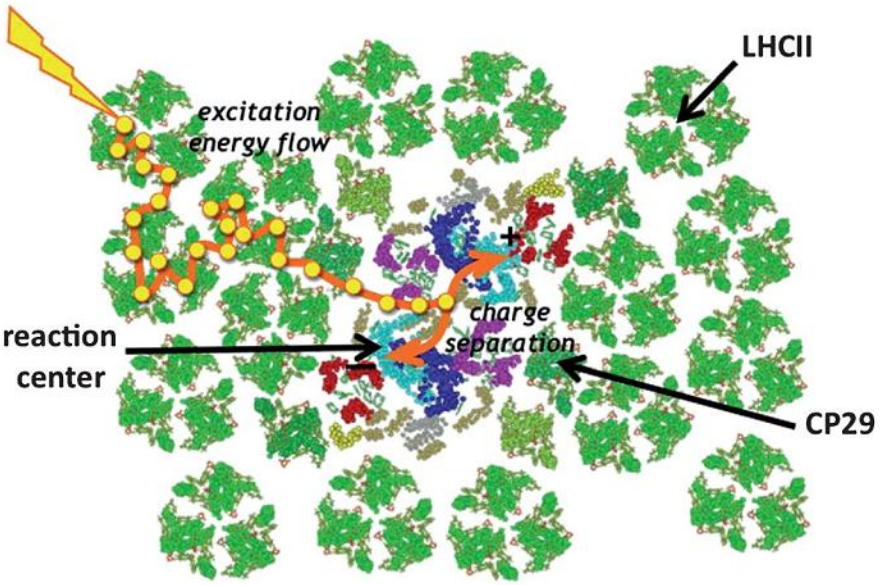

Figure 1.7 Structural organization of light-harvesting complexes and reaction centers in photosystem II.

Excitation energy migrates from the peripheral antenna complexes (i.e. LHCII) to the reaction centers through smaller bridge complexes (i.e. CP29). A potential trajectory of energy flow is shown in orange arrow above. (Reprinted with permission from Ref. 48. Copyright © 2012 Royal Society of Chemistry)

Instead of using pure natural pigments, studies employing photosynthetic protein complexes as photosensitizers in DSSCs are quite encouraging. Photosynthetic protein complexes discovered in plants, bacteria and algae have been reported as essential units for light harvesting, energy transfer and electron transfer in photosynthesis to convert solar energy into life-sustaining chemicals.[47] They are organized into delicate PSs that consist of light-harvesting complexes (LHCs) for photon capture and ultrafast energy transfer, as well as RCs where charge separation and photochemistry take place. Figure 1.7 illustrates the structural organization of LHCs and RCs, and the potential energy transfer pathway in photosystem II (PSII).[48] Comparing with extracted pigments, the pigments in the photosynthetic protein complexes, such as chlorophylls and Carotinoids, are immobilized in the polypepetide network in specific positions and couple with each other. The coupling enables the energy transfer between pigments, which protects them from photodegradation.[49-50] With these advantages, the potential of directly employing photosynthetic

protein complexes in artificial photovoltaic devices as light harvesting antanne was proposed, in attempt to use their extraordinarily efficient light absorption, energy transfer properties, and relatively good stability. Studies have been carried out to utilize the energy transfer processes by directly anchoring RCs[51-52], LHI-RC core complexes[53], or whole PSs (PSI or PSII)[51, 54] on gold electrodes. In a different approach, natural pigments or extracted LHCs have been used as photosensitizers to interface with a ~10 μm-thick mesoporous TiO_2 film or ZnO nanowires in fabricating DSSCs.[45, 55-57]

Overall, the photosynthetic protein complexes based biosolar cells show improved device stability compared to those using pure natural pigments, whereas their conversion efficiency is still much lower than the solar cells based on specifically synthesized photosensitizers. In order to improve the performance of the biosolar cells, it is necessary to tap into the physical processes involving light absorption, energy transfer and charge separation in the photosynthetic protein complexes interfacing with the artificial photovoltaic materials.

1.3.3 Plasmon-Enhanced DSSCs

Nanoparticles (NPs) of noble metals such as gold (Au) and silver (Ag) have been widely applied to enhance photovoltaic and photocatalytic performance accredited to their outstanding light-harvesting and electromagnetic-field concentrating properties.[58-61] Suface plasmonic resonance (SPR) effect accompanied with a strong localized field can be generated around the noble metal NPs when they are exposed to an incident light of which the wavelength is much larger than the size of the NPs (usually the NPs should be smaller than 200 nm). A relatively uniform electromagnetic field provided by the incident light gives rise to a collective oscillation of the free electrons in the noble metal NPs (Figure 1.8).[62] SPR effect will happen at certain wavelength where the oscillation frequency of the free electons is resonant with the frequency of the electromagnetic

field of the incident light. The plasmonic absorptions of plasmonic nanoparticles (PNPs) strongly depend on the particle size, shape and composition, the coupling between particles and the surrounding dielectric environment. [62-65]

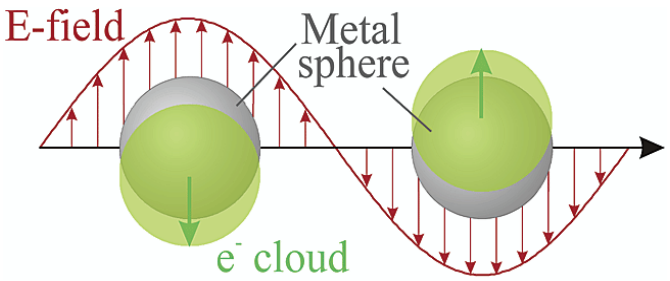

Figure 1.8 Surface plasmonic resonance in noble metal nanoparticles.

Schematic of plasmon oscillation for a metal sphere, showing the displacement of the conduction electron charge cloud relative to the nuclei. Surface plasmonic resonance occurs when the collective oscillation of surface electrons is resonant with the incident light at a specific wavelength. (Image adapted from ref. 65. Copyright © 2003 American Chemical Society)

The SPR effect dramatically affects the absorption and emission properties of the nearby dye molecules.[66-68] Incorporation of PNPs in DSSCs has been proved to improve photocurrent generation and thereby enhance the overall photovoltaic performance.[69-71] The PNP is a light-harvesting booster and concentrator with a strong localized field, that facilitates the dye excitation and photocarrier generation.[72] The thickness of photoanodes can be reduced without sacrifice of PCE by simply blending 0.1~1 wt% PNPs with primary photoanode materials, which allows to lower the manufaturing cost.[73] Moreover, as shown in Figure 1.9, the plasmon-enhanced DSSC with thinner photoanode has higher electron collection efficiency ascribed to the shorter diffusion length, which avoids the potential energy loss caused by the electron recombination.[73]

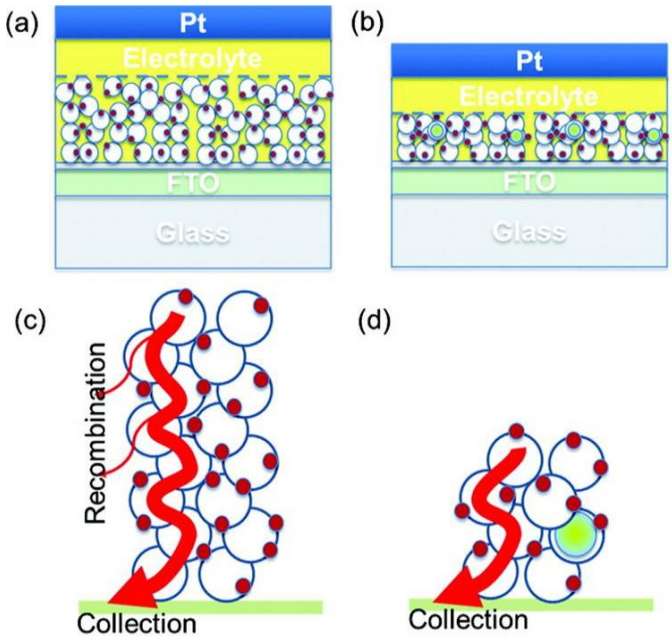

Figure 1.9 Structures and electron collection of conventional and plasmon-enhanced DSSCs. Device structures of conventional DSSCs (a) and plasmon-enhanced DSSCs with thinner photoanode (b); Illustration of photogenerated electron collection in conventional DSSCs (c) and plasmon-enhanced DSSCs (d). (Image copied with permission from ref. 76. Copyright © 2011 American Chemical Society)

There have been many efforts to fabricate more efficient plasmon-enhanced DSSCs with various combinations of tailor-synthesized PNPs and photosensitizers. However, the plausible mechanisms of SPR effect on photovoltaic properties are waiting for solid verifications. It is essential to study the interplay between photosensitizers and PNPs through advanced spectroscopic techniques in conjunction with photovoltaic characterizations.

1.4 Characterizations and Terminologies of Photovoltaic Devices

A number of systematic electrochemistry analysis methods and techniques have been developed to evaluate the performance of photovoltaic cells. In this section, the terminologies, relevant calculations and physical meanings of the characteristic parameters will be illustrated through the data measured from the conventional ruthenium-DSSCs fabricated in our lab. Also,

the theory associated with a technique and the relevant experimental setup will be addressed in each sub-section.

1.4.1 Setup for Photovoltaic Measurements

To evaluate the photovoltaic performance of the as-prepared solar cells, a well aligned illumination system and two potentiostats for electrochemical characterizations were set up in our lab. All components were from Newport Corporation (Irvine, CA) unless otherwise stated. The illumination of full solar spectrum was provided by a Sun simulator using a 300 W Xenon Arc lamp with an AM1.5G filter, the power density of which was carefully calibrated to one-Sun (100 mW/cm^2) with a thermal power meter (Thorlabs， Newton, NJ) and a commercial silicon reference cell (PV Measurements, Boulder, CO). The illumination of monochromatic light was facilitated by a 75 W Xenon Arc Lamp with a motorized monochromator, and the power density at each wavelength was measured by a monochromatic power sensor. A CHI 440A potentiostat (CH Instruments, Austin, TX) was used for current vs. voltage bias measurements, and a PARSTAT 2273 potentiostat (Princeton Applied Research, Oak Ridge, TN) was utilized for impedance measurements. Figure 1.10 displays the layout of the Sun simulator in the lab.

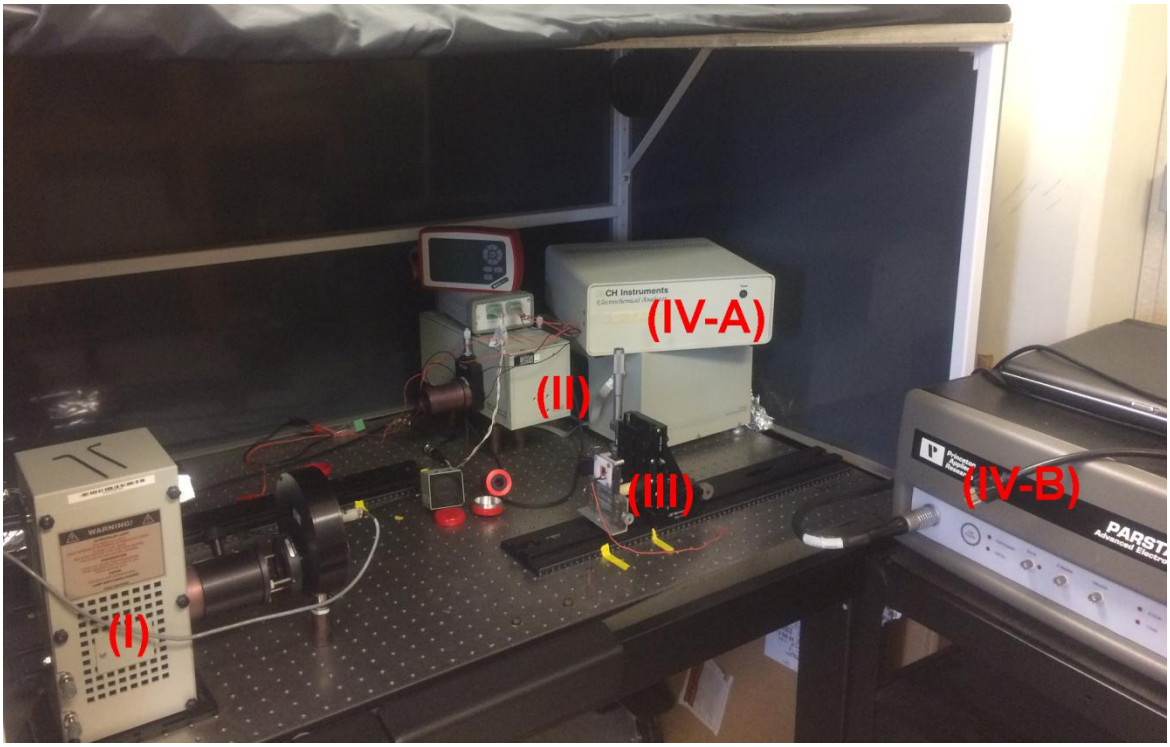

Figure 1.10 Layout of the Sun simulator.

The major components are: (I) 300 W Xenon arc lamp for full solar spectrum illumination, (II) 75 W Xenon arc lamp for monochromatic illumination, (III) movable solar cell stabilizer on an aligned orbit, and (IV-A and B) CHI 440A and PARSTAT 2273 potentiostat for electrochemical measurements.

1.4.2 I-V Measurement

Figure 1.11 is a typical current-voltage (I-V) curve obtained when a forward bias voltage (approx. -0.1 to 1 V depending on solar cells) is added between the photoanode and the counter electrode of the DSSC, allowing the photocurrent density to be measured under one-Sun illumination. The critical parameters of the solar cell indicating its photovoltaic performance, such as the short circuit current density (J_{SC}), open circuit voltage (V_{OC}), fill factor (FF), power conversion efficiency ($\eta\%$), shunt resistance (R_{SH}), and series resistance (R_S), can be extracted directly from this curve.

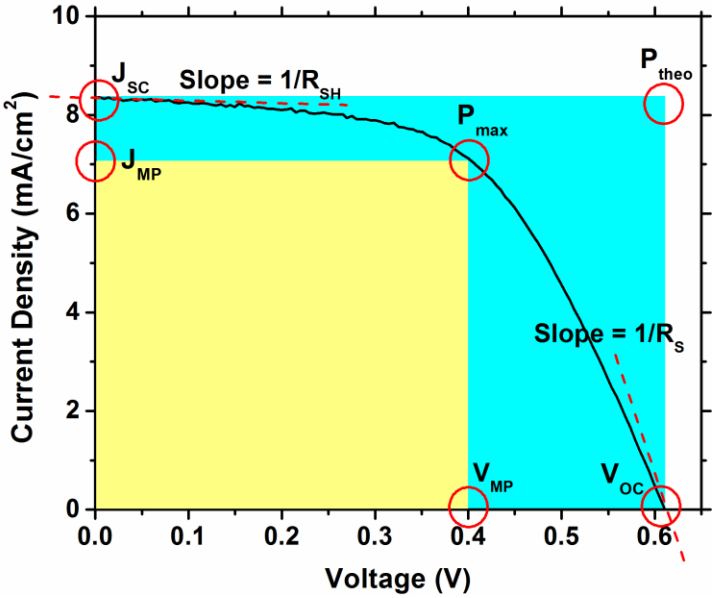

Figure 1.11 Typical I-V curve of the Ru-dye sensitized solar cell. The characteristic parameters are indicated on the graph.

The J_{SC} represents the maximum output current of the solar cell, attained when the bias voltage added on the cell is zero (i.e. the external load resistance is zero). The V_{OC} is the maximum output voltage, which occurs when the current flow through the device is zero (i.e. the infinite resistance is loaded). The power is described as the product of current and voltage. The area of the yellow rectangle in the I-V curve indicates the maximum output power (P_{max}) of the solar cell, corresponding to a certain point at which the product of the current density (J_{MP}) and the voltage (V_{MP}) achieves the P_{max}. The theoretical power (P_{theo}), represented as the cyan rectangle in this curve, equals to the product of J_{SC} and V_{OC}. The FF is defined as the ratio of P_{max} to P_{theo}, which is essentially the ratio of the area of the yellow rectangle to the area of the cyan rectangle, according to the following equation:

$$FF = P_{max} / P_{theo} = (J_{MP} \times V_{MP}) / (J_{SC} \times V_{OC}) \quad (1.1)$$

The value of FF varies from 0 to 1, related to the "squareness" shape of the I-V curve, which is affected by the R_{SH} and the R_S of the solar cell. The value of R_{SH} and R_S can be calculated

from the reciprocal of the slope of the I-V curve around the J_{SC} point and the V_{OC} point, respectively. Low R_{SH} will cause significant power losses by providing an alternate current path for photocurrent (i.e. current leakage) thereby decreasing the V_{OC}. R_S arises from the combined interfacial contact resistances, leading to a drop of the photocurrent. Thus an ideal solar cell should have an extremely large R_{SH} and a very small R_S.

The PCE ($\eta\%$) is the ratio of the P_{max} of the solar cell to the power of the incident radiation (P_{in}), which intuitively reflects the capability of the solar cell to convert the sunlight into electricity. It can be calculated using the following equation:

$$\eta\% = (P_{max}/P_{in}) \times 100\% = (FF \times J_{SC} \times V_{OC}/P_{in}) \times 100\% \quad (1.2)$$

As mentioned above, P_{in} has been calibrated to one-Sun power (100 mW/cm^2). Based on the equation, the PCE is also affected by the resistances of the device, related to the device fabrication and operation, involving the interface engineering of the applied photosensitizers with the charge collection materials associated with charge separation and transfer processes.

1.4.3 Incident-Photon-to-Current Efficiency (IPCE)

Incident-photon-to-current efficiency (IPCE) is performed under the monochromatic illumination, which describes the percentage of photons at each wavelength that are actually converted into electrons (current), and can be calculated from the equation:

$$IPCE_{\lambda} = (1240 \times J_{SC}) \times 100\% / (P_{in} \times \lambda) \quad (1.3)$$

Here, the P_{in} and J_{SC} are the incident power and short circuit current at each wavelength, which needs to be measured individually and input into the equation to obtain the IPCE of this wavelength. The IPCE curve of a conventional Ru-DSSC was plotted in Figure 1.12. The major peak of the curve at ~523 nm ideally corresponds to the maximum absorption of the N719 ruthenium dye (Red curve), while the minor peak at ~350 nm is due to the excitation of the semiconductive TiO_2 layer

convoluted with the glass substrate transmittance. Hence, the IPCE measurement is an effective method to distinguish the origin of the photocurrent generation.

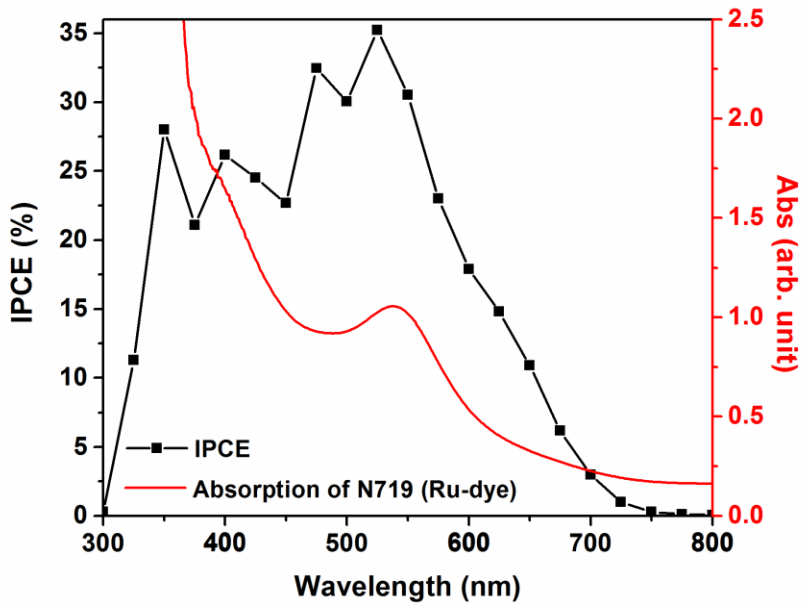

Figure 1.12 IPCE curve of Ru-dye sensitized solar cell (black curve).
The major peak of IPCE is correlated to the characteristic absorption of photosensitizer (N719 dye in red curve).

1.4.4 Synchronous Response of Short Circuit Photocurrent (Illumination On/Off)

Stability is another critical factor to evaluate the performance of solar cells, which can be investigated by synchronous response of the J_{SC}. The measurement is performed using chronoamperometry to record the J_{SC} versus time with illumination turned on and off for several cycles. The operation of the solar cell is stable, if the J_{SC} in each cycle is steady and reproduces well with other cycles (black curve in Figure 1.13). If a J_{SC} decay occurs under illumination (the red curve in Figure 1.13), the solar cell's dye regeneration is decaying due to the diffusion limit of electrolyte. Usually, a highly viscous electrolyte, such as an ionic liquid, is more likely to have diffusion limited issue in DSSCs, which also depends on the porosity of the semiconductive layer.

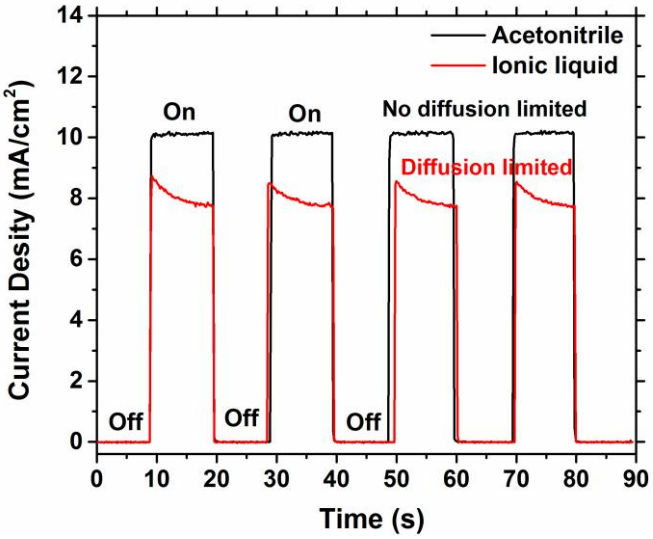

Figure 1.13 Synchronous response of short circuit photocurrent of Ru-dye sensitized solar cell.

The black curve is measured from the solar cell filled with traditional iodide electrolyte in acetonitrile (low viscosity), and red curve is measured from the solar cell using ionic liquid electrolyte (high viscosity). "On" and "Off" refer to one-Sun illuminated and dark conditions, respectively.

Chapter 2 - Preparations of Planar and 3D TiO_2 Films as Photoanode Materials

2.1 Introduction

Semiconductive TiO_2 is the most common photoanode materials in DSSCs. A 10 μm nanostructured TiO_2 film is usually prepared from deposition and sintering of spherical TiO_2 NPs on conducting glass, providing large surface area for dye adsorption and interparticle contacts for electron transport. A variety of TiO_2 structures, such as nanotubes, nanowires and networks, have been applied as alternatives of spherical NPs for more efficient electron transport pathway owing to their inherent well-aligned crystalline domains and the longer diffusion length of the electrons traveling in them.[74-75] In addition, anatase TiO_2 is better for DSSCs compared to the rutile forms due to higher dye loading as well as faster electron transport rate.[76] The TiO_2 crystallization can be affected by annealing process that yields the anatase phase if the annealing temperature is below 550 ℃; it tends to form the thermodynamically stable rutile phase at higher temperatures.[77] In this dissertation, three morphologies of anatase TiO_2, i.e. planar thin film, vertically aligned nanotree array and 3D network (NW) structure, were synthesized with different approaches and utilized in the three projects discussed in Chapter 3, 4 and 5, respectively, according to the specific requirements of the device design.

2.2 Materials and Reagents

The solvents for reactions were obtained from Fisher Scientific (Pittsburgh, PA) and were used as received. All the reagents and chemicals, unless otherwise specified, were purchased from Sigma-Aldrich (St. Louis, MO).

2.3 Planar TiO_2 Thin Film via $TiCl_4$ Treatment

FTO coated glass substrate (TEC8, Dyesol, Queanbeyan NSW, Australia) were covered with a thin TiO_2 layer by treatment with 40 mM aqueous solution of titanium tetrachloride ($TiCl_4$) at 75 ℃ for 20 minutes and sintered at 500 ℃ for 30 minutes, after rinsing with deionized water and ethanol. The obtained TiO_2 film was too thin to be seen on the rough FTO glass. In order to inspect the morphology and thickness of the deposited TiO_2 film, the same treatment procedure was applied on a flat polished silicon wafer. The SEM images in Figure 2.1 shows the 45° perspective view and the cross-sectional view of the deposited TiO_2 film, which is planar and covers the whole substrates but was not uniform; with the thickness varied from ~100 nm in the thinnest region to ~300 nm at nucleation sites.[78]

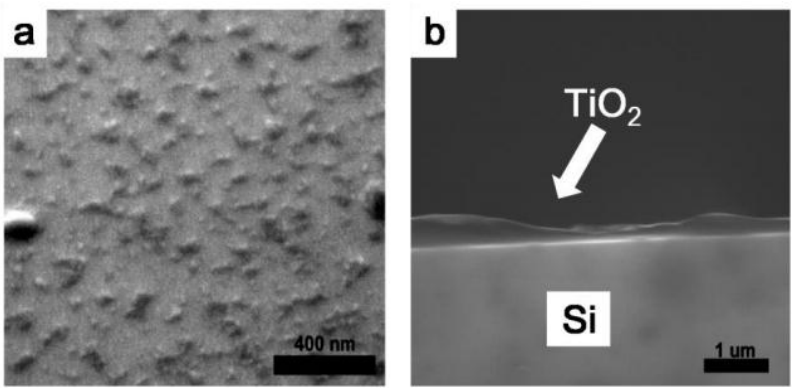

Figure 2.1 SEM images of the TiO_2 thin film deposited on the polished Si wafer via $TiCl_4$ treatment.

(a) the 45° perspective view, and (b) the cross-sectional view. (Image copied from ref. 78. Copyright © 2014 American Chemical Society)

The TiO_2 thin film commonly functions as a barrier layer between FTO substrate and mesoporous TiO_2 framework to suppress the recombination and electron backflow.[79] In Chapter 3, in order to diminish the photocurrent from TiO_2, the thick mesoporous TiO_2 layer was replaced with such thin TiO_2 film in the solar cell. The TiO_2 thin film covered FTO substrate (termed as

TiO_2-FTO) was further functionalized with 3-aminopropyltriethoxysilane (APTES) to enhance sensitization of photosynthetic protein complexes (See Section 3.2 for experimental details).

2.4 Hydrothermal Growth of TiO_2 Nanotree Array

FTO coated glass substrate were first deposited with a thin TiO_2 layer (150-300 nm) by treatment with 40 mM aqueous solution of $TiCl_4$ at 75 ℃ for 20 min, and sintered at 500 ℃ for 30 min after rinsing with deionized water and ethanol. The obtained TiO_2-FTO was placed against the wall of Teflon-lined stainless steel autoclave with the conducting side facing down. 0.73 g of potassium titanium oxide oxalate dihydrate ($K_2(TiO)(C_2O_4)_2 \cdot 2H_2O$) was dissolved in 10 mL water followed by quickly adding 30 mL diethylene glycol under vigorous stirring. The mixture was transferred to the autoclave. The hydrothermal reactions were then carried out at 200 ℃ for 9 h. After reaction, the autoclave was cooled to room temperature. The TiO_2 nanotrees grown on FTO were rinsed with water and ethanol several times, and then treated with 40 mM $TiCl_4$ at 75 ℃ for 30 min, followed by calcination at 500 ℃ for 30 min to achieve better crystallinity.

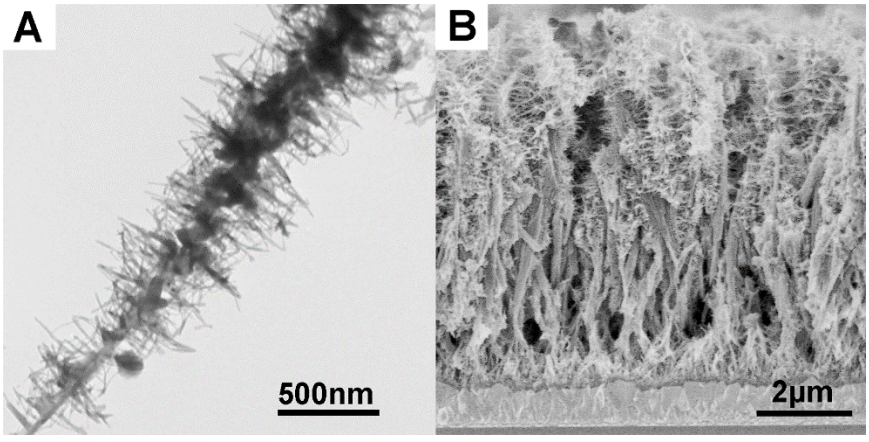

Figure 2.2 The morphology of the as-synthesized TiO_2 nanotrees observed by transmission and scanning electron microscopes (TEM and SEM).

(A) TEM image of the TiO_2 nanotree scraped off from the FTO substrate, (B) the cross-sectional view of TiO_2 nanotree array by SEM.

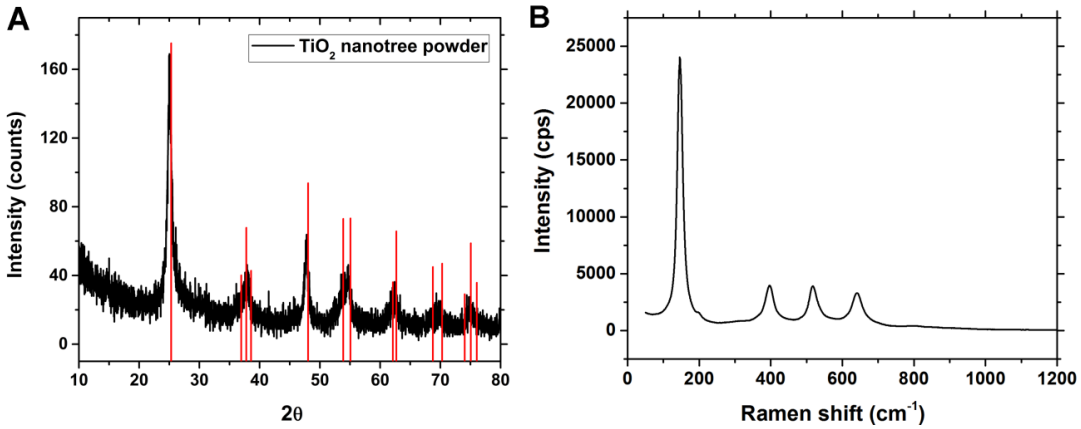

Figure 2.3 The crystalline structure of the TiO_2 nanotrees investigated by X-ray diffraction (XRD) and Raman spectroscopy.

(A) XRD pattern of the as-synthesized TiO_2 nanotrees, and the standard XRD peak position of anatase TiO_2 (JCPDS card No 71-1166) was indicated by the vertical red lines. (B) Raman spectrum of the TiO_2 nanotrees on a FTO coated glass substrate.

The TEM image (Figure 2.2A) and the cross-sectional SEM image (Figure 2.2B) illustrate the morphology of the synthesized TiO_2 nanotree array, showing a hierarchical growth composed of 6 μm-long TiO_2 trunk covered by short and thinner branches extending sideway. The XRD (Figure 2.3A) and Raman (Figure 2.3B) characterizations confirmed that the TiO_2 nanotrees after calcination are highly crystalline anatase phase which is ideal for fabricating DSSCs. In Chapter 4, the TiO_2 nanotree array applied as a photoanode material was then sensitized with nanoscale photosynthetic protein complexes in conjunction with plasmonic nanoparticles. The advantages resulting from this special morphology were discussed therein.

2.5 Core-Shell Au@TiO_2 Network

Gold nanoparticles (Au NPs) were prepared by citrate reduction of chloroauric acid ($HAuCl_4$) in aqueous phase.[19] 0.2 mL of $HAuCl_4$ solution (50 mg/mL) was added into 100 mL of boiling water rapidly, followed by adding 3 mL of trisodium citrate solution (1 wt%). The mixture was kept boiling with stirring for 30 min to form Au seed. Then the temperature of the bath was decreased to 90 ℃. 3 mL of 1 wt% trisodium citrate and 0.2 mL of 50 mg/mL $HAuCl_4$ solution

were simultaineously added to the mixture again. This procedure was repeated 3 times to attain ca. 20 nm Au NPs.

To synthesize Au@TiO_2 network, core-shell Au@TiO_2 NPs were first prepared following a published method[45]. Briefly, 10 mL of 0.02 mol/L L-Arginine aqueous solution (Aldrich) was added to the as-prepared ~25 nm Au NPs (1.4×10^{14} particles/L) to replace the surface citrate ligands. 12 mL of cyclohexane was then added into the mixture to form a biphasic system. A glass-like amorphous silane monolayer was then formed by adding 12 mL of (3-mercaptopropyl)triethoxysilane (MPTS, 98%, TCI) into the cyclohexane layer and stirring gently for 6 hours. Further TiO_2 growth on the Au NPs surface requires a dehydrated condition. Thus the MPTS capped gold cores were collected and redispersed into 20 mL dehydrated ethanol (absolute ethanol, 99.8%, Fisher) followed by centrifugation and washing with another 20 mL dehydrated ethanol. This procedure was repeated three times.

To form a uniform thin TiO_2 shell, this ethanolic solution of silanized Au NPs was added with 1 μL of titanium tetra-isoproxide (TTIP, 97%, Aldrich) as the precursor and mildly stirred under 25 ℃ and 50% humidity for 1.5 hrs. The network structure was obtained by adding more TTIP (6.4 μL in total) for 12 hrs reaction. Hydrolysis of excess TTIP thus crosslinked the core-shell Au@TiO_2 NPs to form a network. The sample was purified by rinsing three times with dehydrated ethannol and centrifugation to remove the residual TTIP. The weight percentage of Au NPs in the as-prepared Au@TiO_2 network is about 7%. Bare TiO_2 network was prepared as a control by similar TTIP hydrolysis but without adding silanized gold cores.

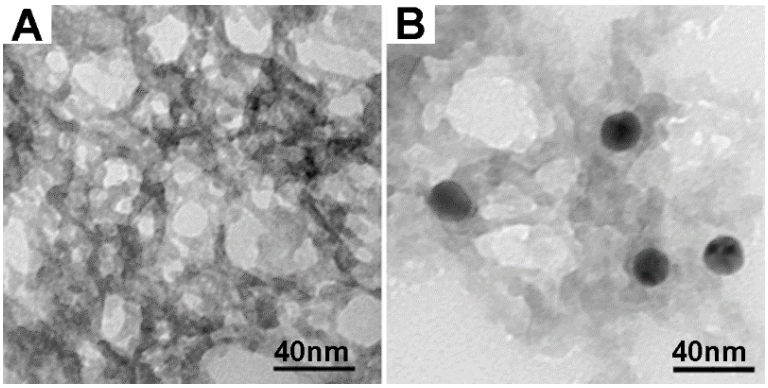

Figure 2.4 TEM images of (A) the TiO_2 network, and (B) the core-shell Au@TiO_2 network.

The network structure was confirmed by the TEM images shown in Figure 2.4. Compared to spherical TiO_2 NPs, the network structure was expected to conduct charge better due to the interconnection of the framework consist of TiO_2 nanowires. With the incorporation of Au NPs, the plasmonic effect on the photoconductivity and the photovoltaics were investigated in Chapter 4 through the devices (i.e. microgap electrode and DSSC) employing the Au@TiO_2 network.

Chapter 3 - Photovoltaic Properties of LHCII Aggregates on Sensitized Planar TiO_2 Solar Cells[†]

3.1 Introduction

Light harvesting complex II (LHCII) is the most abundant chlorophyll-protein complex in nature and the major antenna complex in PSII. The largest PSII supercomplex, $C_2S_2M_2$, consists of a dimeric core complex (C_2) containing RCs, 4 monomeric minor antenna complexes, 4 strongly attached LHCII trimers (S_2 and M_2), and 3 to 4 loosely attached LHCII trimers.[80] Figure 1A shows the top and side views of the crystal structure[81] of an isolated LHCII trimer and its physical dimensions. The LHCII trimer consists of three monomers each of which comprises a polypeptide of about 232 amino-acid residues, 8 Chl *a* and 6 Chl *b* molecules, 3-4 carotenoids and one phospholipid.[81] LHCII not only has a primary role in light harvesting and transferring the excitation energy to the RC, but is also critical in photosynthesis regulation through photoprotective mechanisms called non-photochemical quenching (NPQ).[80, 82-87] LHCII protein aggregation was proposed to be one of the mechanistic factors controlling the dissipation of excess photo-excited state energy of chlorophylls during NPQ (see e.g. reference[88] as a review and references therein).

Photovoltaic behavior of LHCII has been confirmed by the photocurrent enhancement observed in LHCII incorporated DSSCs, which demonstrated the feasibility of LHCII as a photosensitizer.[45, 56] However, little is known about the effects of LHCII aggregation on the photovoltaic and sensitization characteristics. In contrast to isolated LHCII trimers, the Chl excited

[†] Reproduced in part by permission of Royal Society of Chemistry, Y.Yang, R. Jankowiak, C. Lin, K. Pawlak, M. Reus, A. R. Holzwarth, J. Li, Effect of the LHCII Pigment-Protein Complex Aggregation on Photovoltaic Properties of Sensitized TiO2 Solar Cells, *Phys Chem Chem Phys*, 2014, 16, 20856-20865. DOI: 10.1039/c4cp03112a.

states in the aggregates are strongly quenched by the formation of chlorophyll-chlorophyll charge transfer (CT) states whose presence in aggregated LHCII was independently studied recently via high-resolution hole-burning (HB) spectroscopy.[89] If the Chl-Chl CT states in the LHCII can be coupled with the TiO_2 surface, it would enhance electron injection into the TiO_2 conduction band. In this study, we compare the effects of different sizes of LHCII aggregates to illustrate the contribution of aggregation induced CT states to the photovoltaic performance using a model nanoscale thin-film TiO_2 DSSC (schematically shown in Figure 3.1B), and aim to reveal if there is any correlation between the surface coverage/sizes of aggregates and the photovoltaic performance.

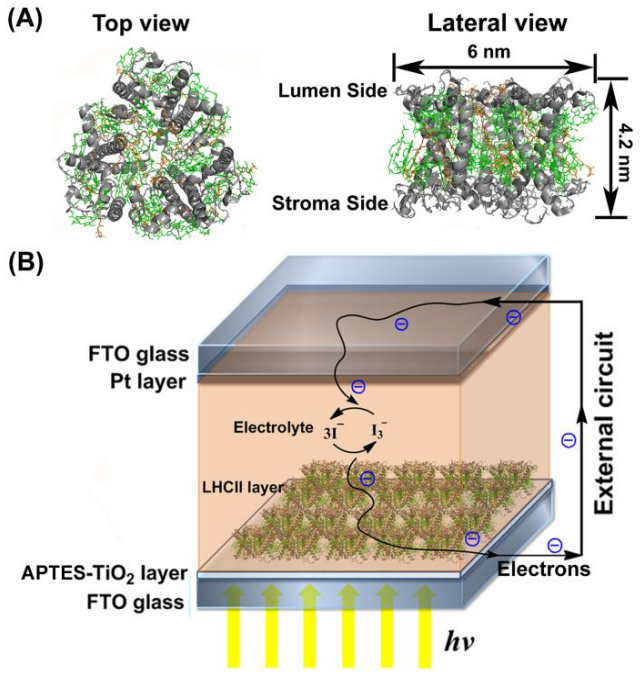

Figure 3.1 Structure of LHCII trimer and the scheme of LHCII sensitized solar cell.

(A) Top and side view of the LHCII trimer consisting of Chl *a* and *b* (green); carotenoids (orange); and polypeptides (grey helices). (B) Schematic model of a LHCII sensitized solar cell assembled by attaching LHCII aggregates to a thin APTES-TiO_2 compact layer on a FTO-coated glass. (Reprinted with permission from Y. Yang, R. Jankowiak, C. Lin, K. Pawlak, M. Reus, A. R. Holzwarthb and J. Li, *Phys. Chem. Chem. Phys.*, 2014, 16, 20856-20865.)

3.2 Experimental Section

3.2.1 Preparation of LHCII Aggregates

The LHCII trimers were extracted from spinach thylakoids as described in the literature[90] and were dispersed in 5 mM tricine buffer (pH = 7.5) with detergent (0.1 M sucrose and 0.06% n-dodecyl β-D-maltoside [β-DM]). Large aggregated LHCII complexes (called "large aggregates" throughout this paper) were formed upon removal of the detergent by several treatments with Biobeads SM-2 (Bio-Rad). For a comparison, smaller less quenched and more homogenous LHCII aggregates (called "small aggregates") were prepared by partial disaggregation of large aggregates in the buffer with low concentration of detergent (0.008% β-DM) after sonication.

The LHCII concentration shown in units of equivalent Chls, was measured according to the procedure described in reference.[91] Chls (Chl *a* and Chl *b*) in LHCII complexes were extracted with buffered aqueous acetone (80% aqueous acetone containing 2.5 mM phosphate buffer with pH = 7.8) and centrifuged with 7800 rpm to remove the insoluble protein residue. All the operations were handled quickly under dim light and 4 ℃ to avoid breakdown of the Chls. By measuring the UV-Vis absorption of the supernatant, the Chl content was calculated using the absorbance at 646.6 nm and 663.6 nm based on the equation shown in Table III of the reference[91] i.e. $\text{Chls}(a+b) = 17.6A^{646.6} + 7.34A^{663.6}$. Thus, the derived Chl contents of the small and large aggregate solutions were 16.2 μg Chl/mL and 17.1 μg Chl/mL, respectively.

3.2.2 Absorption and Emission Spectroscopic Measurements.

Absorption spectra were recorded using a Beckman DU640 spectrophotometer at room temperature. Room-temperature fluorescence emission spectra of LHCII solutions were first measured with a 1-m McPherson monochromator (model 2601, slit width 100 μm) with 150/mm grating and a Princeton Instruments back-illuminated N_2-cooled CCD camera. The excitation

source for the fluorescence experiments was a Coherent UV argon-ion laser operating at 496.5 nm. Further fluorescence emission spectra were collected by a home-build set up from LHCIIs deposited on TiO_2/FTO photoanodes and LHCII solutions (for direct comparison). The excitation source was synchronously pumped dye laser (Spectra-Physics) equipped with cavity-dumper (Spectra-Physics) with the repetition rate of 4 MHz. The DCM (4-Dicyanomethylene-2-methyl-6-4-dimethylaminostyryl-4H-pyran) was used as a dye to provide the excitation wavelength at 663 nm. A micro-channel-plate photomultiplier (Hamamatsu) and a Jobin Yvon monochromator with 2 nm slit were used as the detection system.

3.2.3 Treatment of Photoanodes

The TiO_2-FTO (as-prepared in Chapter 2.3) and clean FTO substrates (for control experiments) were soaked in 10 wt% APTES in redistilled toluene, refluxed for 4 hours, followed by baking at 120 ℃ overnight. The APTES modified substrates (i.e. APTES-TiO_2-FTO and APTES-FTO) were used as the photoanodes for LHCII-sensitized solar cells.

3.2.4 Fluorescence Microscopic Characterization of LHCII Attachment

APTES-FTO substrate masked with a TEM grid (1GC200, PELCO, Hole Width 90 μm; Bar Width 37 μm) was exposed to UV light (8 W UV lamp, 254 nm, Cole-Parmer) to create amino patterns. The amine groups under the exposed area were converted to –OH groups. After incubation in small-sized LHCII aggregate solution in dark at 4 ℃ for 12 hours followed by rinsing, fluorescence images were recorded with an Azioskop 2 FS Plus Microscope (Carl Zeiss) with a filter set of 480±20 nm excitation band and 515-565 nm emission band to examine the selective attachment of LHCII to amine-terminated surface.

3.2.5 Atomic Force Microscopy (AFM) Measurements

Clean Si wafers were soaked in the mixture of water, 30% ammonium hydroxide, 30% hydrogen peroxide (5:1:1 v/v ratio) at 75 °C for 15 min to make the wafers more hydrophilic, and then stored in an ultrapure water, dried by nitrogen blowing right before use. The pretreated Si wafer was dipped into LHCII solutions to immobilize some LHCII complexes and then rinsed with ultrapure water to remove the surfactant and other buffer residues. AFM was carried out in tapping mode on a BioScope (Digital Instruments, Santa Barbara, CA) with a scan speed at 1.5 Hz using silicon cantilevers with a resonance frequency between 65 and 80 kHz.

3.2.6 Assembly of LHCII or Chlorophyll Sensitized Solar Cells

For LHCII-sensitized solar cells, an APTES-TiO_2-FTO or APTES-FTO substrate was used as a photoanode and the Pt-coated FTO/glass as the counter electrode. A 1 × 1 cm window was cut precisely into a 60 μm thick hot melt spacer (Solaronix, SX 1170-60PF) and was sealed at 110 °C for 5 min. The LHCII solutions were filled in the cell, which was stored in dark at 4 °C for 12 hours and then washed by successively injections of tricine buffer, water and ethanol. The electrolyte (Iodolyte AN-50, Solaronix) containing 50 mM iodide/tri-iodide in acetonitrile was finally injected into the cell to complete the solar cell fabrication. To avoid LHCII degradation, the Iodolyte electrolyte was replaced with related tricine buffer after each photovoltaic measurement, and the solar cells were stored at 4 °C. A similar solar cell using physisorbed Chls from spinach (≥ 90.0%, Sigma-Aldrich) (at 8:6 Chl *a* to Chl *b* molar ratio similar to LHCII) as alternative sensitizers was fabricated and used as a control. About 120 μg Chl/mL in dry diethyl ether was used as the loading solution to sensitize TiO_2-covered FTO anode.

3.2.7 Solar Cell Tests

A photovoltaic I-V curve of the solar cells was measured under the irradiation of 1 Sun power (100 mW/cm^2) using a 300 W Xeon lamp with an AM1.5G filter. Three different bandpass interference filters (Edmund Optics, 50 nm FWHM, OD >4.0, Stock NO. 84782, 86952, and 86954) were added to select light only in the wavelength range of 450±25 nm, 575±25 nm, and 675 ± 25 nm, respectively, and photocurrent response curves were collected with chronoamperometry measurements using a potentiostat (CHI 440A Electrochemical Analyzer) while the shutter was turned on and off.

3.3 Results and Discussion

3.3.1 Formation of Charge Transfer States in LHCII Aggregates

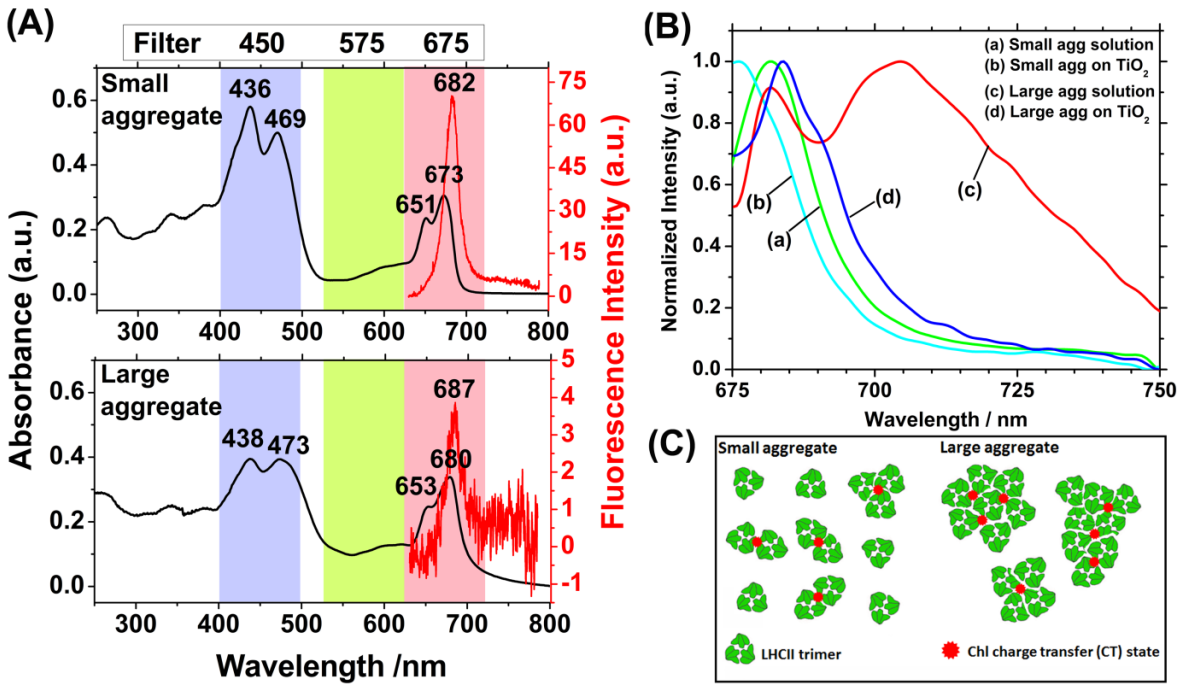

Figure 3.2 Absorption and emission properties of LHCII aggregates associated with the formation of CT states.

(A) Absorption and fluorescence emission spectra (λ_{ex} = 496.5 nm) of small- and large-size LHCII aggregates in tricine buffer with the concentration (in unit of total Chl content) of 16.2 μg Chl/mL and 17.1 μg Chl/mL, respectively. The colored shades indicate the bandwidth of the three bandpass interference filters used in photovoltaic measurements. (B) Normalized

steady-state fluorescence emission spectra (λ_{ex} = 663 nm) of small- and large-size LHCII aggregates in solutions and deposited on the APTES-TiO_2-FTO photoanode surface. Note that the fluorescence of large aggregates on the TiO_2 surface is extremely weak. Each spectrum was normalized to its highest peak intensity for better view of the detailed spectroscopic features. (C) Schematic illustration of the CT states formed in small and large aggregates. (Reprinted with permission from Y. Yang, R. Jankowiak, C. Lin, K. Pawlak, M. Reus, A. R. Holzwarthb and J. Li, *Phys. Chem. Chem. Phys.*, 2014, 16, 20856-20865.)

The absorption and fluorescence emission spectra of the small- and large-size LHCII aggregates are shown in the top and bottom frames of Figure 3.2A, respectively. Free Chl pigments in diethyl ether were reported to show strong absorption peaks in the Soret region (at 430 nm for Chl *a* and 452 nm for Chl *b*) and in the Q_y region (at 661 nm for Chl *a* and 645 nm for Chl *b*).[45] For the small-size LHCII aggregates in this study, these absorption peaks were red-shifted to 436/469 nm and 673/651 nm, respectively, similar to those observed in isolated LHCII trimers.[45] However, the room-temperature (0,0)-band emission was red-shifted by about 2-3 nm to 682-683 nm in contrast to isolated LHCII trimers with a maximum near 680 nm. The absorption of large-size aggregates shows larger red-shifts to 438/473 nm and 679/653 nm and a characteristic red tailing, suggesting the formation of CT states. The fluorescence of large LHCII aggregates is significantly quenched, dropping the intensity by 10 times comparing to small aggregates.

The raw spectra showed largely varied fluorescence intensity among LHCII samples with different degree of aggregation. For better view and comparison of their spectroscopic features, each spectrum was normalized to its highest peak intensity. Fig. 3.2B compares the normalized fluorescence emission spectra of LHCII in various aggregation states in solutions and after being deposited on the TiO_2/FTO photoanode as sensitizers. The fluorescence origin band shifts to about 687 nm in the large aggregates in solution (as compared to LHCII trimers which are not quenched) and a very strong far-red emission band (from 690 to 750 nm) appears. The far-red emission has been shown to derive from Chl-Chl CT states[87, 92], in agreement with the recent findings by

Magdaong et al.[93] Formation of the CT states (characterized by a strong electron-phonon (el-ph) coupling) was revealed recently via resonant HB spectroscopy.[89] In this case, resonant holes were burned in the low-energy absorption wing of aggregated LHCII complexes.[89] Thus the extent of the red-shift observed in room temperature fluorescence spectra and in particular the relative intensity of the far-red (from 690 to 750 nm) emission peak to the shorter-wavelength emission peak of aggregated LHCII complexes reflects the size of the aggregates and the quenching efficiency. This suggests that the large-size LHCII aggregates form CT states at much higher yield than the small-size aggregates.

Most interestingly, the CT state (far-red band) emission completely disappears when the aggregates are deposited as sensitizers on the surface of APTES-TiO_2-FTO substrates (to be used as photoanodes in solar cells) (Fig. 2B). Only very weak fluorescence remains. For small LHCII aggregates, the differences between the fluorescence emission spectra on APTES-TiO_2-FTO surface (curve b) and in solution (curve a) are much smaller. The shape of the fluorescence spectrum of small LHCII aggregates on TiO_2 is more similar to that of LHCII trimers in solution (but with largely different intensity, data not shown), while the fluorescence spectrum of large aggregates on APTES-TiO_2-FTO surface is more red-shifted and differs pronouncedly (on top of the large difference in intensity).

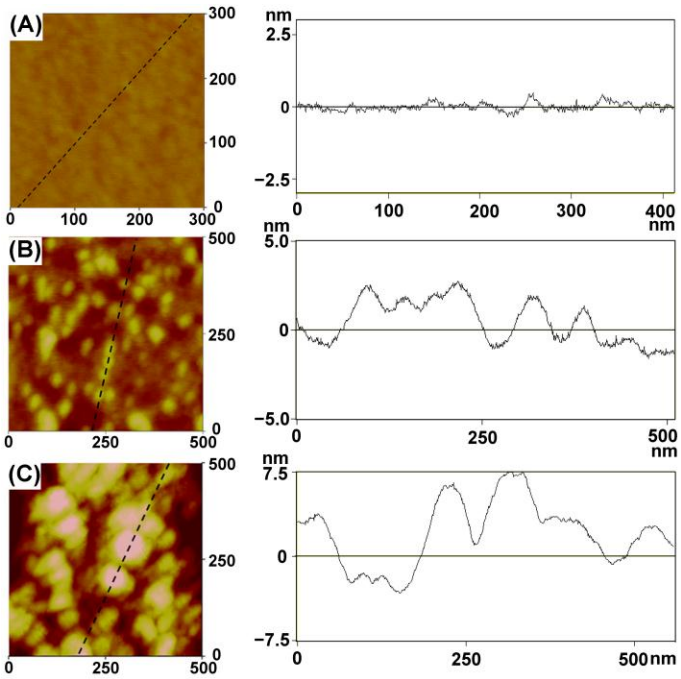

Figure 3.3 The display of LHCII aggregates on solid state substrate.

AFM images and line profiles of (A) a clean silicon wafer and a silicon wafer deposited with (B) the small-size LHCII aggregates and (C) the large-size LHCII aggregates. Measurements were carried out in tapping mode under a nitrogen atmosphere. (Reprinted with permission from Y. Yang, R. Jankowiak, C. Lin, K. Pawlak, M. Reus, A. R. Holzwarthb and J. Li, *Phys. Chem. Chem. Phys.*, 2014, 16, 20856-20865.)

The size of aggregates in the above two samples was further confirmed by measuring the morphology of LHCIIs deposited on a flat surface with AFM, as shown in Figure 3.3. Compared to the smooth surface of bare silicon wafer (Figure 3.3A), brighter dots are clearly observed on the silicon wafer treated with the solution of small-size aggregates (Figure 3.3B). Two kinds of dots can be observed. The smaller (ca. 6 ~ 10 nm) and relative blurred ones are considered as intact LHCII trimers, while the larger (ca. 22 ~ 50 nm) and brighter ones would be small aggregates consisting of two or three trimers. Since the average height from the line profile in Figure 3.3B is only ~ 4 nm, LHCII in this sample likely only formed two dimensional aggregates. In contrast, the AFM images of the large-size LHCII aggregates (formed by intentionally removing the detergent) revealed much larger islands with a diameter of 50 to 100 nm, as illustrated in Figure 3.3C. The

line profile in Figure 3.3C shows a large height of ~10 nm, indicating the likely formation of three dimensional aggregates. These AFM images are consistent with the spectroscopic characteristics revealing the structural difference between the small- and large-size aggregates.

3.3.2 Adsorption of LHCII Aggregates on APTES-TiO_2 Surface

The physisorption of LHCII on the TiO_2 surface was found to be very weak and unstable, as indicated by the long incubation time (96 hours) required to reach saturated adsorption in literature.[45] We also found that only small amount of LHCII was anchored to the thin TiO_2 layer via physisorption, which significantly limited the photocurrent enhancement by LHCII sensitizers (see Appendix Figure A.1). It was recently reported that strong LHCII attachment can be obtained on a APTES functionalized FTO substrate via electrostatic interaction between the anionic residues on the stromal side with cationic $-NH_3^+$ groups.[56] This approach was adopted in this study. Figure 3.4A shows the fluorescence microscopic image of the small-size LHCII aggregates adsorbed on a patterned APTES-FTO substrate. The pattern correlates well with the shape of the optical mask (Figure 3.4B). The APTES-FTO surface was subjected to an UV exposure except in the cross-shaped area where the solid grid frame (ca. 37 μm in width) blocked the UV light. UV radiation is known to effectively cleave the amine group of APTES and to convert the surface back to normal –OH groups.[56] The fluorescence contrast between the exposed and blocked areas clearly confirmed that the electrostatic interaction facilitated by the APTES-functionalized surface provides much stronger LHCII adsorption. Hence, in this work, all the photoanode substrates for DSSCs were treated with APTES before LHCII attachment. The strong surface adsorption is particularly important in controlling sub-monolayer LHCII coverage on the APTES-TiO_2 surface. However, though selective attachment of LHCII complexes was believed to occur between the anionic LHCII polypeptide at the stromal side and the cationic APTES surface,[56] it is likely that

both stromal and luminal surfaces may work since they both contain negative charges in the LHCII proteins.

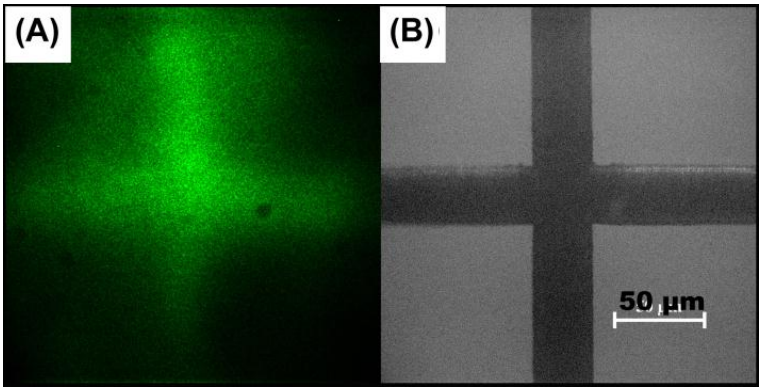

Figure 3.4 Attachment of LHCII aggregates on a patterned APTES-FTO substrate.

(A) A fluorescence image of small-size LHCII aggregates attached on a patterned APTES-FTO substrate. (B) An optical microscopy image of the corresponding mask in which the UV light was blocked by the solid grid frame (the dark area) and can only pass through the open squares (light areas). The scale bar is 50 μm. (Reprinted with permission from Y. Yang, R. Jankowiak, C. Lin, K. Pawlak, M. Reus, A. R. Holzwarthb and J. Li, *Phys. Chem. Chem. Phys.*, 2014, 16, 20856-20865.)

In fabricating LHCII sensitized solar cells, a 1× 1 cm^2 window was cut in a 60 μm thick hot melt spacer sandwiched between the sensitized photoanode and a Pt/FTO/glass cathode. The total volume in the solar cell sealed with this spacer is ca. 6.0 μL. An isolated LHCII trimer has a cross-sectional area of 2618 to 3333 $Å^2$, corresponding to a radius of ~3 nm.[94] Assuming that all LHCIIs in solution are adsorbed onto the photoanode surface, it requires filling a LHCII solution with a concentration of 33.6 μg Chl/mL (in unit of equivalent Chl content) to form a hexagonal close-packed monolayer on 1 cm^2 TiO_2 surface, defined as $C_{monolayer}$. In order to study the effect of the aggregation-dependent CT states on the photovoltaic properties, more diluted samples were used to control the LHCII adsorption less than a fully covered monolayer. The actual concentration of LHCII solutions (C_{LHCII}) used in the experiments were calculated from the optical absorbance of extracted chlorophylls (as described in the experimental section), giving 16.2 μg Chl/mL for

small-size aggregates and 17.1 μg Chl/mL for large-size aggregates, both lower than that required concentration for forming a close-packed monolayer, i.e. $C_{monolayer}$ = 33.6 μg Chl/mL. Thus, it only forms a sub-monolayer if we fill the LHCII solution into the solar cell only one time. As schematically illustrated in Figure 3.2C, at such sub-monolayer stage, the adsorbed small- and large-size aggregates are isolated and not in contact with neighboring aggregates. The ET between the neighboring trimers/aggregates should be minimal.

To precisely determine the efficiency of LHCII adsorption onto the APTES-TiO_2 photoanode, we compared the extracted Chl concentration of the LHCII solution before and after incubation in solar cells (see Appendix A Figure A.2). The attachment efficiency (η_{attach}) was determined to be about 95%, which confirmed the strong electrostatic interaction between LHCII and APTES. As will be demonstrated later, such strong interaction also facilitates the high stability of the LHCII-sensitized solar cells. Thus the effective surface coverage (ESC, see Table 1) of LHCII on the photoanode of each solar cell can be estimated based on the following equation:

$$ESC = \frac{C_{LHCII}}{C_{monolayer}} \times \eta_{attach}\% \quad (3.1)$$

A full monolayer coverage (i.e., 100% of ESC) was attained by repeating 5 times the procedure including filling a fresh LHCII aggregate solution to the solar cell cavity, incubating for 4 hours for LHCII adsorption, and then rinsing off weakly bonded LHCII top layers with blank tricine buffer.

3.3.3 Charge Transfer and Operation of LHCII Sensitized Solar Cells

The emission spectra and AFM images discussed above clearly show that the two LHCII samples formed different extent of aggregates. We have shown recently that, in the case of large-size aggregates (prepared in absence of detergent), more Chl-Chl CT states can be formed between the surface Chls as revealed by the very strong el-ph coupling.[89] The most relevant pigments

involved in the formation of CT states are likely Chls 610, 611, and 612 (using nomenclature of Z. Liu et al.[81]) because they are close to the surface, have the lowest site-energies, and strongly contribute to the lowest energy exciton band.[95] Thus electrons transfer from the CT states to the TiO_2 layer facilitates generation of the observed photocurrent by aggregated LHCII.

If our interpretation is correct, we expect that the deposition of highly quenched large LHCII aggregates as a sensitizer and the functioning of this sensitizer as electron donor from the Chl-Chl CT states into the TiO_2 conduction band would concomitantly quench the far-red emission (from 690 to 750 nm) in the aggregates resulting from the Chl-Chl CT states. This is indeed the case as is seen in Figure 3.2B. The far-red CT emission band is absent from the LHCII aggregates when deposited on TiO_2 and only a broad long-wave tail remains in the large aggregates.

Figure 3.1B schematically depicts the structure of the LHCII sensitized solar cell. One notable difference from the previous reported LHCII solar cells[45, 56] is that a very thin (150-300 nm) compact TiO_2 layer is used here to replace the 10 to 12 μm thick mesoporous TiO_2 film formed by sintering ~20 nm diameter TiO_2 nanoparticles. This is necessary for two reasons. First, it minimizes the photocurrent generated by UV photons absorbed by the TiO_2 framework. As shown in Appendix Figure A.3, a solar cell fabricated with a bare 10-μm mesoporous TiO_2 can generate by itself a strong photovoltaic effect with a J_{SC} from ~0.14 to ~0.6 mA/cm^2 under 1 sun illumination. This makes it difficult to extract the photocurrent generated explicitly by LHCII sensitizers. Second, the internal pores of the typical mesoporous TiO_2 films are tortuous and poorly defined, with the size of only ~8 nm or less. As a result, it was reported that even the isolated LHCII trimers, which have a comparable size to the pore, only formed a layer at the outer surface of the mesoporous TiO_2 film.[45] Both of these factors may obscure the details of LHCII

contribution, particularly at the sub-monolayer coverage and in the I-V curve under the irradiation of the full solar spectrum.

On the other hand, a thin compact TiO_2 layer is required as a barrier to prevent electron backflow from the FTO anode to the electrolyte. Figure A.3B of Appendix A shows that the DSSC with LHCII directly attached to the APTES-FTO anode only gives very low values for both J_{SC} and V_{OC}. In a previous report[78], we have demonstrated that a TiO_2 film of 150 to 300 nm thickness formed by treatment of the FTO electrode with 40 mM $TiCl_4$ solution for 20 minutes serves well as an effective barrier layer. This method was adopted in this study. In addition, to avoid protein denaturation by the volatile organic solvent (such as acetonitrile) that was used in typical Grätzel cells, we previously used an ionic liquid electrolyte. However, we found that, though clear photovoltaic effects were observed, the performance of the ionic liquid electrolyte is far inferior to the volatile electrolyte (see Figure A.4 in Appendix A). Hence the typical Iodolyte in acetonitrile, which was recently reported to be compatible with LHCII complexes[45], was used in this study.

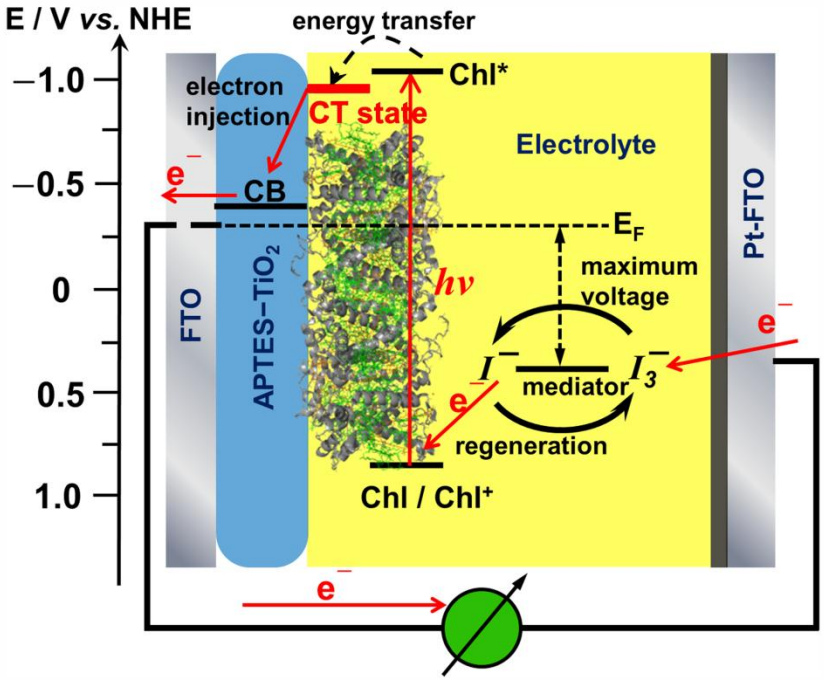

Figure 3.5 Electron transfer and energy level scheme of a photovoltaic device based on aggregated LHCII complexes.

(Reprinted with permission from Y. Yang, R. Jankowiak, C. Lin, K. Pawlak, M. Reus, A. R. Holzwarthb and J. Li, *Phys. Chem. Chem. Phys.*, 2014, 16, 20856-20865.)

Figure 3.5 shows the electron transfer and energy level scheme of the prepared solar cell based on aggregated LHCII complexes as the sensitizer. Potentials are relative to the normal hydrogen electrode (NHE). The V_{OC} (maximum voltage) corresponds to the difference between the redox potential of the Iodolyte mediator and the Fermi level of the FTO film. To be noted, the CT states in aggregated LHCII mixed with the excited state of chlorophylls have lower oxidation potential due to their more reddish absorption and red tail in UV spectra (see Fig. 3.2 and the related description). The CT states couple with the TiO_2 conduction band more effectively and lead to a more efficient electron injection accompanied with fluorescence emission quench (as shown in Fig. 3.2B).

3.3.4 Photovoltaic Characterizations and Stability of LHCII Sensitized Solar Cells

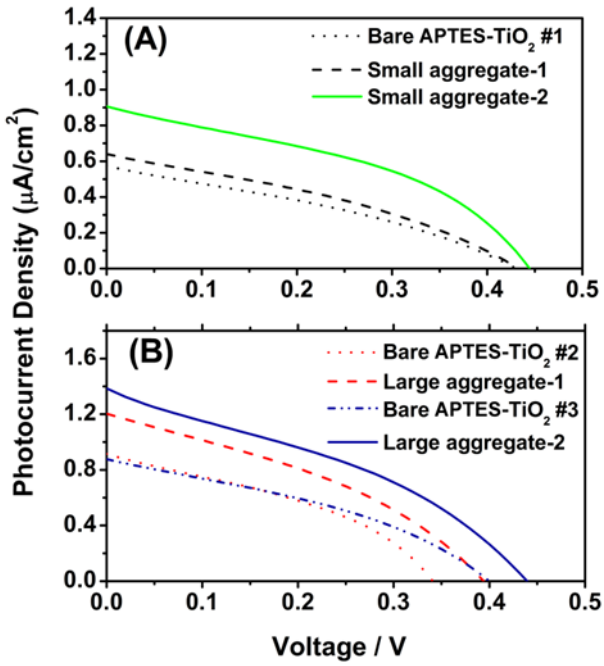

Figure 3.6 I-V curves of LHCII sensitized TiO_2 solar cells.

(A) Solar cells made of a bare APTES-TiO_2 photoanode (bare APTES-TiO_2 #1, dot) and after being first sensitized with 45.8%-coverage small-size LHCII aggregates (small aggregate-1, dashed line) and then further sensitized with 100%-coverage small-size LHCII aggregates (small aggregate-2, solid). (B) Solar cells made of the 2nd bare APTES-TiO_2 photoanode (bare APTES-TiO_2 #2, dot) and this electrode after being sensitized with 48.3%-coverage large-size LHCII aggregates (large-size aggregate-1, dash), the 3rd bare APTES-TiO_2 photoanode (bare APTES-TiO_2 #3, dash-dot-dot) and this electrode after being sensitized with high-coverage large-size LHCII aggregates (large-size aggregate-2, solid). All measurements were under 1 sun illumination with an AM1.5G filter. (Reprinted with permission from Y. Yang, R. Jankowiak, C. Lin, K. Pawlak, M. Reus, A. R. Holzwarthb and J. Li, Phys. Chem. Chem. Phys., 2014, 16, 20856-20865.)

Figure 3.6 shows I-V curves of the TiO_2 solar cells sensitized with the two LHCII samples with different degrees of aggregation and at two different ESCs, one submonolayer and one full monolayer. These data confirmed that the photovoltaic effects were enhanced after the APTES-TiO_2 surface was sensitized with both small- and large-size LHCII aggregates. Both J_{SC} and V_{OC} consistently increased as the ESC of LHCII aggregates was raised. Modifying the surface of the TiO_2 thin film with APTES suppressed the photocurrent generated by UV photon absorption in TiO_2, with J_{SC} dropping from ~8 $\mu A/cm^2$ (see Figure S1) to ~0.6 to 0.9 $\mu A/cm^2$, possibly due to electron trapping and recombination at the positively charged $-NH_3^+$ group at the TiO_2 surface. However, as it is shown later, the $-NH_3^+$ group did not block the CT from LHCII to the photoanode since illumination the solar cell with the selected light band that can only be absorbed by LHCII was able to produce substantial photocurrent. APTES modification was necessary to enable the strong adsorption of LHCII on the TiO_2 surface and thus made it possible to observe the differences between two LHCII aggregates. The values of V_{OC} are comparable in all these solar cells, at about 0.40 to 0.45 V.

Table 3.1 The characteristic values of the TiO_2 solar cells sensitized with LHCII aggregates at different ESCs (in percentage).

	ESC%*	J_{SC} (μA/cm2)	V_{OC} (V)	ΔJ_{SC}%
Bare APTES-TiO_2 #1	0	0.575	0.427	N.A.
Small aggregate-1	45.8	0.640	0.432	11.3
Small aggregate-2	100	0.907	0.444	57.7
Bare APTES-TiO_2 #2	0	0.915	0.340	N.A.
Large Aggregate-1	48.3	1.203	0.394	31.5
Bare APTES-TiO_2 #3	0	0.876	0.398	N.A.
Large Aggregate-2	100	1.386	0.424	58.2

Table 3.1 summarizes the characteristic values of the I-V measurements shown in Figure 3.6. The percentage increase in J_{SC} (i.e., ΔJ_{SC}%) from the bare APTES-TiO_2 cell was used to compare the results so that the difference caused by the variation in thickness and roughness of the TiO_2 barrier layer can be normalized. By filling LHCII solution into the cell only once, the LHCII adsorption was defined by Eq. (1), giving an ESC of 45.8% for small-size aggregates (in the cell labeled as "small aggregate-1") and 48.3% for large-size aggregates (in the cell labeled as "large aggregate-1"). Though the ESCs are similar, the ΔJ_{SC}% value with the large-size aggregate is almost 3 times that of the small-size aggregate (31.5% vs. 11.3%). The larger enhancement is likely related to the higher extent of CT states formed in large-size aggregates and the resulted more efficient electron injection from CT states to the TiO_2.

Interestingly, at the full monolayer coverage (i.e., 100% ESC), the solar cells sensitized with both small- and large-size LHCII aggregates (i.e., "small aggregate-2" and "large aggregate-2") showed almost the same ΔJ_{SC}% values (57.7% vs. 58.2%). Since the packing density of the LHCII trimer on the TiO_2 surface is nearly the same, no matter if they are originally from small- or large-size aggregates, the CT states at this condition are about the same as well. It is noteworthy

that the power conversion efficiency is increased by ~58% from the bare APTES-TiO_2 cell after being sensitized with a full monolayer of LHCII aggregates, which is higher than the 35% increase using LHCII trimers as a sensitizer on the 10 μm thick mesoporous TiO_2 film[45].

To identify the origin of the photocurrent generation, the synchronous response of J_{SC} to the illumination of the full solar spectrum and in selected wavelength bands were recorded and illustrated in Figure 3.7. The current density is normalized to the photocurrent of the solar cell with bare APTES-TiO_2 photoanodes in order to correct the variation of TiO_2 photoanode (see Figure A.5 in Appendix A for normalization processing). All photocurrents were highly reproducible as the illumination was turned on and off for four cycles. Only a very slow drift was observed during the illumination *on,* indicating that LHCII complexes were stable under the experimental conditions and were effectively regenerated by iodide/tri-iodide redox electrolyte. Under 1 sun illumination with the full solar spectrum (Figure 3.7A), all curves showed higher photocurrent after LHCII sensitization, fully consistent with the I-V measurements in Figure 3.6. The cell "large aggregate-1" (ESC = 48.3%) gave significantly higher normalized current density than "small aggregate-1" (ESC = 45.8%), though both of them had similar level of LHCII coverage. The curves for the cells with the full LHCII monolayer coverage, i.e., "small aggregate-2" and "large aggregate-2", are essentially overlapped with each other.

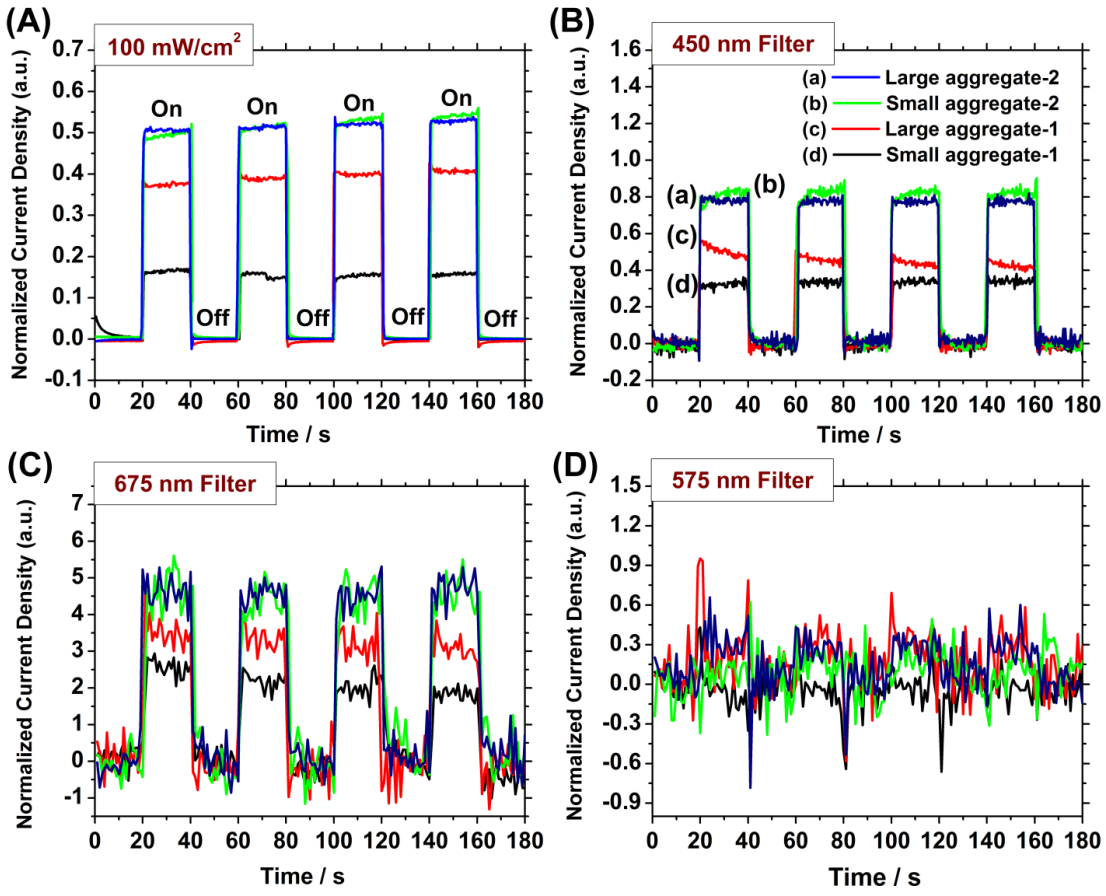

Figure 3.7 Synchronous photocurrent responses of the TiO_2 solar cells sensitized with different ESC% of small- and large-sized LHCII aggregates.

The measurements performed under 1 sun illumination with the full solar spectrum (A) and passing through bandpass interference filters at 450±25 nm (B); 675±25 nm (C); and 575±25 nm (D). The photocurrents were normalized as described in the SI (see Figure S5). "On" and "Off" refer to illuminated and dark conditions, respectively. (Reprinted with permission from Y. Yang, R. Jankowiak, C. Lin, K. Pawlak, M. Reus, A. R. Holzwarthb and J. Li, *Phys. Chem. Chem. Phys.*, 2014, 16, 20856-20865.)

In addition to the full solar spectrum, three bandpass interference filters were applied to limit the illumination to three narrow wavelength regions. The chosen illumination ranges are 450±25 nm (Soret region of Chls), 675±25 nm (Q_y region of Chls), and 575±25 nm (region with minimum absorbance), in accordance with the shaded areas in the LHCII absorption spectra shown in Figure 3.2. Figures 3.7B and 3.7C clearly demonstrated that the photocurrent response can be attributed to the absorbance of LHCII proteins. The correlation of the photocurrent magnitude and

the LHCII coverage, as well as the degree of aggregation, agreed well with that of the full solar spectrum. The illumination in the 575±25 nm region, which has minimum photon absorption by LHCII, however, did not generate any photocurrent (Figure 3.7D).

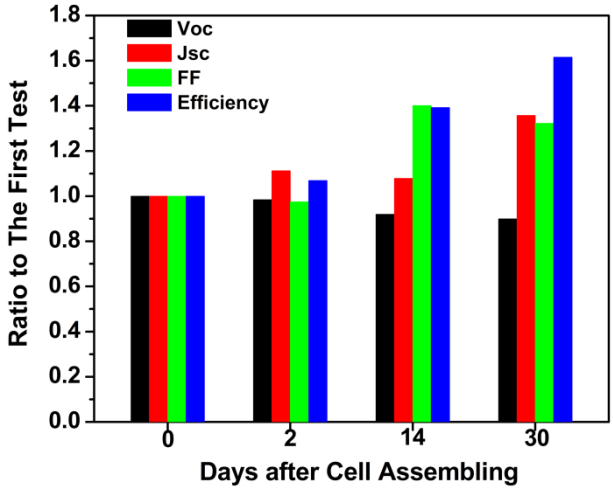

Figure 3.8 The performance characteristics of LHCII-sensitized TiO_2 solar cells measured over 30 days after assembly.

All parameters were normalized to the value obtained with the cell immediately after it was assembled. (Reprinted with permission from Y. Yang, R. Jankowiak, C. Lin, K. Pawlak, M. Reus, A. R. Holzwarthb and J. Li, *Phys. Chem. Chem. Phys.*, 2014, 16, 20856-20865.)

Proteins are normally unstable and tend to denature in organic solvents such as acetonitrile. However, we found that LHCIIs were extremely robust (regarding photocurrent generation) after they were attached to the APTES-TiO_2 surface, which was critical for LHCII-sensitized solar cell to work well in acetonitrile based Iodolyte. That is, a possible denaturation (that cannot be fully excluded) did not affect the performance of our photovoltaic devices. Figure 3.8 illustrates the characteristic photovoltaic properties of the solar cell "Small aggregate-1" (i.e., 45.8% ESC of small-size LHCII aggregates) over 30 days after assembly. In fact, not only did the cell display an outstanding stability, but the overall cell performance improved with time as demonstrated by the increase in J_{SC}, FF, and PCE (η). Only V_{OC} slightly decreased. In these experiments, the only effort to avoid cell degradation was to replace Iodolyte with tricine buffer after each photovoltaic

measurement and store them at 4º C before refilling Iodolyte for the next measurement. Continued reorganization of LHCII complexes could occur during this period, allowing more CT states formation or a better contact to the TiO_2 surface, leading to an improved cell performance.

To further understand the effects of LHCII reorganization, a TiO_2 solar cell sensitized with isolated chlorophyll pigments was also prepared and tested by the same procedure as a control. Since Chl *a* and Chl *b* are the two major light-harvesting pigments in LHCII complex (with a molar ratio of 8 : 6), the bare TiO_2 solar cell was thus sensitized in a dry diethyl ether solution with a total Chl concentration of 120 μg Chl/mL at 8:6 molar ratio of.Chl *a* and Chl *b*. As shown in Figure A.6 of the Appendix A, although Chls did enhance the photocurrent of the solar cell at the beginning, the current kept decreasing in the following 5 days (120 hours). The current response curves illustrated that the contribution of Chls to photocurrent almost became negligible after 72 hrs. It should be noted that Chls attached onto the TiO_2 layer only through weak physisorption tend to desorb over time and are easily oxidized in atmosphere. Compared with the LHCII-sensitized solar cells discussed above, the stability of the Chl-sensitized solar cell was very poor, which illustrated the necessity of using photosynthetic protein complexes instead of Chl pigments alone.

3.4 Conclusions

LHCII complexes with different degrees of aggregation were respectively applied onto a model thin film TiO_2 solar cell. The results not only illustrated that LHCII can serve as a remarkably stable photosensitizer for DSSCs, but also revealed that the photovoltaic properties of this system, represented by the photocurrent enhancement, can be directly correlated to the aggregation induced CT states. The existence of the CT states must have improved the electron injection into TiO_2, since the photocurrent generated by large-size LHCII aggregates was

significantly higher than the same amount of small-size LHCII aggregates. We emphasize that formation of CT states in aggregated LHCII complexes is consistent with the observed strong electron-phonon coupling and much weaker (red-shifted) fluorescence emission observed in aggregated LHCII complexes at low temperatures.[89] More CT states formed by a possible LHCII reorganization or a better contact to the photoanode are likely responsible for the high stability and continuously increased performance of the solar cell after assembling. Our LHCII sensitized solar cell adopted a thin film design to reduce the background current from the traditional mesoporous TiO_2 layer and amplify the contribution from sensitizing protein complexes. This design should be also applicable to other photosynthesis protein complexes, which provides a new platform to tap into the early biophysical processes of photosystems, i.e., the photon capture and energy/charge transfer.

Chapter 4 - Plasmonic Enhancement of Biosolar Cells Employing LHCII Incorporated with Core-Shell Metal@TiO_2 Nanoparticles[‡]

4.1 Introduction

While interfacing photosynthetic proteins with artificial DSSCs has provided inspiring insights into development of bio-solar cells, the overall PCE of such devices is still too low compared to the traditional DSSCs relying on using synthesized dye molecules (such as N719)[36] as light harvesting antennas. Strong efforts in current research have been placed on boosting light harvesting of photosynthetic proteins. For example, since adsorption of the photosynthetic proteins onto internal surface of the mesoporous TiO_2 anode is hindered by its much larger size (4 – 6 nm) than dye molecules (< 1 nm), researchers strive to increase their loading capacity by engineering more open three-dimensional (3D) electrode architecture and improving protein binding to the electrode surface.[57] Furthermore, studies have shown that SPR of gold or silver nanoparticles enormously alters the light absorption and fluorescence emission of photosynthetic proteins near the nanoparticle surface.[96] Hybrid systems with PSI attached to PNPs displayed increased light absorption over the entire absorption band.[97] Approximately 10- to 20-fold enhancements in fluorescence intensity were observed for LHCs placed on the film of silver or gold islands.[98-100] A theoretical model for SPR-enhanced free electron production and photocurrent generation was proposed based on PSI-RCs bound to Au and Ag nanocrystals.[101] The internal photosynthetic

[‡] Reproduced in part by permission of the John Wiley and Sons, Y. Yang, H. Gobeze, F. D'Souza, R. Jankowiak and J. Li, Plasmonic Enhancement of Biosolar Cells Employing Light Harvesting Complex II Incorporated with Core-Shell Metal@TiO_2 Nanoparticles, *Adv Mater Interfaces*, DOI: 10.1002/admi.201600371

efficiency of PSI-RC was strongly enhanced by the metal nanoparticles, which involved two competing effects, i.e. plasmon enhanced light absorption of Chl molecules and energy transfer from Chl to metal nanoparticles.[101] The proposed mechanism provides useful insights into energy-conversion devices involving the photosynthetic proteins, but is controversial with other studies. Here we employ LHCIIs alone (without RCs) electrostatically conjugated onto the TiO_2-coated PNPs to maximize both light harvesting and energy transfer from LHCII to TiO_2 by plasmonic effects of PNPs.

PNPs have been widely employed in new emerging photovoltaic devices to enhance the performance, including DSSCs[61, 71, 102] and Perovskite solar cells.[103-104] Recently, Adhyaksa et al. reported a biosolar cell using natural extract graminoids coupled with silver nanoparticles to achieve larger photocurrents.[105] However, the explanation of the interplays between PNPs and different light harvesting antennas varied in each specific cases. Compared to synthetic light harvesting molecules, photosynthetic complexes containing multiple pigments are much more complicated. Studies on model systems are necessary to uncover the mechinism of SPR effects on the photovoltaic properties of the bio-solar cells. In this work, three kinds of PNPs, including gold nanospheres (AuNSs), silver nanospheres (AgNSs) and silver nanoplates (AgNPs), were synthsized to achieve tailored SPR characteristics relative to the UV-Vis absorption spectrum of LHCII trimers. The PNPs were coated with a thin TiO_2 barrier layer to form core-shell strucures, which were further assembled into LHCII-PNP hybrids in solutions for spectroscopic characterization. The PNPs were then incorporated in LHCII-sensitized solar cells (LSSCs) on a 3D photoanode consisting of verically grown TiO_2 nanotrees. The combined information helps to understand the energy transfer (ET), charge seperation and current collection processes of the

hybrid system. It has demonstrated that the electron injection from LHCII into TiO_2 is substantially enhanced by the SPR of PNPs.

4.2 Experimental Details

4.2.1 Synthesis of Plasmonic Nanoparticles (PNPs): AgNS@TiO_2, AuNS@TiO_2 and AgNP@TiO_2

The core-shell PNPs used in this work are composed of different metal cores, i.e. silver nanosphere (AgNS), gold nanosphere (AuNS) and silver nanoplate (AgNP), and a thin TiO_2 shell, termed as AgNS@TiO_2, AuNS@TiO_2 and AgNP@TiO_2.

AgNSs were synthesized by a reported method.[73] First, 0.017 g of silver nitrate was dissolved into 25 mL of ethylene glycol solution containing 0.5 g of Polyvinylpyrrolidone (PVP-40 with an average molecular weight of 40,000). Then the solution was slowly heated up to 120 ℃ and kept at that temperature for 1 h with constant stirring. After the reaction, the as-prepared AgNSs were washed with acetone (200 mL of acetone per 25 mL of reaction mixture) and subsequently centrifuged at 3000 rpm. The supernatant was removed, and the AgNSs were rinsed with ethanol, centrifuged at 3000 rpm, and redispersed in ethanol.

AuNSs were prepared by citrate reduction of $HAuCl_4$ in aqueous solution.[19] 0.2 mL of $HAuCl_4$ solution (50 mg/mL) was added into 100 mL of boiling water rapidly, followed by adding 3 mL of trisodium citrate solution (1 wt%). The mixture was kept boiling with stirring for 30 min to form Au seeds. Then the temperature of the bath was decreased to 90 ℃. 3 mL of 1 wt% sodium citrate and 0.2 mL of 50 mg/mL $HAuCl_4$ solution were simultaneously added to the mixture again. This procedure was repeated 3 times to attain ~20 nm AuNSs. The AuNSs were then purified by centrifugation, rinsing and redispersed in ethanol.

For AgNP synthesis, the total volume of the reaction solution was fixed at 25.00 mL. In 24.04 mL of pure water, an aqueous solution of silver nitrate (0.05 M, 50 μL), trisodium citrate (75 mM, 0.5 mL), PVP-40 (17.5 mM, 0.1 mL), and H_2O_2 (30 wt %, 60 μL) were combined and vigorously stirred at room temperature in air. Sodium borohydride ($NaBH_4$, 100 mM, 250 μL) is rapidly injected into this mixture to get the nanoplates. A series of color change of the solution was observed similar as reported.[106]

PNPs with the core-shell structure were synthesized by coating a thin TiO_2 layer (2~5 nm) on the as-prepared AgNSs, AuNSs and AgNPs. About 12 μL of TTIP in 1 mL ethanol was added to the ethanolic solution of AgNS, AuNS and AgNP, respectively. The reaction sustained for 12 hours at room temperature under steady stir. The particles were purified with ethanol washing and centrifugation for three times. In order to increase the interaction between LHCII and PNPs, the surface of AgNS@TiO_2, AuNS@TiO_2 and AgNP@TiO_2 particles was further functionalized with amine groups by incubating the particles in 5 wt% APTES ethanolic solution for 30 min at 60℃ and then washed with ethanol and redispersed in water.

4.2.2 Preparation of LHCII Trimer Solution

The LHCII trimers were extracted from spinach thylakoids as described in the literature[90] and were dispersed in 5 mM tricine buffer (pH = 7.5) with a detergent, i.e. 0.1 M sucrose and 0.06% n-dodecyl β-D-maltoside (β-DM). The concentration of LHCII, in unit of equivalent Chl concentration, were derived from the absorbance measured with the same procedure described in our previous paper[107] using buffered aqueous acetone (80% aqueous acetone containing 2.5 mM phosphate buffer with pH = 7.8) as chlorophyll extractant.

4.2.3 Plasmon-Enhanced LHCII Sensitized Solar Cell

The TiO_2 nanotree array grown on FTO glass was used as the photoanode in this work, of which the fabrication was described in Section 2.4 of Chapter 3. To increase the adsorption of LHCII, the TiO_2 nanotrees were first treated with 5 wt% APTES, and then incubated in LHCII trimer solution under dark for 24 h at room temperature. The solutions of APTES-treated PNPs ($AgNS@TiO_2$, $AuNP@TiO_2$ and $AgNP@TiO_2$, respectively) with the metal content corresponding to ~1 wt% of the total mass of TiO_2 in the photoanode were casted onto the LHCII sensitized TiO_2 nanotrees. With the APTES treatment, PNPs tend to adsorb on top of LHCII trimers. The photoanode was then rinsed with water to remove weakly adsorbed LHCII trimers and PNPs, and finally dried with N_2 flow.

A 20 nm thick Pt film sputtered on the FTO glass by a high resolution ion beam coater (Model 681, Gatan Inc., Pleasanton, CA) was applied as the cathode. The photoanode and cathode were assembled with a 1×1 cm^2 window cut in a 250 μm-thick silicone gasket (Solaronix, Switzerland). Iodide based ionic liquid electrolyte (Mosalyte TDE-250, Solaronix, Switzerland) was injected into the cell by a syringe through two holes drilled on the cathode. The assembled cell was masked to define an active area of 0.2 cm^2.

4.2.4 Material Characterization

The morphology of the core-shell PNPs was examined with high resolution transmission electron microscopy (HRTEM, JEM-2100 LaB6, JEOL USA, Peabody, MA). The TiO_2 photoanode was examined with a field-emission scanning electron microscopy (FESEM, Nano430, FEI, Hillsboro, OR) using a through-lens detector (TLD) for secondary electrons and a low-voltage high contrast detector (vCD) for backscattering electrons, which provide complementary information of the 3D structure. UV-Vis absorption spectra were recorded at room

temperature using a DU 640 spectrophotometer (Beckman, Fullerton, CA). The steady-state fluorescence was recorded by using a Horiba Jobin Yvon Nanolog spectrofluorimeter equipped with PMT (for UV-visible) and InGaAs (for near-IR) detectors. The fluorescence lifetimes were measured with the Time Correlated Single Photon Counting (TCSPC) option with nano-LED excitation sources on the Nanolog. All the solutions were purged prior to spectral measurements using argon gas. The atomic composition and PNP particle concentration were determined with an inductively coupled plasma-atomic emission spectrometer (ICP-AES, 720-ES, Varian, Walnut Creek, CA). The crystalline structure of the TiO_2 nanotrees were determined by powder x-ray diffraction (D8, Bruker, Madison, WI) and Raman spectroscopy (DXR Raman microscope, Thermal Scientific, Waltham, MA).

4.2.5 Transient Absorption Measurements

Femtosecond pump-probe experiments were performed using an Ultrafast Femtosecond Laser Source (Libra) by Coherent combining a diode-pumped, mode locked Ti:Sapphire laser (Vitesse) and diode-pumped intra cavity doubled Nd:YLF laser (Evolution) to produce a compressed laser output of 1.45 W. For optical detection, a Helios transient absorption spectrometer coupled with a second and third harmonics generator, both provided by Ultrafast Systems was used. The source for the pump and probe pulses were derived from the fundamental output of Libra (Compressed output 1.45 W, pulse width 100 fs) at a repetition rate of 1 kHz. About 95% of the fundamental output of the laser was introduced into a harmonic generator to produce the second and third harmonics of 400 and 267 nm besides the fundamental 800 nm for excitation. The rest of the output was used for generation of white light continuum. In the present study, the second harmonic output (400 nm) was used as excitation pump source. Kinetic profiles at appropriate wavelengths were assembled from the time-resolved spectral data. Data analysis

was carried out using Surface Xplorer software from Ultrafast Systems. All spectral measurements were performed at room temperature in Ar-saturated solutions.

4.2.6 Solar Cell Characterization

Cell performance was evaluated with the characteristics of photocurrent-voltage (I-V) curve measured with a CHI 440A potentiostat (CH Instruments, Austin, TX) under one-sun (100 mW/cm^2) illumination using a solar simulator consisting of a 300 W Xe lamp and an AM 1.5G filter (Newport, Irvine, CA). Three different bandpass interference filters with 50 nm FWHM (Edmund Optics, Barrington, NJ) were employed to select specific wavelength range of 450 ± 25 nm, 575 ± 25 nm, and 675 ± 25 nm, respectively, and the dynamic responses of short-circuit current (J_{SC}) were monitored with chronoamperometry measurements while the shutter was turned on and off. The incident photon-to-current efficiency (IPCE) at various wavelengths was collected with irradiation of a 75 W Xe lamp and a monochromator (74004, Oriel Instrument, Newport, Irvine, CA).

4.3 Results and Discussion

4.3.1 Characterization of the Structure of Core-Shell PNPs.

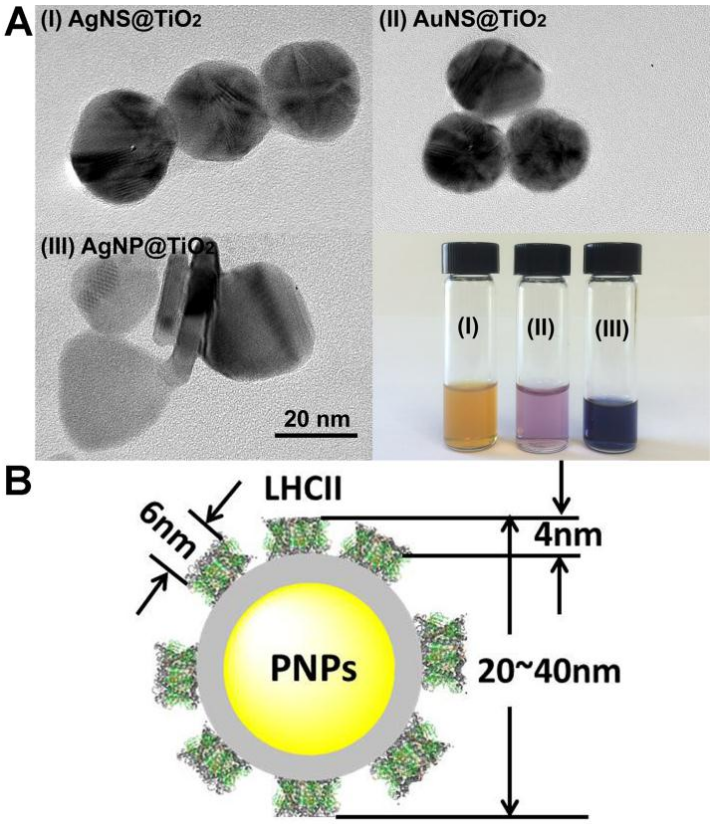

Figure 4.1 Dimensional morphology and color of three core-shell plasmonic nanoparticles. (A) TEM images of AgNS@TiO_2 (I), AuNS@TiO_2 (II) and AgNP@TiO_2 (III), and the photograph of the corresponding particles dispersed in aqueous solution. (B) Schematic structure of the LHCII-PNP hybrid systems. (Reprinted with permission from Y. Yang, H. Gobeze, F. D'Souza, R. Jankowiak and J. Li, *Adv. Mater. Interfaces*, DOI: 10.1002/admi.201600371)

The transmission electron microscopy (TEM) images in Figure 4.1 exhibit the representative morphologies of the as-prepared PNPs. The average diameters of the spherical PNPs are 23.4±2.5 and 22.0±1.6 nm for AgNS@TiO_2 and AuNS@TiO_2, respectively. The TEM image of AgNP@TiO_2 PNPs (left bottom panel) shows that some PNPs lie flat and some stand vertically on the TEM grid, confirming that they have a flat plate-like shape of 27.3±10 nm in diameter and

5.6±0.9 nm in thickness. The solutions of these PNPs exhibit orange (AgNS@TiO_2), purple (AuNS@TiO_2) and navy blue color (AgNP@TiO_2), respectively. The PNP concentrations were determined by inductively coupled plasma atomic emission spectroscopy (ICP-AES) and summarized in the Appendix B-Table B.1. The core-shell structure of the PNPs was demonstrated by high-resolution TEM images in Appendix B-Figure B.1. A thin TiO_2 shell of about 2~3 nm can be observed on the surface of metallic cores. Soaking these PNPs in iodide solutions overnight did not show significant decrease in the SPR peak height, which further confirms that the TiO_2 shell fully covers the metallic cores and is effective in protecting them from etching by electrolytes. Compared with the bare Ag nanoparticles used in Adhyaksa's work,[105] this core-shell structure has multiple functions. First, the hydrophilic nature of TiO_2 shell makes the PNP surface biocompatible for protein attachment.[108] Second, the semiconductive TiO_2 shell serves as an energy barrier to prevent unwanted electron flow from the attached proteins to the metallic core.[70] Third, the TiO_2 shell acts as a protective armor to ensure the stability of the metallic core in the corrosive iodide electrolytes in solar cells.[45]

It is noteworthy that LHCII only weakly adsorbs to the native TiO_2 surface, as we reported before.[107] To overcome this issue, a positively charged amine group ($-NH_3^+$) was introduced to the TiO_2 surface of PNPs by functionalization with APTES. The affinity of LHCII to TiO_2 surface is largely increased due to electrostatic interaction between the negatively charged carboxylate groups ($-COO^-$) in LHCII and the $-NH_3^+$ group on the surface. For direct quantitative comparison, the PNP solutions used in later spectroscopic studies were controlled to have similar TiO_2 surface area so that the amount of attached LHCII is about the same. Figure 1B schematically depicted the structure and relative dimension of the LHCII-PNP hybrid system consisting of LHCII trimers adsorbed on the TiO_2 shell of PNPs. To further ensure forming a close-packed monolayer of LHCII

trimers on the surface of APTES-functionalized core-shell PNPs, we intentionally added redundant LHCII trimers in the solution during LHCII-PNP hybrid formation. It is estimated that, in the final LHCII-PNP solutions, ~20% of LHCII are absorbed on the PNP surface while the other ~80% of LHCII remain freely dispersed in solution.

4.3.2 Optical Spectroscopic Properties of LHCII-PNP Hybrids.

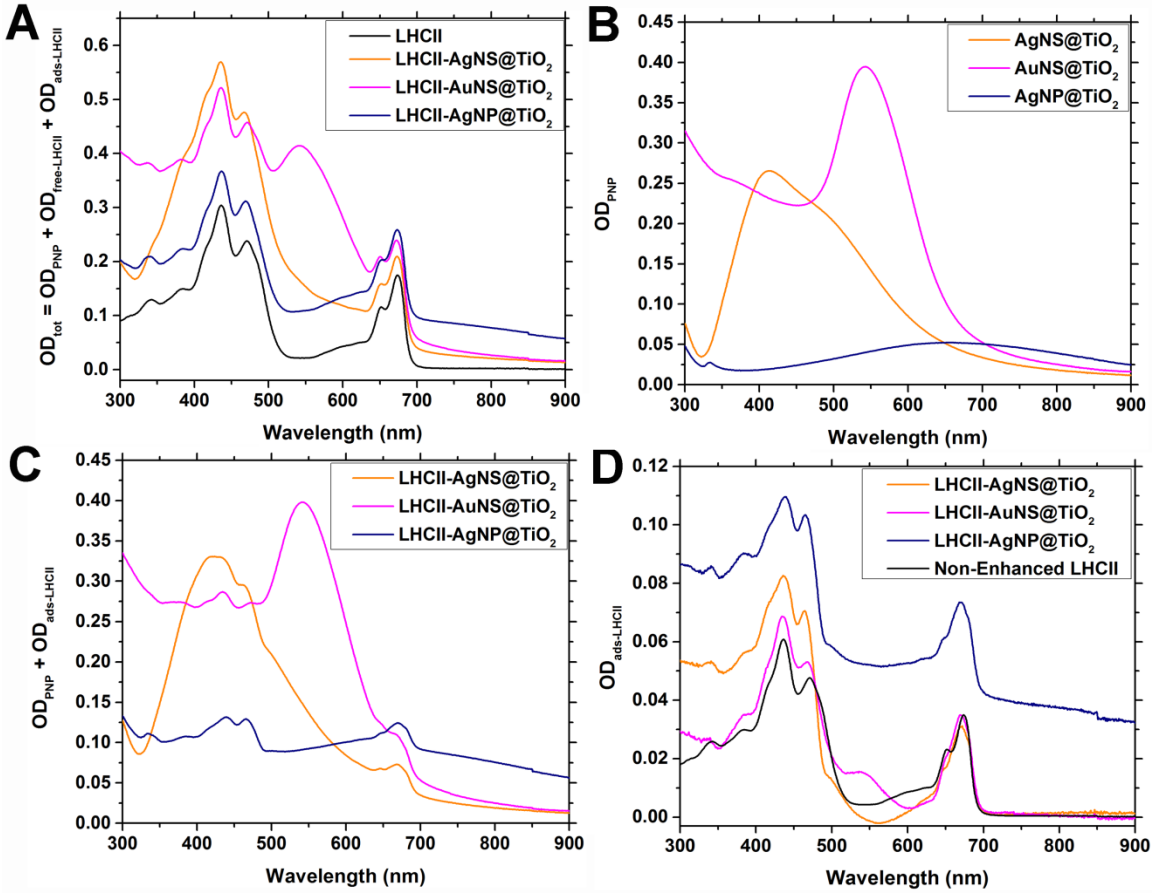

Figure 4.2 Absorption properties of the LHCII-PNP hybrids.

(A) UV-Vis absorption spectra of free LHCII trimers and LHCII-PNP hybrids in aqueous solutions. OD_{tot} stands for total optical density that is the sum of the OD of PNPs (OD_{PNP}), free LHCII trimers ($OD_{free\text{-}LHCII}$) and LHCII adsorbed on PNP ($OD_{ads\text{-}LHCII}$). (B) Plasmonic absorption spectra of the bare core-shell PNPs in aqueous solutions (OD_{PNP}), with the PNP concentrations same as those of the LHCII-PNP hybrids in (A). (C) The net absorption of LHCII-PNP hybrids after subtracting the contribution from free LHCII in solution, with $OD_{ads\text{-}LHCII} + OD_{PNP} = OD_{tot} - 80\%OD_{LHCII}$, where 80% accounts for the approximate portion of LHCII remaining freely dispersed in solution. (D) The enhanced absorption of LHCII adsorbed on PNP, with $OD_{ads\text{-}LHCII} = OD_{tot} - 80\%OD_{LHCII} - OD_{PNP}$. For comparison, the absorption of non-enhanced LHCII was calculated from $20\%OD_{LHCII}$. (Reprinted with

permission from Y. Yang, H. Gobeze, F. D'Souza, R. Jankowiak and J. Li, *Adv. Mater. Interfaces*, DOI: 10.1002/admi.201600371)

Figure 4.2A shows the UV-Vis absorption spectra of free LHCII trimer in comparison with three LHCII-PNP hybrid solutions. The absorption spectrum of LHCII trimer consists of the Soret band (at 436 nm for Chl *a* and 471 nm for Chl *b*) and Q band (at 673 nm for Chl *a* and 652 nm for Chl *b*) of the primary Chl pigments. Clearly, all LHCII-PNP curves shift upward, indicating that adding PNPs induces higher absorption than pure LHCII. In contrast, the absorption of the LHCII sample in visible wavelength range is unaffected by solid TiO_2 NPs in the solution except larger scattering. After subtracting the scattering, the absorption spectrum is completely overlapped with that of the pure LHCII solution, as shown in Appendix B-Figure B.2.

The absorption spectra of LHCII-PNP hybrids were considered as the convolution of the absorptions of LHCII adsorbed on PNPs ($OD_{ads\text{-}LHCII}$), free LHCII in solution ($OD_{free\text{-}LHCII}$), and the plasmonic absorption of PNPs (OD_{PNP}). To de-convolute the contributions of each component, we first subtracted the absorption of free LHCII remaining in the solution of LHCII-PNPs ($OD_{free\text{-}LHCII}$ = ~80%OD_{LHCII}) by calculating the differential optical density (OD) between the LHCII-PNP hybrids and pure LHCII solutions using $\Delta OD = OD_{tot} - 80\%OD_{LHCII}$. The extracted spectra of net LHCII-PNPs are shown in Figure 4.2C are attributed to the summation of $OD_{ads\text{-}LHCII}$ and OD_{PNP}. Though the general features of net LHCII-PNP spectra reflect the characteristics of both free LHCII and free PNPs, they seem not to be simply the summation of these two components. Further analyses were done by deducting the absorption of PNPs (OD_{PNP}, as shown in Figure 4.2B). The results are shown in Figure 4.2D, which represent the enhanced absorption attributed to the LHCII adsorbed on the PNP surface. The non-enhanced absorption from the same amount of free LHCII in solution (20%OD_{LHCII}) is plot in black line in Figure 4.2D as a reference. Interestingly, compared to free LHCII, the LHCII on AgNP@TiO_2 shows higher absorption over the whole

spectral range, those on AgNS@TiO_2 shows higher absorption in the short-wavelength range, while those on AuNS@TiO_2 shows small peak absorption in the mid-wavelength range. The LHCII absorption apparently was modulated by the PNPs.

The maximum absorption of AgNS@TiO_2 overlaps with the Soret band of Chls in LHCII, while the AgNP@TiO_2 has a broad absorption covering both Soret and Q bands. The maximum absorption of AuNS@TiO_2 locates in the "dark region" between Soret and Q bands, where LHCII has the minimum absorption. Therefore, the increased absorption may be attributed to the enhanced photon harvesting induced by the SPR effects of the PNPs.[101] The slightly decreased absorptions in the mid-wavelength range for the LHCII on AgNS@TiO_2 and AgNS@TiO_2 are insignificant considering the experimental error. Although the LHCII on AuNS@TiO_2 exhibits negligible enhancement on its characteristic bands, the AuNS@TiO_2 PNPs are useful to fill the spectral gap in the wavelength range between 520 – 640 nm to capture the photons that cannot be effectively utilized by LHCII. Overall, these spectral characteristics imply that the photon capture by LHCII-PNP hybrids can be effectively tuned by controlling the core materials and particle morphology.

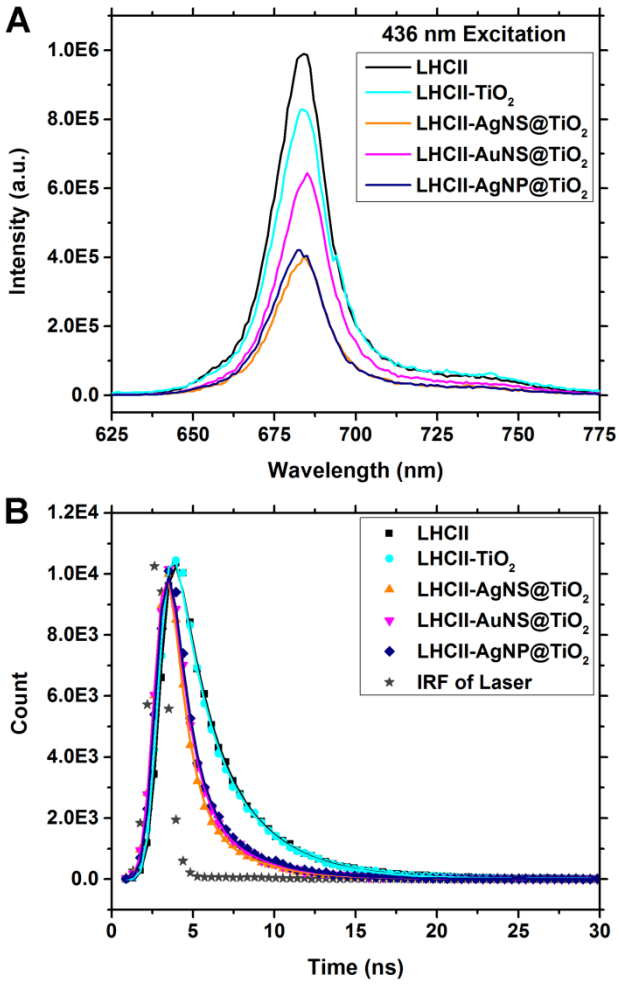

Figure 4.3 Emission properties of three LHCII-PNP hybrids.

(A) Steady-state fluorescence emission spectra of the aqueous solution of LHCII, TiO_2 NP and three types of core-shell LHCII-PNP hybrids. The LHCII absorbance was set to 0.1 in all of the samples excited at 436 nm. (B) Fluorescence decay curves after the samples were excited with a nanoLED operating at 494 nm wavelength. The instrument response function (IRF) (black stars) shows that the instrument has a much higher temporal resolution. (Reprinted with permission from Y. Yang, H. Gobeze, F. D'Souza, R. Jankowiak and J. Li, *Adv. Mater. Interfaces*, DOI: 10.1002/admi.201600371)

Figure 4.3A shows the steady-state fluorescence emission spectra of LHCII, LHCII-TiO_2 NP and LHCII-PNP hybrids in aqueous solutions. Even though it was excited at 436 nm, all emission occurs at ~683 nm with similar peak shapes, implying that the spectroscopic properties of LHCII were not significantly affected after attaching onto the TiO_2 surface. However, a

reduction of the fluorescence intensity was clearly observed after LHCII adsorbed onto TiO_2 NPs, and it became more significant in LHCII-PNP hybrids. Excitation at other wavelengths including 471, 542, and 673 nm all generates fluorescence with the origin band near 683 nm, with the similar trend of quenching by TiO_2 NPs and various PNPs, as summarized in Appendix B-Figure B.3. The time-resolved emission of LHCII at 683 nm using time-correlated single photon counting (TCSPC) reveals faster emission decays in the presence of various core-shell PNPs (Figure 4.3B). The decay curves can be fitted with two or three exponential function to derive the mean weighted lifetime τ_{Av} (see Table 4.1), which are 3.3 ± 0.5 ns for the pure LHCII, 2.6 ± 0.4 ns for LHCII with solid TiO_2 NPs, and smaller values from 1.2 ± 0.2 to 1.5 ± 0.2 ns for the core-shell PNPs. The two sets of fluorescence measurements in Figure 4.3 are in good agreement with each other, showing quenching of fluorescence intensity and reduced fluorescence lifetime of excited LHCII after they adsorbed onto TiO_2 surface; the latter effects were clearly enhanced by plasmonic cores.

Table 4.1 Mean weighted lifetime (τ_{Av}) of LHCII, LHCII-TiO_2 NP and LHCII-PNP hybrids.

Systems	τ_{Av} (ns)
LHCII	3.3 ± 0.5
LHCII-TiO_2	2.6 ± 0.4
LHCII-AgNS@TiO_2	1.2 ± 0.2
LHCII-AuNS@TiO_2	1.4 ± 0.2
LHCII-AgNP@TiO_2	1.5 ± 0.2

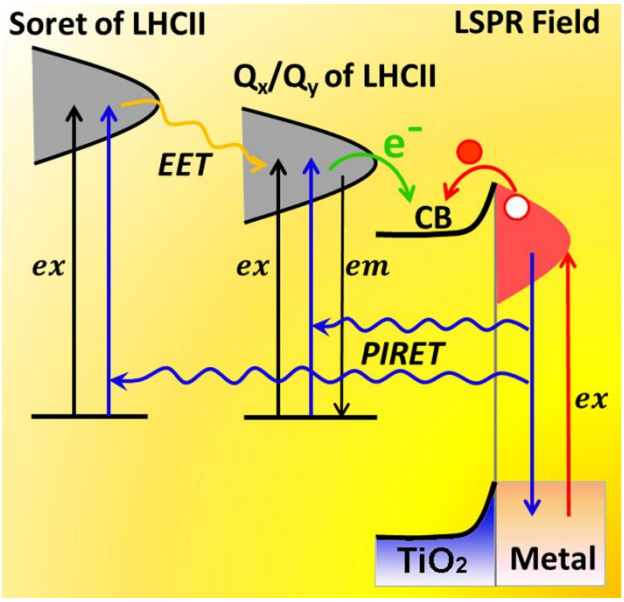

Figure 4.4 Schematic diagram of the energy and electron pathways in LHCII-PNP hybrid system.

The excitation of LHCII trimers is mostly due to strong absorption around the Soret band and Q band of the Chls (black upward arrows). These are followed by an ultrafast EET from Soret band to Q band (yellow arrow) and fluorescence emission (black downward arrow) to return to the ground level. After attaching LHCII to TiO_2 NPs or the core-shell PNPs, it induces a charge transfer process, i.e. injection of excited electrons in Q band to the conduction band (CB) of TiO_2 (green arrow), resulting in the reduced fluorescence intensity. In presence of the metallic core, the further excitation to LHCII may occur due to plasmon-induced resonance energy transfer (PIRET) from PNPs to LHCII (blue arrows), resulting in larger electron injection from LHCII to TiO_2. The charge carrier density in TiO_2 may be increased due to the injection of hot electrons excited at the metal core of PNPs as they overcome the Schottky barrier (red arrows). (Reprinted with permission from Y. Yang, H. Gobeze, F. D'Souza, R. Jankowiak and J. Li, *Adv. Mater. Interfaces*, DOI: 10.1002/admi.201600371)

From the optical spectroscopic results in Figures 4.2 and 4.3, it is clear that PNPs provide additional photon capture to LHCII with the spectral overlap at different regions. However, the extra photon energy harvested by PNPs does not simply enhance the excitation (i.e. absorption) of LHCII and relaxed by radiative electron recombination that leads to higher fluorescence emission. Instead, the observed fluorescence emission decreases. Obviously there must be other mechanisms involved in LHCII-PNP hybrids which cause fluorescence quenching instead of enhancement. As

elaborated by Cushing et al[109-110], when a plasmonic metal NP is coupled to semiconductor, charge generation in semiconductor can be enhanced via three mechanisms, including light trapping based on scattering, hot electron/hole transfer, and plasmon-induced resonance energy transfer (PIRET) based on near-field. These are also applicable to the LHCII-PNP hybrids, with the possible mechanisms illustrated by the schematic energy diagram and electron pathways in Figure 4.4. If only LHCII is present in solution, the excitation process pumps electrons from the ground state to the excited states of Soret band or Q band. The excitation of the Soret band is followed by internal conversion and ultrafast excitation energy transfer (EET) to the Q band with assistance of carotenoids contained in LHCII trimer, as was proposed and verified by a theoretical modeling.[111] Thus all fluorescence emission bands from LHCIIs were at 683 nm, corresponding to a radiative relaxation by returning the excited electrons from Q band to the ground state.

When LHCII is adsorbed on the TiO_2 surface, upon excitation a charge transfer process occurs, i.e. the excited electrons in Q band are injected to the conduction band (CB) of TiO_2, resulting in the reduced fluorescence intensity. In presence of the metallic core, the incident photon energy captured by plasmonic absorption generates strong near-field oscillation which can reach up to ~10 nm decay length, affecting all LHCII adsorbed on the surface of the ~2-3 nm thick TiO_2 shell. The strong dipole-dipole coupling between the plasmon and LHCII induces a strong PIRET to enhance the excitation of LHCII at either Soret or Q bands. The strong near-field likely facilitates more efficient electron injection from LHCII to TiO_2 and thus lowers the overall fluorescence intensity even though additional LHCII excitation is induced by PIRET. These processes are beneficial in enhancing the photocurrent generation in plasmonic LSSCs as will be discussed later. The plasmonic hot electrons excited at the metal core of PNPs may also be easier to overcome the Schottky barrier at the metal-TiO_2 interface and raise the charge carrier density in

TiO_2 shell. Here we mainly focus on the plasmonic effects on LHCII in wavelength larger than 400 nm. Thus the PIRET from metal core to TiO_2 at shorter wavelength is neglected.

4.3.3 Femtosecond Transient Absorption Study.

In order to seek further evidence of charge injection from excited LHCII to TiO_2 NPs, femtosecond transient absorption studies were performed. In these studies, the samples were excited using 400 nm, 100 fs laser pulses where chlorophyll pigments of LHCII have a large absorbance. In order to identify the electron injection product, namely the oxidized LHCII species, LHCII was chemically oxidized using nitrosonium tetrafluoroborate (NTFB) as an oxidizing agent in water. As shown in Appendix B-Figure B.4a, adding more oxidizing agent resulted in decrease in intensity of LHCII peaks and appearance of new shoulder peaks at the longer wavelength side of the 472 and 674 nm LHCII peaks. In order to isolate the changes, the differential spectra were generated with ΔA = Abs(oxidized) - Abs(neutral), as shown in Figure B.4b. The negative peaks represent reduction in the amount of the neutral compound due to the oxidation process and the positive peaks represent absorbance due to the oxidized species. The appearance of the positive peaks during transient studies would serve as a proof of charge injection from excited LHCII to TiO_2 NPs.

Figure B.5a in the Appendix B shows femtosecond transient absorption spectra of LHCII in water at different delay times after excited with a short laser pulse. The spectra revealed instantaneous formation of a positive peak at 535 nm with negative peaks at 485 and ~680 nm (time constant ~1 ps). The positive peak has been attributed to the singlet-singlet transition of the chlorophyll pigment while the negative peaks are attributed to ground state bleaching. The 680 nm peak also has contributions from stimulated emission. The decay of the singlet excited peak and recovery of the ground state (represented by the decrease in the negative peak) appeared slightly

faster than that predicted from the lifetime values, perhaps due to some photobleaching by the intense laser light. Importantly, successful excitation of LHCII to populate the singlet excited state is witnessed.

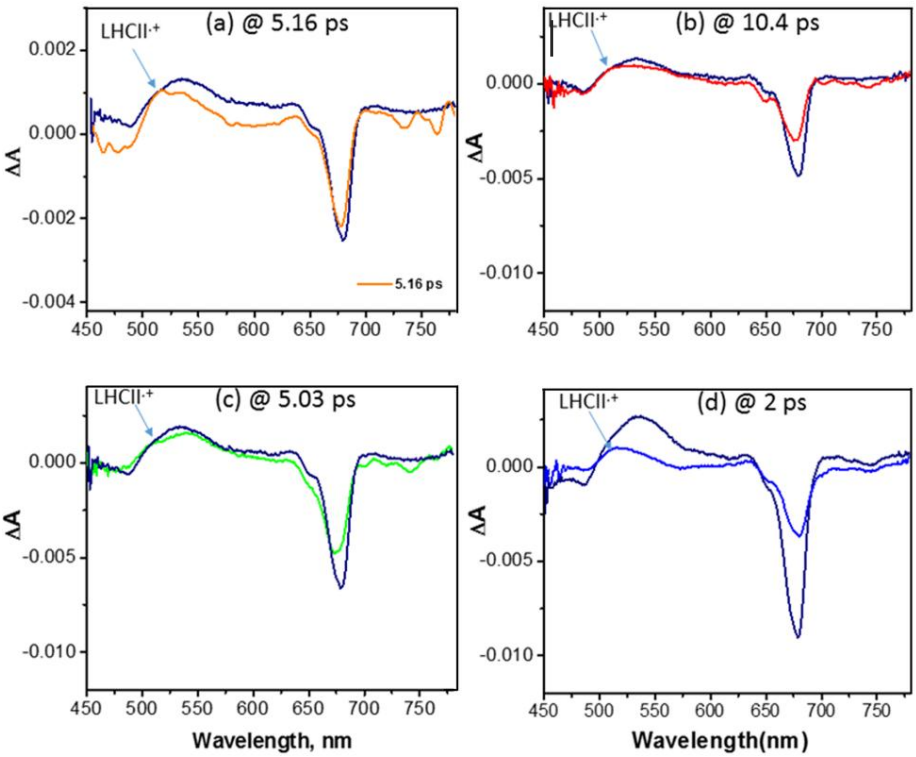

Figure 4.5 Femtosecond transient absorption spectra at the indicated delay time of LHCII and LHCII-PNP hybrids.

(A) LHCII and LHCII-TiO_2, (B) LHCII and LHCII-AgNS@TiO_2, (C) LHCII and LHCII-AuNS@TiO_2, and (D) LHCII and LHCII-AgNP@TiO_2 in Ar-saturated water. All LHCII spectra are shown in navy blue. (Reprinted with permission from Y. Yang, H. Gobeze, F. D'Souza, R. Jankowiak and J. Li, *Adv. Mater. Interfaces*, DOI: 10.1002/admi.201600371)

Figure 4.5 shows the transient absorption spectra of LHCII adsorbed on TiO_2 NPs and PNPs in water at the specified delay times. The spectrum of pristine LHCII solution is also shown at the same delay time for reference (see Figures B.5a-d in Appendix B for more spectra at a series of delay times of LHCII adsorbed on different core-shell PNPs). Two important observations were made. First, the decay of the 535 nm peak and the recovery of the negative peak at 680 nm of LHCII adsorbed on solid TiO_2 NPs and core-shell PNPs was faster than that observed for pristine

LHCII, suggesting involvement of excited LHCII in additional photochemical events. The time profiles of these peaks in comparison with pristine LHCII are shown in Appendix B-Figure B.6. In general, in accordance with the lifetime data, the metal NPs in TiO_2 accelerated the decay/recovery processes. Second, in the 500 nm range, positive absorbance appeared as a shoulder to the singlet-singlet peak of LHCII corresponding to the formation of $LHCII^{\bullet+}$. Other expected peaks of $LHCII^{\bullet+}$ around 660 and 680 nm were masked by the strong negative peak of excited LHCII. These results conclusively prove that there is charge injection from the excited LHCII into the conduction band of TiO_2 and that the metal NPs inside TiO_2 facilitate this photochemical event.

4.3.4 Design of Plasmon-Enhanced LHCII Sensitized Solar Cells

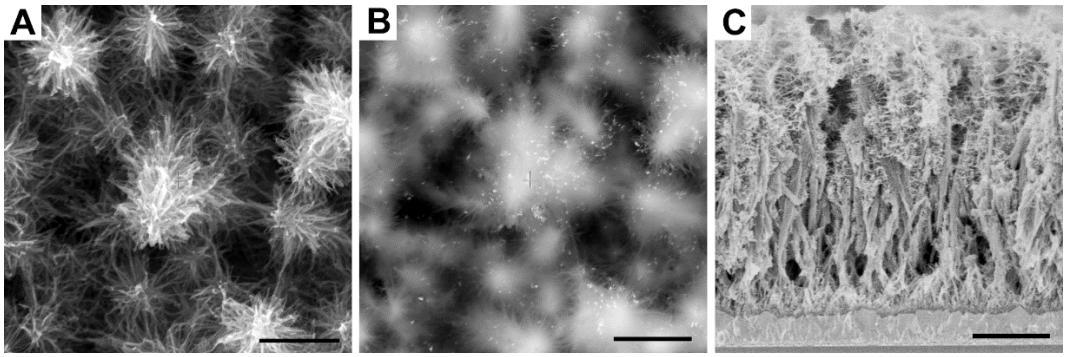

Figure 4.6 SEM images of the hydrothermally grown TiO_2 nanotrees on a FTO coated glass. (A) The top view (by measuring secondary electrons with a TLD detector), (B) the top view (by measuring backscattering electrons with a vCD detector), and (C) the cross-sectional view (by the TLD detector). The bright spots in (B) are well-dispersed PNPs on the TiO_2 nanotrees. All scale bars are 2 μm. (Reprinted with permission from Y. Yang, H. Gobeze, F. D'Souza, R. Jankowiak and J. Li, *Adv. Mater. Interfaces*, DOI: 10.1002/admi.201600371)

To further validate the importance of the SPR properties of the core-shell PNPs and utilizing them to enhance the LSSCs, we incorporated them into the photoanode (at ~1 wt% loading relative to the total TiO_2 total mass). In traditional DSSCs, a 20 μm thick film consisting of sintered TiO_2 nanoparticle with about 20 nm pore size is usually used as the photoanode material

for dye sensitization. Here, the LHCII trimer and the PNPs are both nanoparticles, much larger than organic dye molecules. To facilitate their penetrating through tortuous pores to access the internal surface of the whole TiO_2 film, we adopt a vertically-oriented TiO_2 nanotree array with much larger pore size as the photoanode. Such 3D hierarchical TiO_2 structures were directly grown on FTO coated glass substrates by an one-step hydrothermal reaction following a previous report.[112] The structure is illustrated by SEM images in Figure 4.6. The high-resolution secondary electron images in Figure 4.6A and C display the top and cross-sectional views of the synthesized TiO_2 nanotree array, showing a hierarchical structure composed of 6 μm-long TiO_2 trunk covered by short and thinner side branches. Large pores of several hundreds of nanometers between the neighboring TiO_2 nanotrees are preserved, leaving sufficient openings for electrolytes filling. Such structure has been used to improve the charge transfer while maintaining a high specific surface area, leading to enhanced charge collection efficiency in DSSCs sensitized with conventional ruthenium dye (N719).[113-114] The backscattering electron image in Figure 4.6B provides higher contrast, showing well-dispersed AuNS@TiO_2 PNPs as bright dots anchored on the TiO_2 branches. XRD and Raman characterizations in Appendix B-Figure B.7 confirmed that the TiO_2 nanotrees are highly crystalline anatase phase, which is ideal for DSSCs.

Figure 4.7 schematically depicts the structure and mechanism of the designed plasmonic LSSC with the PNPs drop-casted on the LHCII-sensitized TiO_2 nanotrees. The operation of LSSC includes three critical steps that may benefit from the unique properties of LHCII-PNP hybrids discussed earlier: (1) the enhanced photon capture, (2) fast energy transfer to excite Q band of LHCII trimers, and (3) more efficient charge separation at the LHCII/TiO_2 interface by plasmon promoted electron injection from LHCII into TiO_2. The other three steps follow the same mechanisms as traditional DSSCs, including (4) the injected electrons diffuse through the TiO_2

nanotrees to the current collector (FTO coated glass) and the external circuit to generate photocurrent, (5) regeneration of the oxidized LHCII trimers by filling electrons donated from iodide mediators in the electrolyte, and (6) transport of the oxidized iodide (i.e. triiodide) as the hole carrier to the cathode (Pt coated glass) and reducing it back to iodide to complete the circle.

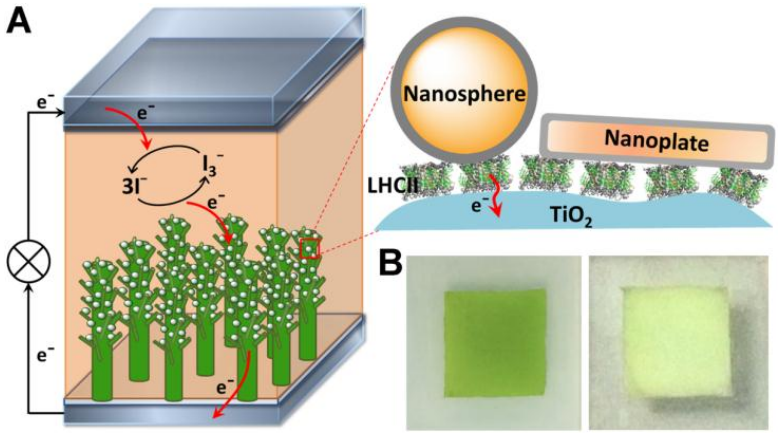

Figure 4.7 The structure of the plasmon-enhanced LHCII-sensitized solar cell and the appearance of the sensitized photoanode.

(A) The scheme of the solar cell. The enlarged portion (red square) shows the binding of different PNPs on LHCII-sensitized TiO_2 nanotrees and the electron injection from LHCII to TiO_2 (red arrow). (B) The digital photographs of the LHCII-sensitized region of an APTES-treated TiO_2 nanotree array (left) and a bare TiO_2 nanotree array (right). (Reprinted with permission from Y. Yang, H. Gobeze, F. D'Souza, R. Jankowiak and J. Li, *Adv. Mater. Interfaces*, DOI: 10.1002/admi.201600371)

As mentioned above, the adsorption of LHCII trimers on TiO_2 surface can be improved by APTES functionalization. It can be easily verified from the color of the LHCII sensitized film. A uniform greenish film was attained on APTES-treated TiO_2 nanotree array (see left frame of Figure 4.7B). In contrast, only a non-uniform dim green color was observed on the TiO_2 nanotree array without APTES functionalization (see right frame of Figure 4.7B). The amount of adsorbed LHCII was extracted into solutions and quantitatively assessed by the UV-Vis absorbance and illustrated in Appendix B-Figure B.8. The amount of LHCII trimers adsorbed on APTES-treated TiO_2 nanotrees was increased by 2.5 folds compared to that on bare TiO_2 nanotrees. Based on the

calculations, it requires LHCII trimers containing 0.2 μg Chls to form a hexagonal close-packed monolayer on a flat 1×1 cm^2 surface.[107] Here the adsorbed LHCII trimers were measured to be equivalent to 6.6 μg Chl, 33 times higher than that on the flat TiO_2 surface. Clearly, LHCII trimers were able to penetrate into the TiO_2 nanotree array and adsorb on a large surface area.

4.3.5 Photovoltaic Characterizations

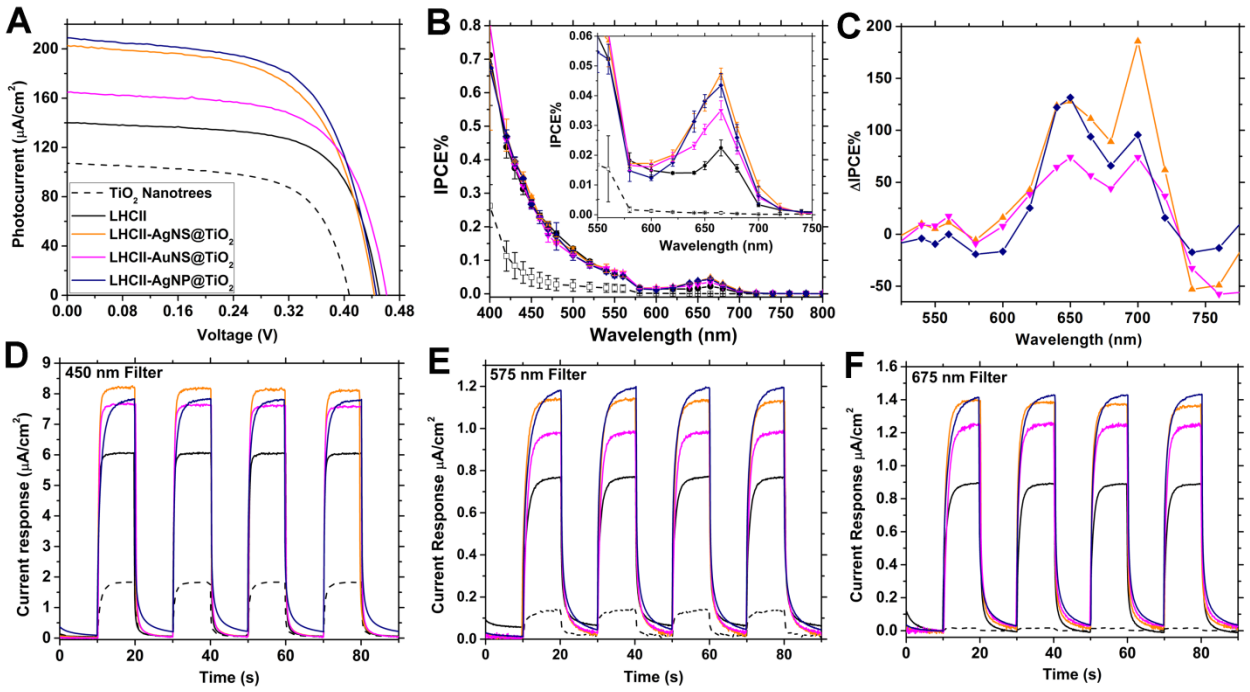

Figure 4.8 Photovoltaic performance of the plasmon-enhanced LSSCs.

(A) current-voltage (I-V) curves, (B) incident photon-to-current efficiency (IPCE) curves (inset: the enlargement from 550 to 750 nm), (C) the percentage change of IPCE (ΔIPCE%) of PNP-incorporated LSSCs relative to the normal LSSC. Synchronous response of the short-circuit photocurrent under illumination through bandpass interference filters for selecting wavelength at (D) 450 ±25 nm, (E) 575 ±25 nm, and (F) 675 ±25 nm. The illumination is altered between "On" and "Off" in about every 10 s using a shutter. The figure legends for all figures are the same as frame A. (Reprinted with permission from Y. Yang, H. Gobeze, F. D'Souza, R. Jankowiak and J. Li, *Adv. Mater. Interfaces*, DOI: 10.1002/admi.201600371)

The performance of the fabricated LSSC was characterized with I-V measurements in Figure 4.8A. Comparing to the bare TiO_2 device, both short circuit current (J_{sc}) and open circuit voltage (V_{oc}) increased by LHCII sensitization. Further photocurrent enhancement was realized by

incorporating PNPs in the LSSCs. The results from triplicated experiments showed that J_{sc} of the LSSCs with AgNS@TiO_2, AuNS@TiO_2 and AgNP@TiO_2 achieved 201±3, 173±9 and 208±11 μA/cm^2, respectively, representing an average increase of 49%, 28% and 54% comparing to the control (LSSCs without PNPs, giving J_{sc} = 135±12 μA/cm^2). Interestingly, the enhancement factor of AuNS@TiO_2 PNP is clearly lower than those of the other two PNPs (AgNS@TiO_2 and AgNP@TiO_2) which are comparable to one other.

The IPCE measurements were also performed and plotted in Figure 4.8B. All LSSCs showed substantially enhanced IPCE over the whole spectrum. Due to the strong photon absorption and large photocurrent generated by LHCII trimers and TiO_2 at the wavelength below 550 nm, the SPR effects of the small amount of PNPs were obscured in this range. However, at the wavelength from 550 to 750 nm where the IPCE from bare TiO_2 was negligible, the PNP-incorporated LSSCs showed clearly higher IPCE than those with LHCII sensitizer alone. In this range, an IPCE peak centered at ~665 nm was observed, matching well with the Q band absorption of LHCII trimers. The values of the characteristic parameters (including standard deviation) from I-V and IPCE measurements were summarized in Appendix B-Table B.2.

To further understand the effects of PNPs, the percentage change of the IPCE (ΔIPCE%) was calculated based on the equation:

$$\Delta IPCE\% = [IPCE_{(LHCII\text{-}PNPs)} - IPCE_{(LHCII)}] \times 100\% \,/\, IPCE_{(LHCII)} \quad (4.1)$$

Interestingly, the ΔIPCE% spectra in Figure 4.8C shows that the maximum ΔIPCE% of all three PNPs-incorporated LSSCs locate at the Q band range, with the fine features very similar to the Q_x and Q_y absorption bands of LHCII trimers. This evidence confirms that the photocurrent enhancement is ascribed to the coupling between the PNPs and LHCII trimers.

It is clear that the photocurrent under 1 sun full spectrum was significantly enhanced by all PNPs. However, the IPCE curves (Figures 4.8B and C) do not directly reflect the shapes of the UV-vis absorption spectra (Figures 4.2A) except in the long wavelength range corresponding to Q band. One of the possible reasons is that the intensity of the monochromatized light was too low (only 0.20 - 0.78 mW/cm^2) in the setup for IPCE measurements and thus only generated very weak electric field by the plasmon which can be easily masked by the photocurrent from TiO_2. To overcome this issue, broader bandpass filters (with 50 nm band width) were used to select specific wavelength regions under 1 sun illumination, allowing much higher light irradiance (at the level of ~18 mW/cm^2) at the solar cells. Indeed, much higher enhancements in J_{SC} were observed.

Figures 4.8D to F show the synchronous responses of J_{SC} to the illumination in selected wavelengths. Three bandpass interference filters were applied to chop the illumination into three specific ranges, 450±25 nm (Soret band of Chls), 675±25 nm (Q band of Chls), and 575±25 nm (region of minimum absorption). All photocurrents were highly reproducible as the illumination was turned on and off for four cycles, indicating that LHCII complexes were stable under the experimental conditions. The photocurrent of the LSSCs increases after incorporating all three types of PNPs, which is in contrast to the quenching of fluorescence emission by PNPs in the LHCII-PNP hybrids shown in Figures 4.3. These results collectively confirm that PNPs are able to enhance the charge transfer from the adsorbed LHCII to TiO_2 as illustrated in Figure 4.4. Considering that the absorption by LHCII is stronger around Soret band, substantial energy must be effectively transferred from Soret band to Q band to induce charge transfer and generate the photocurrent in LSSCs. This provides supplementary information to the previous spectroscopic studies regarding the energy transfer and charge separation in this hybrid system.

In summary, the optical spectroscopy results demonstrate that the SPR of the PNPs provides additional photon capture in the LHCII-PNP hybrid system (refer to the discussion of Figure 4.2). The captured energy in the form of plasmon may be utilized in the LSSCs to generate enhanced photocurrent by two mechanisms, i.e. (1) inducing additional LHCII excitation due to PIRET and (2) generating hot electron injection from metal core to TiO_2, similar to the models proposed by Cushing et al[109-110] The enhanced charge separation is reflected in the higher photocurrent of LSSCs in I-V and IPCE measurements. The AgNS@TiO_2 PNP is expected to present higher photocurrent enhancement than AuNS@TiO_2 PNP due to the larger spectral overlap with LHCII Soret band (around ~400 to 500 nm). However, it is interesting to note that the AgNP@TiO_2 PNP presents enhanced photocurrents comparable to AgNS@TiO_2 PNP and clearly higher than AuNS@TiO_2 PNP under the full solar spectral illumination and three selected wavelength bands, including 575±25 nm band that is overlapped with the SPR peak of AuNS@TiO_2 PNP. Particularly, the peak absorbance of AgNP@TiO_2 PNP in Figure 4.2B is 5.4 and 8.0 fold lower than spherical AgNP@TiO_2 and AuNP@TiO_2 PNPs, respectively.

By correlating the results from optical and photovoltaic studies, it is likely that following four factors collectively account for the relatively high plasmon effects of AgNP@TiO_2 PNP in LSSCs: (1) The absorption spectra in Figure 4.2B were collected from the PNP solution with the same particle surface area while the LSSCs used PNPs with the same mass, a factor of ~1.54 needs to be applied to the AgNP@TiO_2 curve to compare it with AgNS@TiO_2 PNPs. (2) The spectral overlap of AgNP@TiO_2 with LHCII is at the region of Q bands (~640 – 690 nm) which is directly involved in electron transfer from LHCII to TiO_2 and could be more effective. (3) The AgNP@TiO_2 PNPs likely rest flat on top of the LHCIIs sensitized on the TiO_2 photoanode due to their plate-like geometry. This can produce much larger contact area with the LHCII in the LSSC

than spherical PNPs (as illustrated in Figure 4.7) and thus can generate larger plasmonic effects by each PNP. (4) The photocurrent reflects the efficiency to convert incident photons (instead of irradiance) into free electrons. As shown in Appendix B-Figure B.9, after converting the AM1.5G standard solar spectrum from W/(m^2·nm) into number of photons/(s·m^2·nm), the incident photons at longer wavelength is significantly higher. Thus AgNP@TiO_2 PNP, whose SPR is at longer wavelength, may generate more effective plasmon than the other two PNPs though its overall absorbance is lower.

In addition, we speculate that the "hot electrons" in the plasmon-excited metal core may be also involved in the photovoltaic process as shown in Figure 4.4. Based on literature reports,[115-117] the hot electrons from the metal core are able to cross over the Schottky Barrier at the metal/TiO_2 interface (~0.9 eV for Au/TiO_2,[118] and ~0.2 eV for Ag/TiO_2[119]) under visible irradiation. In another study, we have confirmed that the photoconductivity of TiO_2 can be improved by the increased charge carrier density induced by the hot electron injection. This would lead to more efficient charge collection and faster electron transport in TiO_2.

4.4 Conclusions

Three types of TiO_2-coated PNPs with distinct surface plasmon resonace characteristics have been prepared. Incorporating these PNPs to form LHCII-PNP hybrids clearly provided additional plasmonic photon capture which is in good correlation with their SPR characteristics. However the fluorescence emission of LHCII was quenched in the LHCII-PNP hybrids, indicating the enhanced charge transfer from Q band of LHCII to CB of TiO_2. Femtosecond transient absorption studies unequivocally proved occurrence of the electron injection process. This is also supported by the observation of enhanced photocurrent in LHCII-sensitized solar cells after incorporating a small amount of PNPs. Despite the distinct SPR characteristics, all three types of

PNPs showed substantial enhancement in the photocurrent under the full solar spectral illumination and in IPCE, which are complementary with the emission quenching revealed by steady-state fluorescence measurements and faster decay observed with time-resolved fluorescence spectroscopy. Hot electrons from the metal cores of the PNPs might transfer to TiO_2 and improve charge collection efficiency of the devices. This strategy provides a new platform to reveal the nature of energy/charge transfer processes at the interface of natural photosynthetic protein complexes (such as LHCs, RCs, PSs, etc.) and artificial photovoltaic materials, which may lead to high-efficient bio-energy conversion devices.

Chapter 5 - Correlation of the Plasmon-Enhanced Photoconductance and Photovoltaic Properties of Core-Shell Au@TiO_2 Network

5.1 Introduction

Recent studies proposed that the metal/TiO_2 interface in the TiO_2-encapsulated metal NPs, i.e. metal@TiO_2, form an interfacial energy barrier (so-called Schottky barrier) to prevent electron flow across, but hot electrons from plasmon-excited metal cores could easily overcome this energy barrier and be injected into the TiO_2 conduction band (CB), resulting in a new mechanism for plasmon enhancement to DSSCs.[120] In general, the injected hot electrons are considered to be either being converted into photocurrent or functioning as charge carriers in the semiconductor matrix.[121] The photocurrent generated by direct hot electron transfer across the Schottky barrier has been collected and utilized for photodetection and photovoltaics based on well-designed devices with a complete circuit allowing refilling electrons back to the metal.[122-125] However, for the metal@TiO_2 NPs embedded in the mesoporous TiO_2 film in DSSCs, the sustainability of the photocurrent generation from hot electron injection is under debate considering that the metal core is unaccessible to the electron donors or the external circuit, which are needed for charge regeneration. On the other hand, the initially injected hot electrons may be converted into steady-state charge carriers and sufficiently raise the conductivity of the mesoporous TiO_2 frame, as has been indirectly demonstrated by enhanced photoconductivity in metal coupled semiconductors.[126-127] In addition, a recent study by Cushing et al. reported that metal@TiO_2 and metal@SiO_2@TiO_2 NPs can also enhance DSSCs by exciting surrounding TiO_2 matrix and dye molecules with near-field based plasmon-induced resonance energy transfer (PIRET) beside hot electron injection.[109]

In Chapter 4, we have also confirmed such effects in DSSCs senstized with natural light havesting complex II.[128] In most DSSC operations, these three effects are mixed. It is necessary to design some model systems to elucidate the contributions of these distinct effects in order to understand the complex mechanisms of plasmon-enhanced DSSCs.

Here, we propose a strategy to sort out the contributions of hot electron injection by comparing the characteristics of two model devices, i.e. micro-gap electrodes and DSSCs. A core-shell material consisting of isolated Au NPs embedded at the nodes of a nanostructured TiO_2 network, i.e. Au@TiO_2 network, was used as the bridging material in the micro-gap between two Au electrodes and as the mesoporous film on a DSSC anode, respectively. This study allows isolating the plasmonic effects on electron transport across the network structure[129] and link it with the enhanced photocurrents in DSSCs. These two devices present distinct wavelength dependences, revealing their different dominant plasmonic mechanisms. The correlation of the plasmonic enhanced photoconductance and photovoltaic properties unambiguously reveals the major role of hot electrons in the enhanced DSSCs

5.2 Experimental Section

5.2.1 Synthesis of Au@TiO_2 Network

The procedures to prepare the Au@TiO_2 network and the bare TiO_2 network as control were descibed in Chapter 2.5.

5.2.2 Materials Characterization

The morphology of the as-prepared Au@TiO_2 network was imaged with a transmission electron microscopy (TEM) with tungsten filament under 100 kV accelerating voltage (CM-100, FEI, OR). Scanning electron microscopy (SEM) images were taken with a field-emission system (Nano430, FEI, OR). Raman spectra were measured with a DXR Raman microscopy (Thermo

Electron, WI) using 50× objective, and 532 nm laser with 5 mW laser power. Absorption spectra were recorded using a Beckman DU640 UV-Vis system.

5.2.3 Photoconductance Measurements with A Micro-Gap Electrode

The micro-gap electronde was prepared with a lift-off lithography process by ion beam sputtering a 2 nm Cr adhesion layer and 100 nm thick gold film on patterned SiO_2/Si wafer. The as-prepared Au@TiO_2 network was drop-casted on a 2 μm wide gap between the two Au electrodes to bridge the circuit, and then annealed at 350 ℃ in the air for one hour. Photoconductance tests were carried our by measuring current versus bias voltage (I-V) curves with a CHI 440A potentiostat (CH Instruments, Austin, TX) under one-sun (100 mW/cm^2) irradiation using 300 W Xe lamp solar simulator with an AM 1.5G filter (Newport, Irvine, CA). The wavelength-dependent photocurrent was measured under 0.2 V bias and illumination of light at various wavelength selected with a monochromator coupled with a 75 W Xe lamp (74004, Oriel Instrument, Newport, Irvine, CA).

5.2.4 Photovoltaic Measurements of DSSCs Consisting of Au@TiO_2 Network

The Au@TiO_2 network paste was prepared by adding Au@TiO_2 ethanolic dispersion to α-terpineol with 10 wt% of ethyl cellulose. The mixture was homogenized in an ultrasonic bath for ~0.5 hour. A viscous paste was obtained by evaporation of extra solvent in a vacuum oven. For anode preparation, a fluorine-doped tin oxide (FTO) glass (TEC8, Dyesol, Queanbeyan NSW, Australia) was pretreated with 40 mM aqueous solution of $TiCl_4$ at 75 ℃ for 20 minutes and baked at 500 ℃ for 30 minutes to generate a thin TiO_2 barrier layer. Au@TiO_2 network film (~3 μm thick) coated on this substrate was conducted by conventional doctor blade method. The film was relaxed at 60 ℃ for 2 hours and then annealed at 500 ℃ in the air for 30 minutes, followed by sensitization with di-tetrabutylammonium cis-bis(isothiocyanato)bis(2,2'-bipyridyl-4,4'-

dicarboxylato)ruthenium(II) (N719, Dyesol, Queanbeyan, Australia) after cooling below 80℃. A 20 nm thick Pt film sputtered on FTO glass by a high resolution ion beam coater (model no. 681, Gatan Inc., Pleasanton, CA) was applied as the cathode. The anode and cathode were assembled with a 60 μm-thick heat treated Surlyn gasket (Solaronix, Aubonne, Switzerland). Then the iodolyte AN-50 electrolyte (Solaronix, Aubonne, Switzerland) filled the cell by a syringe through two holes punched on cathode. The assembled cell has an active area of 1 cm^2. The cell performance was evaluated with the characteristics of photocurrent−voltage (I−V) curve, the impedance measurement, and the incident photon-to-current efficiency (IPCE) tested under the short circuit condition with the same equipment setup for the photoconductivity measurement on micro-gap electrodes.

5.3 Results and Discussion

5.3.1 Structure and Absorption of the Core-Shell Au@TiO_2 Network

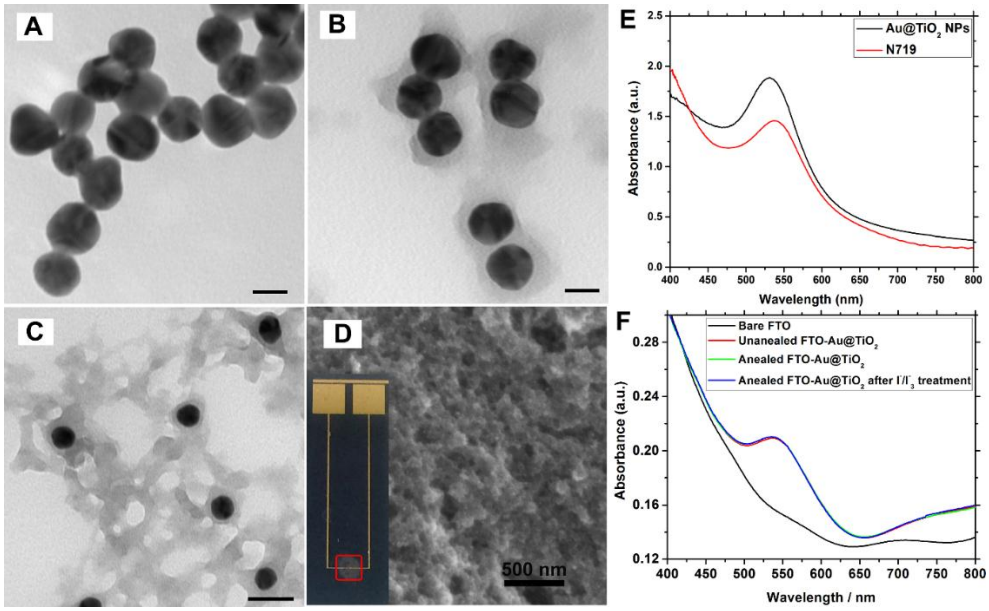

Figure 5.1 Structure and plasmonic absorption of the Au@TiO_2 network.

TEM images of (A) bare gold nanoparticles, (B) Au@TiO_2 core-shell nanoparticles (C) Au@TiO_2 network. (D) SEM image of Au@TiO_2 network deposited on micro-gap electrode after annealing. Inset: the photograph of micro-gap electrode with Au@TiO_2 network material drop casted in the region of red box to cover the micro-gap. Scale bars are 20 nm

in TEM images (A) and (B), 40 nm in (C), and 500 nm for SEM image (D). (E) Absorption spectra of Au@TiO_2 NPs in solution and 50 mM N719 in acetonitrile. (F) Absorption spectra of a thin film of Au@TiO_2 NPs on FTO glass subjected to annealing and I^-/I_3^- electrolyte treatment.

Synthesis of Au@TiO_2 network was defined into two steps. In the first step, a TiO_2 layer of ~8 nm was deposited on the surface of 20 nm Au NPs (Figure 5.1B). The growth of TiO_2 shell is a heterogeneous nucleation process that competes with formation of isolated TiO_2 NPs via homogeneous nucleation. This nucleation mechanism highly depends on the concentration of TiO_2 oligomers in solution.[130] In order to attain a uniform TiO_2 shell, an anhydrous condition with controlled relative humidity during reaction as well as comparatively low concentration of TTIP precursor are required to slow down the hydrolysis rate of TTIP and limit the amount of free TiO_2 oligomers in solution, restraining the unwanted homogeneous nucleation at this step. In the second step, the homogeneous reaction among TiO_2 oligomers was dominated by adding more precursors, and the core-shell Au@TiO_2 NPs formed by the first step were crosslinked into the amorphous TiO_2 network as shown in Figure 5.1C. The SEM image in Figure 5.1D confirmed that the network structure retained in the sample after drop-casting and annealing on the micro-gap electrode (illustrated in the inset of Figure 5.1D). The SPR peak wavelength is ~534 nm, slightly lower than the 539 nm peak wavelength of N710 absorption band, but the plasmonic band of Au@TiO_2 NPs overlaps with the whole absorption peak of N719 dye (Figure 5.1E), which is ideal for near-field plasmonic enhancement. The SPR peak doesn't show any obvious shift after growing into the Au@TiO_2 network (data not shown). In order to confirm that the TiO_2 shell fully covers the Au NPs, the Au@TiO_2 network was coated on a transparent FTO glass and annealed at 350 ℃ in the air for one hour. The prepared sample was then immersed in iodide/triiodide (I^-/I_3^-) electrolyte overnight. The absorption spectra after annealing and electrolyte treatment display negligible difference comparing with the initial spectrum (see Figure 5.1F), demonstrating that the intact

TiO_2 shell on the Au NPs is able to protect Au NPs from heat damage and iodide corrosion during the device fabrication and testing.

5.3.2 Photoconductance Study on the Micro-Gap Electrode

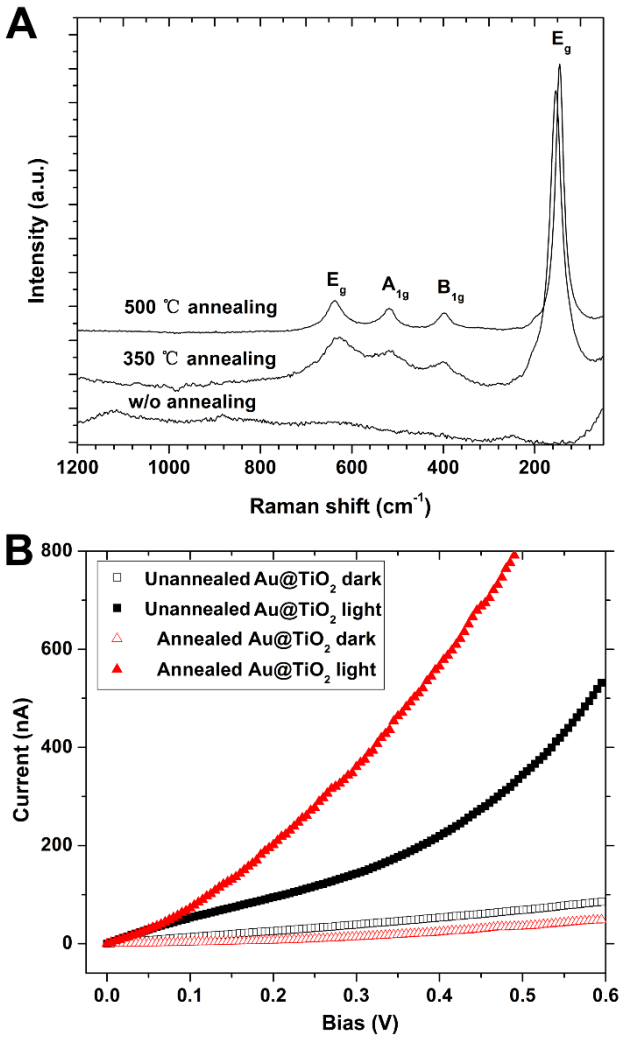

Figure 5.2 The effect of thermal annealing on the photoconductance of the Au@TiO_2 network.

(A) Raman spectra of Au@TiO_2 network on the micro-gap electrode without annealing and after annealing at 350 ℃ and 500 ℃, respectively. (B) I-V curves of the un-annealed and 350 ℃ annealed Au@TiO_2 network on the micro-gap electrodes under dark condition (open symbols) and under illumination (solid symbols).

The crystallization of the TiO_2 network under different temperature was characterized with Raman spectroscopy (Figure 5.2A). No clear peak is shown in the Raman spectrum of the initial sample before the thermal treatment, indicating the formation of an amorphous TiO_2. After

annealing at 350 ℃, the characteristic bands of anatase phase at ~143, 197, 396, 516, 639 cm^{-1} appeared. The peak intensity increased and the peak width narrowed down after subjecting to 500 ℃ annealing, demonstrating conversion into a higher degree of crystallinity. Previous studies reported that phase transition from anatase to rutile will occur if annealing at the temperature above 550 ℃.[131] However, rutile TiO_2 usually displays less photoactivity and slower charge transport rate than anatase TiO_2 due to the higher optical transition energy and worse interparticle connectivity.[76, 132-133] Thus it needs to be avoided. Note the micro-gap electrode shows unreliable readings after baking above 400 ℃ in the air, likely due to delamination of TiO_2 or Au films. Hence, in this study, the samples casted on the micro-gap electrode were annealed at 350 ℃ to attain single anatase phase and perform reliable photoconductivity measurements.

To investigate the photoconductance, the I-V curves of the Au@TiO_2 network casted on the micro-gap electrode were recorded under dark and illuminated conditions. The annealed Au@TiO_2 network exhibited bigger increase in photoconductance as represented by the larger slope in the I-V curve under illumination in Figure 5.2B, which can be ascribed to the improved anatase crystallinity of TiO_2. In contrast, slightly smaller current was measured with the annealed sample under the dark condition. This could be due to the possibility of lower density of oxygen vacancies in TiO_2 (as electron donors) after the thermal treatment.[134-135]

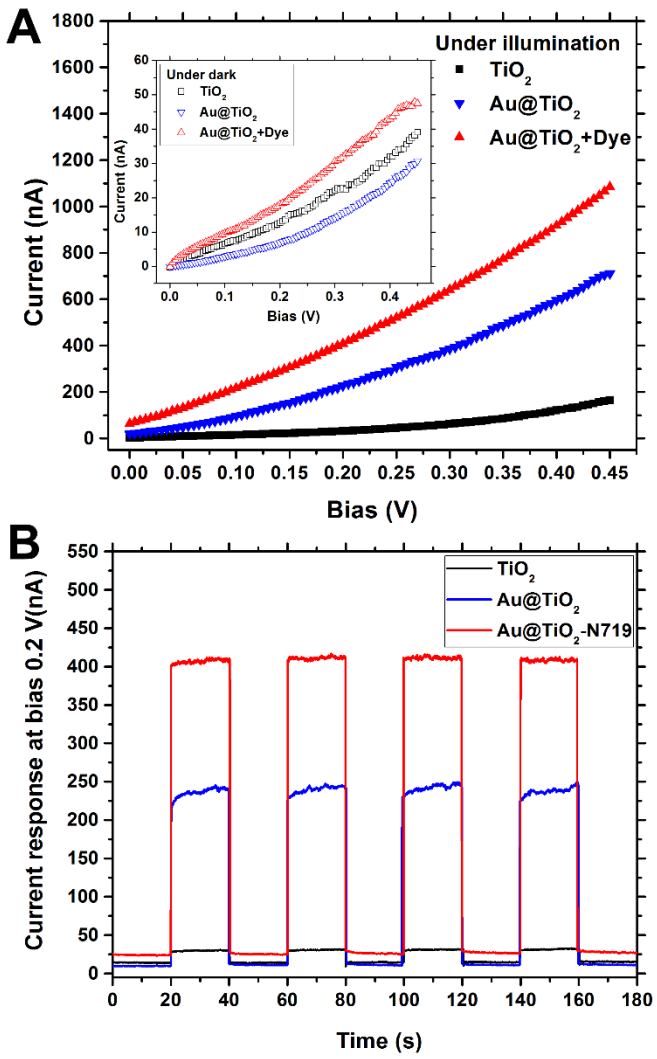

Figure 5.3 I-V curves and current responses measured on the Au@TiO_2 network compared to the bare TiO_2 network and the sample with N719 sensitization.

(A) I-V curves measured with the micro-gap electrodes deposited with a bare TiO_2 network (black solid square), bare Au@TiO_2 network (blue solid down triangle), and Au@TiO_2 network sensitized with N719 (red solid up triangle) under 1 sun illumination. Inset is the I-V curves of the corresponding samples under the dark condition. (B) Current responses at 0.2 V bias as the one-sun illumination is switched on and off, respectively. All samples were annealed at 350 ℃ before dye sensitization and measurements.

As illustrated in Figure 5.3A, under 1 sun illumination, the slope of the I-V curve measured with the Au@TiO_2 network is much larger than that of the bare TiO_2 network, which is further raised after N719 dye sensitization. Figure 5.3B shows synchronous responses of the photocurrent at 0.2 V bias to one sun illumination. All photocurrents were highly reproducible as the

illumination was turned on and off for four cycles. The response is very fast, beyond the temporal resolution of the instrument (~40 ms) that is mainly defined by the shutter speed, and the magnitudes correlate well with the trend of the I-V curves in Figure 5.3A. These results concluded that the photoconductivity of Au@TiO_2 network was enhanced (by 6.7 folds) due to the incorporation of Au NPs, and it was further improved with dye sensitization (by additional 5.5 folds).

Both Au NPs and N719 dye help to harvest the solar photons in the visible range while the TiO_2 alone only absorbs UV light. The strong plasmonic excitation of Au NPs would generate significant amount of hot electrons which can overcome the ~0.9 eV Schottky barrier to transfer from Au NPs into TiO_2 shell. The injected hot electrons act as charge carriers and thus increase the photoconductivity of the TiO_2 network. With additional N719 dye sensitization, because the energy level of the lowest un-occupied molecular orbital (LUMO) of N719 (-3.85 eV) locates 0.55 eV higher than the edge of the conduction band (CB) of TiO_2 (-4.4 eV), the excited electrons can easily transfer from the dye to the TiO_2 network. This process could be enhanced by the energy transfer from plasmonic Au NPs to N719 dye passing through the thin TiO_2 shell, i.e. the near-field associated PIRET, since the plasmonic band of the incorporated Au NPs matches well with the absorption band of N719 (as shown in Figure 5.1E). This would further raise the charge carrier density in the TiO_2 network and thus make it even more conductive. Notably, the lack of spectral overlap of the Au NPs with the TiO_2 disables the PIRET between Au NPs and TiO_2 shell. Therefore, the enhanced photoconductivity of the non-sensitized Au@TiO_2 network must be dominated by hot electron injection. More convincing evidence will be discussed in later sections.

The currents at the similar voltage bias under dark conditions from the corresponding samples (shown in the inset of Figure 5.3A) were about 20 times smaller than those obtained under

1 sun illumination, indicating a poor intrinsic conductivity of the TiO_2 network. It is noted that the Au@TiO_2 network shows slightly smaller dark current than the pure TiO_2 network. This may be due to the larger electron scattering by Au NPs and blocking of the carrier pathway by redistributed electron density at the Au/TiO_2 interface during Schottky barrier formation.[136] However, higher current in the dark condition was measured after dye sensitization, in contrast to the previous studies on single TiO_2-coated carbon nanofibers.[135] Since the measurements were carried out in atmosphere, oxygen molecules as electron scavengers may "quench" the conduction electrons.[137] Dye molecules adsorbed on TiO_2 might suppress this carrier "quenching" via blocking the oxygen adsorption and thereby improve the intrinsic conductivity of the TiO_2 network.

5.3.3 Photovoltaic Properties of Corresponding DSSCs

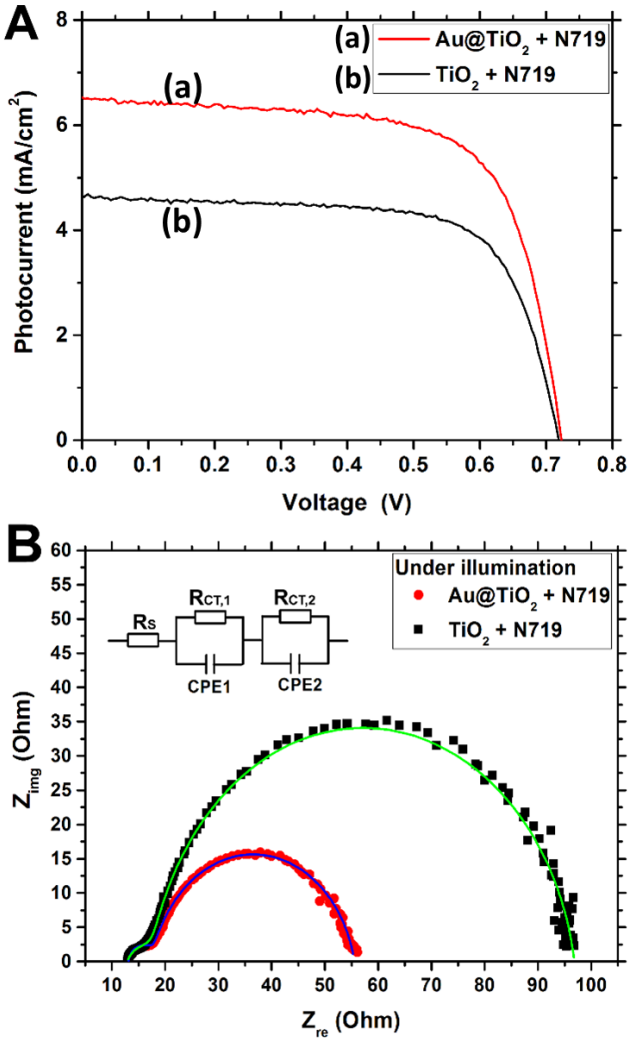

Figure 5.4 I-V and AC impedance measurements of the DSSCs consisting of pure TiO_2 network and Au@TiO_2 network, respectively.

(A) I-V curves and (B) AC impedance spectra of the DSSCs based on pure TiO_2 network (black curves) and Au@TiO_2 network (red curves), respectively. The impedance data are fitted with the equivalent circuit shown in the inset of panel B. All data were collected under one Sun irradiation.

The above discussed Au@TiO_2 network was prepared into a ~3 μm thick film on FTO-coated glass and used as an anode material in the DSSC for the purpose of correlating the enhanced photoconductivity with its photovoltaic performance. A pure TiO_2 network without Au NPs was used as the control. The I-V curves and AC impedance spectra measured from these two types of DSSCs are plotted in Figures 5.4A and 5.4B. Obviously, much larger photocurrents were generated

in the DSSC based on the Au@TiO_2 network, which is mainly attributed to the aforementioned plasmonic near-field stimulated dye excitation, i.e. PIRET. The short-circuit current (J_{SC}) was increased to 6.54 mA/cm^2 with Au@TiO_2 network comparing to 4.64 mA/cm^2 with the pure TiO_2 network. The open circuit voltage (V_{OC}) was nearly the same for both DSSCs, implying that the core-shell structure was effective in suppressing the electron-hole recombination in the Au NPs. However, another effect that was neglected in most literature is also significant. The series resistance calculated from the inverse of the slope of the I-V curve around V_{oc} was found to be reduced from 15 Ohm to 11 Ohm with the presence of Au NPs. In addition, the AC impedance spectra under illumination exhibited much smaller charge transfer resistance after incorporating Au NPs, giving a $R_{CT,2}$ value of 38 Ohm vs. 79 Ohm, as reflected by the smaller semicircle at the low frequency range in the DSSC made of the Au@TiO_2 network. These data correlate well with the higher photoconductivity shown in Figure 5.3, which conclusively prove that higher charge carrier density and thus higher conductance is generated in the Au@TiO_2 network.

5.3.4 Possible Mechanisms of the Photoconductance and Photovoltaic Enhancements

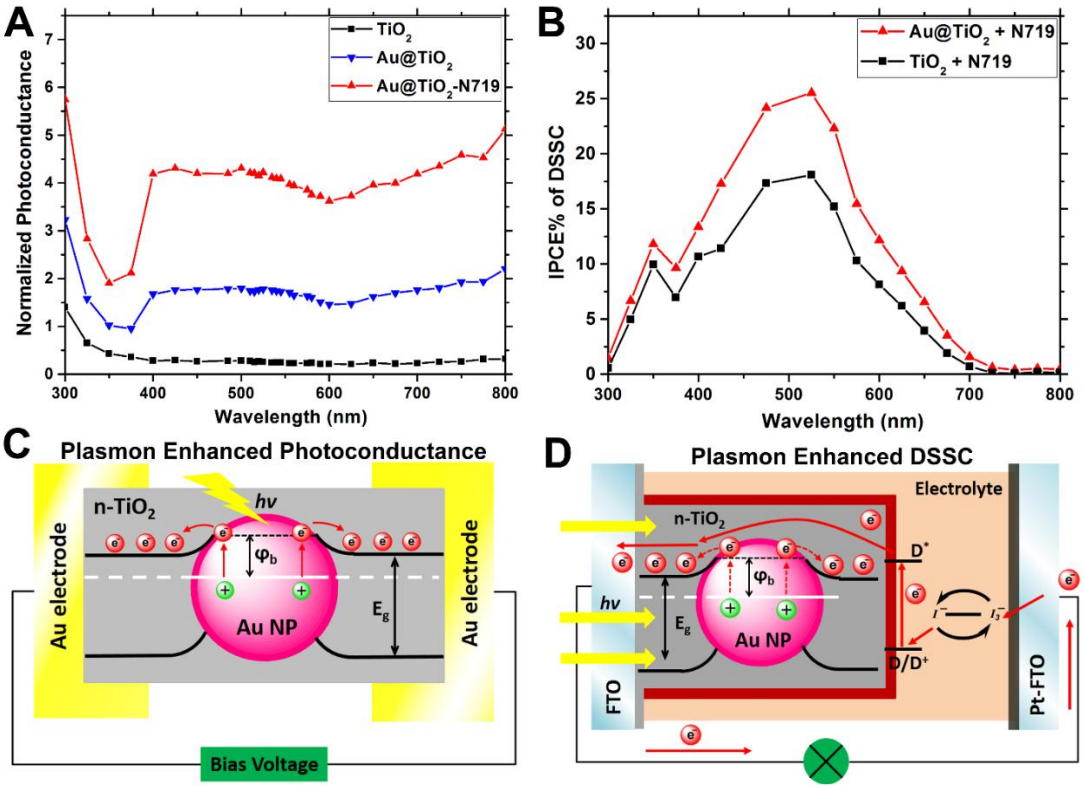

Figure 5.5 Wavelength dependence of photoconductance and IPCE studies and the schematics of the possible enhancement mechanisms.

(A) The wavelength dependent photoconductance measured under 0.2 V bias on the micro-gap electrode after normalized to the number of incident photons. (B) The incident photon-to-current efficiency (IPCE%) of the DSSCs based on the pure TiO_2 network and Au@TiO_2 network, respectively. (C, D) The schematic of the potential mechanisms of the plasmonic effects in the Au@TiO_2 network on the micro-gap electrode and in the DSSC, respectively.

In order to probe the origins of the enhanced charge carrier density in the Au@TiO_2 network, wavelength dependence of the photoconductance under 0.2 V bias voltage on the micro-gap electrode was compared with the IPCE measurement of corresponding DSSCs under short circuit. The IPCE was calculated with the equation:

$$\text{IPCE\%} = 100\% \times (1240 \times J_{SC}) / (\lambda \times P_{in}) \qquad (5.1)$$

where J_{SC} is the short circuit current and P_{in} is the powder of incident photons at each wavelength. For direct comparison, the photoconductance was normalized to the number of incident photons

of different wavelength using same equation of IPCE%, but replacing J_{SC} with the current measured under 0.2 V bias voltage. Here the contribution of dark current is ignored, since it is more than 100 times smaller than the current under illumination. The trend of the normalized photoconductance at all wavelengths in Figure 5.5A correlates well with the illuminated I-V curves in Figure 5.3A, implying the large enhancement to the photoconductance by Au NPs embedded in the TiO_2 network. Interestingly, the enhancement appeared in a much broader range than the Au NP's SPR band, covering the full visible range from 400 to 800 nm (with the cutoff below 400 nm defined by light absorption by the glass substrate). The enhanced current (by a factor of ~6) is almost constant over this wavelength range except a small dip around 600 nm. The photocurrent is further increased by another factor of ~10 after N719 dye sensitization, indicating the strong coupling between N719 dye and the plasmonic Au NPs. It is noted that the wavelength-dependent photoconductance in Figure 5.5A (illuminated from above) shows a dip at ~375 nm in the curves with Au NPs due to the convolution of the sharp decline of the plasmonic absorption of Au NPs and quick increase of TiO_2 absorption when the wavelength goes below 400 nm.

In contrast, the IPCE curve of the DSSC made of the pure TiO_2 network shows a well-defined single peak in the visible range, whose peak wavelength and shape reflect the absorption spectrum of N719 dye. The IPCE value below 400 nm wavelength approximately monotonically decreases with the wavelength since the illumination is applied from the back side and the photons at shorter wavelength is absorbed by the glass substrate and FTO coating, as we demonstrated in an earlier study.[78] After incorporating Au NPs, the shape of the IPCE peak remains the same but the peak IPCE value is increased by ~41%. Notably, the long flat tails at longer wavelengths (600 – 800 nm) in Figure 5.5A do not show in the IPCE curves of the corresponding DSSCs (Figure

5.5B), but they are of great interests toward utilization of lower energy photons. These two types of devices are clearly based on different mechanisms.

The potential mechanisms of the plasmonic enhancement in photoconductance and the photovoltaics are schematically depicted in Figures 5.5C and 5.5D. As discussed previously, a Schottky barrier formed at Au/TiO_2 interface would hinder the interfacial electron transfer in dark conditions. The barrier height is determined by the band structure of TiO_2 and the work function of gold, which is only ~0.9 eV (i.e. ~1378 nm in photon wavelength). As a result, not only the photons in the plasmonic band of the Au NPs but also those in the near-infrared range are energetic enough to generate hot electrons in the Au NPs that can be injected into the TiO_2 network. Thus the charge carrier density in the semiconductive TiO_2 network is increased. In other words, the injected hot electrons act as mobile charge carriers and able to deliver larger currents under the same bias voltage. This mechanism nicely explains the I-V characteristics of the micro-gap experiments and the equally effective photoconductance enhancement by photons in longer wavelength region. The charge carrier density likely reaches the saturation level even with the weak light absorbance of Au NPs at ~800 nm wavelength, thus forming a flat plateau.

The photovoltaic behavior of the DSSCs, however, is dominated by the charge separation at the dye/TiO_2 interface. The steady-state photocurrent requires electrons being continuously injected from the dye molecules into TiO_2 and the oxidized dye being quickly regenerated by reduction with I^-/I_3^- electrolyte. In the DSSC made of the Au@TiO_2 network, considering that the Au NPs embedded within the TiO_2 shell are not accessible by the regenerating agents, the plasmonic generated hot electrons from Au NPs to TiO_2 cannot be the source of continuous steady-state photocurrent. However, they are sufficient to raise the charge carrier density in TiO_2 and reduce the series resistance and charge transfer resistance in the corresponding DSSCs. This effect

amplifies the characteristic features of the DSSC's IPCE curves which are determined by the charge separation initiated by photon absorption spectrum of the dye molecules. The correlation of the photovoltaic and photoconductance measurements clearly reveals the two distinct effects of plasmonic NPs which are entangled in normal plasmonic DSSCs.

5.4 Conclusion

The core-shell Au@TiO_2 network deposited on the micro-gap electrode and photoanode of DSSCs exhibits enhancements in photoconductance and photovoltaic performance compared to the TiO_2 network without incorporating Au NPs. Ramen spectra confirmed that the TiO_2 network was crystalized into single anatase phase after thermal annealing and achieved higher photoconductivity due to faster electron transport in the crystalline phase than the amorphous TiO_2. Based on the correlation of the photoconductivity to the photovoltaic performance of the enhanced DSSC fabricated by the same Au@TiO_2 network, a plausible explanation was proposed to discriminate the contribution of the hot electron injection from the SPR enhancement. Hot electrons excited from the Au NPs are converted into major charge carriers in the TiO_2 network. The interfacial electron transfer across the Au/TiO_2 Schottky barrier (~0.9 eV) can be easily realized under illumination over the whole visible range allowing extending the enhancement effect to the light in the near-infrared region where the photon energies is distinctly below the semiconductor band gap, Au SPR, and dye absorption band. The study might inspire future optoelectronic devices with smart designs to make better use of hot electrons and the associated interfacial electron transfer for outstanding performance.

Chapter 6 - Conclusion and Future Outlooks

The goal of this dissertation was to tap into the fundamental energy/charge transfer properties of photosynthetic pigment-protein complexes, and develop plasmon-enhanced bio-energy conversion system through a proper approach to interface them with PNPs in artificial photovoltaic devices. This goal has been achieved through the combined work presented in Chapter 3, 4 and 5 using a model system based on natural extract LHCII as light antenna in DSSCs.

As part of this effort, Chapter 3 preliminarily verified the photovoltaic properties of LHCII in a thin layer sensitized TiO_2 solar cell. Photocurrent generation was enabled by the electron injection from excited LHCII to TiO_2 conduction band. The aggregation allowed reorganization between individual trimers, which dramatically increased the photocurrent, correlating well with the formation of Chl-Chl coupled charge-transfer states that are effectively coupled with the TiO_2 surface and thus facilitate the electron injection. The assembled LHCII sensitized solar cells demonstrated remarkable stability in both aqueous buffer and acetonitrile electrolytes over 30 days.

In Chapter 4, LHCII trimers were conjugated with three types of metal@TiO_2 core-shell PNPs to form LHCII-PNP hybrids. Enhanced photon harvesting capability and more efficient charge separation at the LHCII/TiO_2 interface were demonstrated in the hybrids, as revealed by PIRET process, quenching of the steady-state fluorescence emission, and reduction of the transient fluorescence lifetime. Femtosecond transient absorption technique provides further conclusive proof for charge injection from excited LHCII into the conduction band of TiO_2 shell of the PNPs. The plasmonic effect was also demonstrated by the enhanced photocurrent after incorporating the PNPs in the LHCII sensitized solar cells built on an open-structured three-dimensional

photoanode, i.e. vertically aligned TiO_2 nanotree arrays, and was consistently supported by the spectroscopic results.

Chapter 5 focuses on different plasmonic effects on the energy transfer and the charge separation in the synthesized Au@TiO_2 network. The enhancements in photoconductance and photovoltaic performance were achieved by the Au@TiO_2 network applied on the micro-gap electrode or the photoanode of DSSC, which can be ascribed to two aspects: 1) the promoted dye excitation by the near-field induced PIRET from Au NPs to dye molecules, 2) the increase of charge carrier density in the semiconductive TiO_2 network due to the hot electron injection across the Schottky barrier at Au/TiO_2 interface. The engagement of hot electrons excited from metal NPs allows extending the enhancement effect towards the near infrared region.

So far, poor stability and low conversion efficiency prevent the biophotovoltaic devices from scaled-up manufacturing and competing with conventional systems. Future prospects include novel biosolar cells based on more efficient and robust photosynthetic protein complexes and development of biocompatible noncorrosive electrolytes. In addition, as mentioned before, perovskite materials have attracted a lot of attentions due to their superior performance in photovoltaics. Another future plan is to fabricate perovskite solar cells based on the 3D TiO_2 nanotree photoanode. The preliminary data and prospective scenario are depicted below.

6.1 Water Soluble Chlorophyll-Binding Protein (WSCP) in DSSC

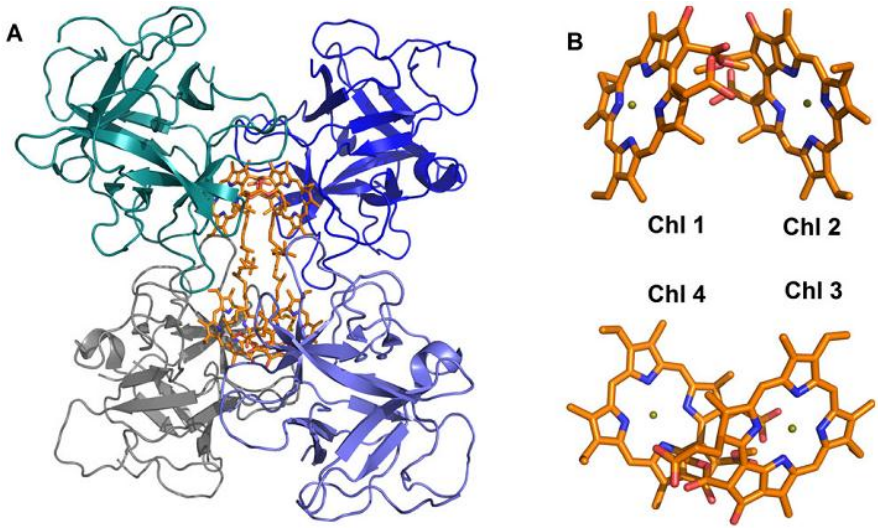

Figure 6.1 Overall structure of the tetrameric LvWSCP.

(A) The four monomers are shown in green, blue, purple and gray. The four Chls are shown in orange. (B) The geometry of two pairs of Chl dimers (i.e. Chl 1/2 and Chl 3/4). (Reprinted with permission from ref. 121 Copyright © 2016 The American Society of Photobiology)

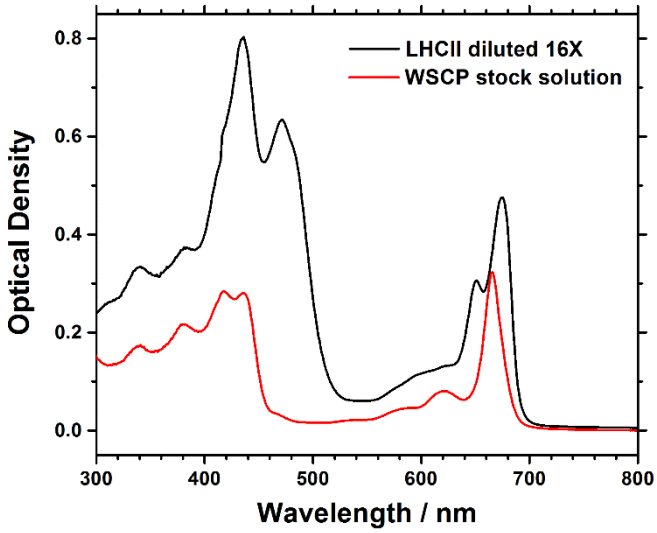

Figure 6.2 Absorption spectra of WSCP and LHCII in aqueous solution.

(from Y. Yang et al. unpublished work).

Figure 6.1 shows the molecular structure of water soluble chlorophyll-binding protein from *Lepidium virginicum* (LvWSCP) based on the 2 Å resolution crystal structure.[138] Compared to

LHCII, WSCP has simpler structure that only provides high affinity for Chl pigments. Each complex binds four Chls (i.e. two pairs of Chls dimers) in the hydrophobic cavity of its tetramer with hydrophilic ligands on the periphery that make it soluble in aqueous environment.[139] The absorption spectrum of WSCP in Figure 6.2 displays the characteristic Sorret and Q band absorptions of Chl *a* and Chl *b* similar to that of LHCII trimer. Since Chls are well protected and stabilized in the protein matrix, WSCP should be robust and appropriate for applications in bio-photovoltaic devices.

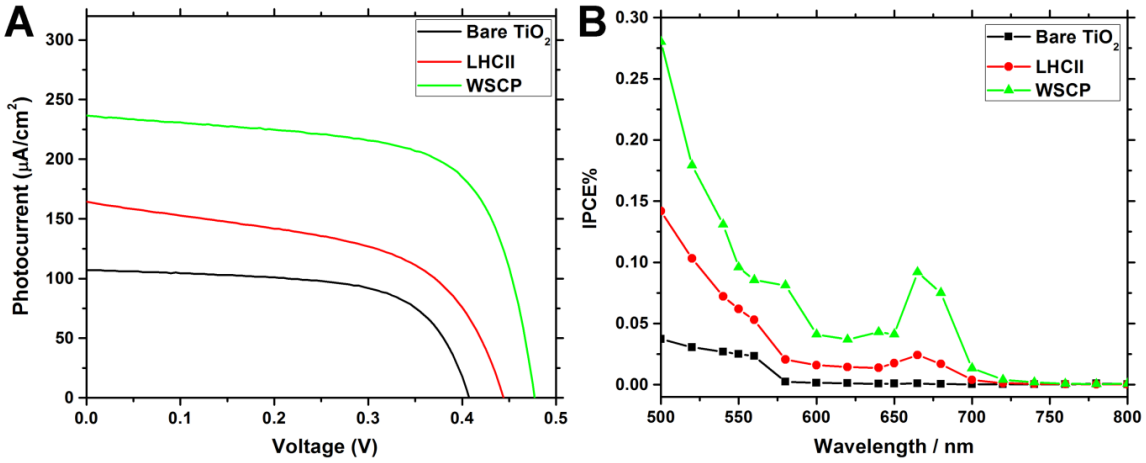

Figure 6.3 (A) IV curves and IPCE (B) IPCE spectra of the DSSCs based on WSCP, LHCII and the bare TiO_2.

(from Y. Yang et al. unpublished work)

WSCP (provided by our collaborator Dr. Ryszard Jankowiak) was applied to sensitize the TiO_2 nanotree anode as-prepared in Chapter 4, and assembled into the DSSC filled with iodolyte ionic liquid electrolyte (ADE-250, Solaronix, Switzerland). Based on the OD readings from Figure 6.2, the stocks concentration of WSCP in aqueous solution is much lower than the LHCII trimer stocks solution that used for TiO_2 sensitization in Chapter 4. However, both IV and IPCE tests in Figure 6.3 confirmed that the WSCP tetramers as light-harvesting antenna performed much better than the LHCII trimers in photocurrent generation of the corresponding sensitized solar cells.

6.2 Non-aqueous and Aqueous Cobalt$^{(II/III)}$ Complex Electrolyte

Even though iodide/triiodide (I^-/I_3^-) was the most common choice of redox mediator to construct highly efficient DSSCs, some drawbacks of this redox couple, such as corrosiveness to most metallic electrodes/nanoparticles and a significant energy loss arising from the large driving force required for dye regeneration, trigger the motivation of exploitation of new redox mediators.[140] $Co^{II/III}$ complexes have emerged as leading candidates to replace the I^-/I_3^- redox shuttle because of its compatibility with most metals, negligible visible light absorption, and tunable redox potential via tailored ligand designs to achieve efficient dye regeneration as well as maximum V_{OC}.[141] Cobalt$^{(II/III)}$ tris(2,2'-bipyridine) ($[Co(bpy)_3]^{2+/3+}$) based redox electrolyte has demonstrated outstanding performance in corporation with a synthesized porphyrin dye, which achieved a record efficiency of 12.8% and V_{OC} of 965 mV.[142] This type of electrolytes is expected to coordinate well with most photosynthetic pigment-protein complexes which contain the nature porphyrin dye, chlorophyll, as major pigment to harvest sunlight for photosynthesis reactions. Depending on the ligands, the $[Co(bpy)_3]^{2+/3+}$ redox couple can be applied in both non-aqueous (i.e. $[Co(bpy)_3]^{2+/3+}$ $(TFSI)_{2/3}$) and aqueous (i.e. $[Co(bpy)_3]^{2+/3+}$ $(NO_3)_{2/3}$) electrolytes as the structure shown in Figure 6.4.

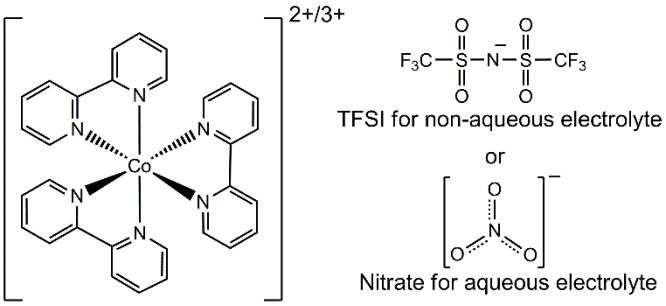

Figure 6.4 The molecule structures of non-aqueous and aqueous Tris(2,2'-bipyridine)cobalt$^{(II/III)}$ redox complexes.

6.2.1 Synthesis of $[Co(bpy)_3]^{2+/3+}$ $(TFSI)_{2/3}$ and $[Co(bpy)_3]^{2+/3+}$ $(NO_3)_{2/3}$

The $[Co(bpy)_3]^{2+/3+}$ TFSI for non-aqueous electrolyte was synthesized with the modified literature method.[143] Briefly, one equivalent of $CoCl_2 \cdot 6H_2O$ was dissolved in a minimum amount of methanol and added dropwise with 3.3 equivalents of 2,2'-bipyridine in methanol under stirring and 60℃ heating, followed by a reflux for 2 hrs. Then to the filtrate solution an excess of lithium bis(trifluoromethane-sulfonyl)imide (LiTFSI) was added, and the solution was again refluxed for 30 minutes and then cooling naturally to attain a crystalline brown yellow product. The product was filtered, washed several times with little amounts of diethyl ether-methanol mixed solution (1:1) and dried under vacuum at 60℃ overnight. The Co^{3+} complex was prepared by oxidization of the Co^{2+} complex, with 1.05 molar equivalent of methanolic bromine (NOBF4) added to acetonitrile solution of the as-prepared Co^{2+} complex. The solvent was removed by rotary evaporation. The solid was dissolved in acetonitrile again and added with 10 folds excess of LiTFSI to precipitate the product which was then filtered, washed with diethyl ether and water and dried under vacuum overnight.

The water soluble $[Co(bpy)_3]^{2+/3+}$ $(NO_3)_{2/3}$ was synthesized by the following method as reported before.[144] One equivalent of $Co(NO_3)_2 \cdot 6H_2O$ was dissolved in a minimum amount of deionized water and 3.3 equivalents of 2,2'-bipyridine dissolved in methanol were added dropwise. The solution was stirred at room temperature for 1 h and evaporated to remove the solvents. The product was rinsed with methanol and diethyl ether, and dried under vacuum for 24 h. Oxidation of the Co(II) complex was performed by adding a slight excess of $AgNO_3$ to an acetonitrile solution of the complex. After stirring at room temperature for 2 hours, the Ag particles were filtered and the solvent was removed by rotary evaporation. The product was washed with methanol and dried under vacuum overnight.

6.2.2 Performance of Non-Aqueous and Aqueous $[Co(bpy)_3]^{2+/3+}$ Electrolyte.

The non-aqueous electrolyte compositions were as follows: 0.20 M $[Co(bpy)_3](TFSI)_2$, 0.070 M $[Co(bpy)_3](TFSI)_3$, 1.0 M tert-butylpyridine (tBP), 0.05 M LiTFSI in acetonitrile.

The aqueous electrolyte is composed of 0.20 M $[Co(bpy)_3](NO_3)_2$, 0.040 M $[Co(bpy)_3](NO_3)_3$, 0.70 M N-Methylbenzimidazole (NMBI). The mixture was heated to 60 ℃ for 2 min to completely dissolve.

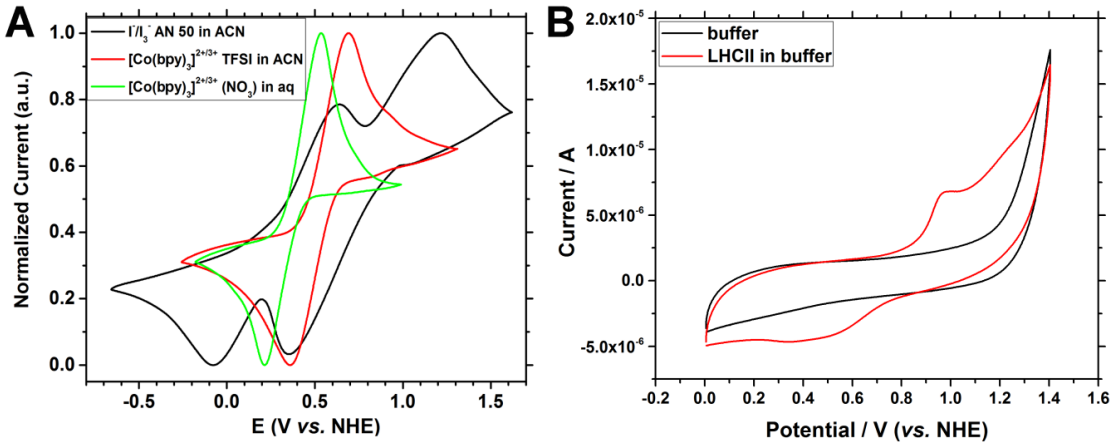

Figure 6.5 Cyclic voltammetry (CV) of the electrolytes and LHCII.

(A) CV of commercial I^-/I_3^- electrolyte (AN 50) diluted in acetonitrile (ACN) (black wave), non-aqueous $[Co(bpy)_3]^{2+/3+}$ TFSI electrolyte, and aqueous $[Co(bpy)_3]^{2+/3+}$ NO_3 electrolyte. The measurements were performed with use of Pt-sputtered FTO as working electrode, Pt foil as counter electrode, and Ag/AgCl as reference at a scan rate of 100 mV/s. (B) CV of LHCII in tricine buffer, measured with glassy carbon electrode as working electrode. The plots are relative to the normal hydrogen electrode (NHE). (from Y. Yang et al. unpublished work)

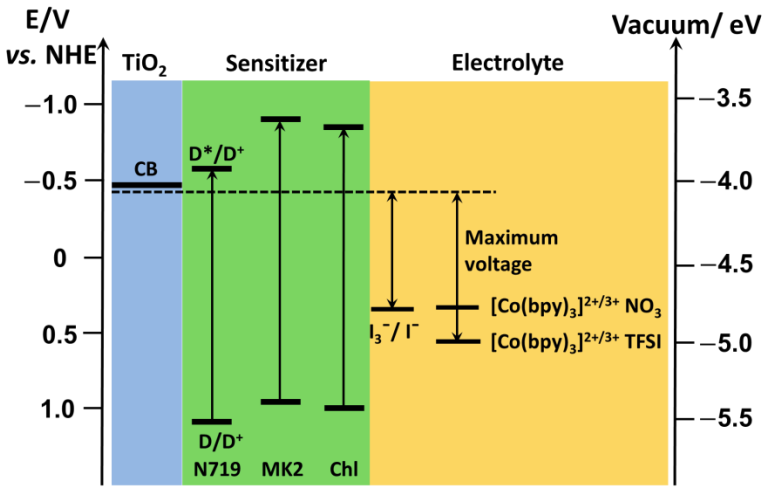

Figure 6.6 Energy level diagram of DSSC components.

The redox potentials of the electrolytes and the oxidation potential of the Chl pigment are based on the peak potentials of the CV (plotted in Figure 6.5). (from Y. Yang et al. unpublished work)

Figure 6.5A illustrates the electrochemical properties of the $[Co(bpy)_3]^{2+/3+}$ complexes investigated by cyclic voltammetry (CV). A quasi-reversible redox reaction is observed at half-wave redox potentials of $E_0 = +0.526$ V and $+0.374$ V vs. NHE for $[Co(bpy)_3]^{2+/3+}$ TFSI and $[Co(bpy)_3]^{2+/3+}$ NO_3, respectively. Compared with the two electron redox reaction of I^-/I_3^- electrolyte (black wave), $[Co(bpy)_3]^{2+/3+}$ complexes perform one electron redox reaction with narrower peak separation, indicating a faster reaction kinetics. The oxidation potential (referred to HOMO level) of Chl pigment was determined at $+0.970$ V vs. NHE by the CV of LHCII (Figure 6.5B). Figure 6.6 compares the redox potentials (vs. NHE) derived for I^-/I_3^-, two $[Co(bpy)_3]^{2+/3+}$ complexes, and the HOMO LUMO levels of sensitizers N719, MK2 and Chl. The oxidation potentials of the two cobalt complexes locate higher than HOMO levels of all three sensitizers, indicating the suitability of the redox couples for dye regeneration. The DSSC using $[Co(bpy)_3]^{2+/3+}$ TFSI might give larger V_{OC} resulting from 172 mV higher in redox potential than I^-/I_3^- ($E_{1/2} = +0.354$ V vs. NHE).

6.3 Pervoskite Solar Cells

The mixed halide perovskite $CH_3NH_3PbI_{3-x}Cl_x$ was synthesized according to the reported method.[24] Briefly, $PbCl_2$ and CH_3NH_3I was mixed with a molar ratio 1:3 and dissolved in DMF with the concentration of 0.73 M and 2.2 M, respectively. The mixture solution was stirred at 60 ℃ temperature overnight, and spin-coated on the pre-heated FTO coated glass at 2000 rpm for 30 second. The sample coated substrate was then annealed on a hot plate at 95 ℃ for 1.5 hours.

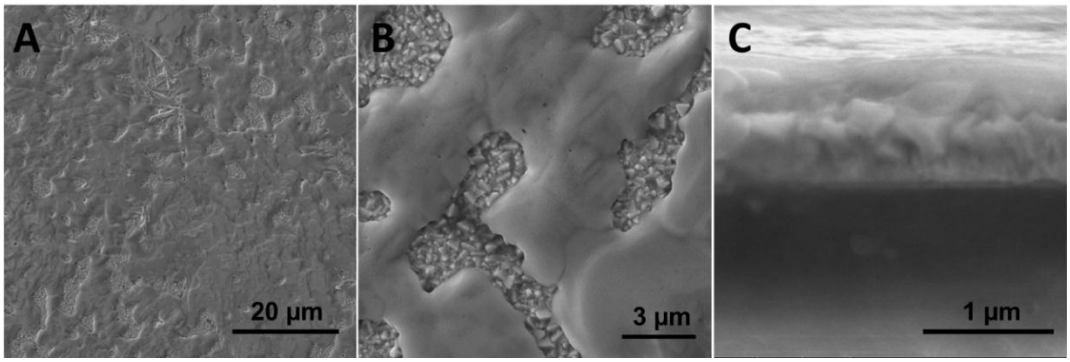

Figure 6.7 Morphology of the spin-coated perovskite film on FTO glass.
(A-C) SEM images of the top and the cross-sectional views. Panel B shows the voids in the film under higher magnification. (from Y. Yang et al. unpublished work)

Figure 6.7 shows SEM images of the top and the cross-sectional views of the perovskite layer deposited on FTO glass. The layer is about 300~500 nm thick, but not uniform with many voids exposing the uncovered FTO. For planar thin-film architecture, incomplete coverage of perovskite would lower the performance of the solar cells through current leaking from small shunt resistance paths and loss in light absorption.[145]

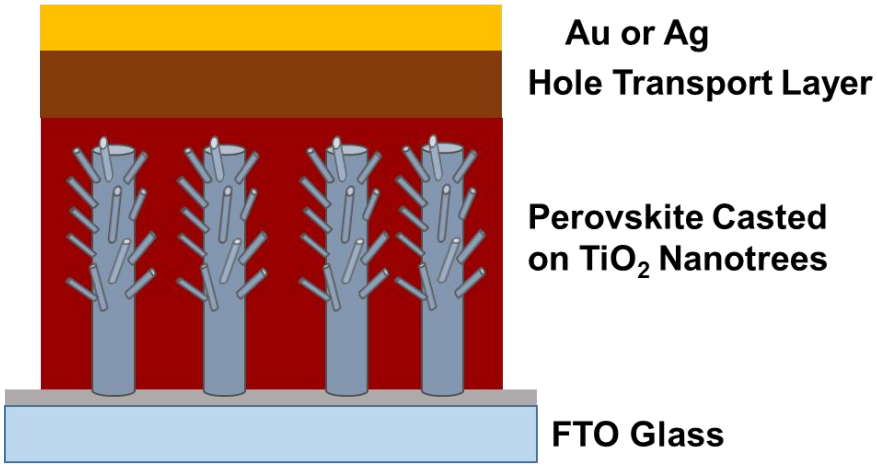

Figure 6.8 Schematic of the perovskite solar cell based on the 3D TiO_2 nanotree photoanode.

Based on previous studies, the pin-hole free perovskite "capping layer" can be prepared by drop-casting on the mesoporous Al_2O_3 or TiO_2 support film.[146-147] The support films were also confirmed to increase the V_{OC} and alleviate the hysteresis in I-V measurements.[146, 148] Hence, we consider to adopt the 3D TiO_2 nanotree array in future perovskite solar cell study. The schematic scenario is illustrated in Figure 6.8.

References

1. Various Authors, Energy Crisis. https://en.wikipedia.org/wiki/Energy_crisis

2. *Today in Energy*. U.S. Energy Information Administration: **7/2/2015**.

3. *Inventory of U.S. Greenhouse Gas Emissions and Sinks: 1990-2013*. U.S. Environmental Protection Agency: **2015**.

4. Ameri, T.; Li, N.; Brabec, C. J. Highly efficient organic tandem solar cells: a follow up review. *Energy Environ Sci* **2013,** *6*, 2390-2413.

5. *Energy and the challenge of sustainability*. Unitied Nations Development Programme and World Energy Council: **2000**.

6. Green, M. A.; Ho-Baillie, A.; Snaith, H. J. The emergence of perovskite solar cells. *Nat Photon* **2014,** *8*, 506-514.

7. Ragoussi, M.-E.; Torres, T. New generation solar cells: concepts, trends and perspectives. *Chem Commun* **2015,** *51*, 3957-3972.

8. Madsen, M. V. Solar cells-the three generations. http://plasticphotovoltaics.org/lc/lc-solarcells/lc-introduction.html.

9. O' Regan, B.; Grätzel, M. A Low-Cost, High-Efficiency Solar-Cell Based on Dye-Sensitized Colloidal TiO_2 Films. *Nature* **1991,** *353*, 737-740.

10. Ito, S.; Zakeeruddin, S. M.; Humphry-Baker, R.; Liska, P.; Charvet, R.; Comte, P.; Nazeeruddin, M. K.; Péchy, P.; Takata, M.; Miura, H. High-Efficiency Organic-Dye-Sensitized Solar Cells Controlled by Nanocrystalline-TiO2 Electrode Thickness. *Adv Mater* **2006,** *18*, 1202-1205.

11. Kuang, D.; Uchida, S.; Humphry-Baker, R.; Zakeeruddin, S. M.; Grätzel, M. Organic Dye-Sensitized Ionic Liquid Based Solar Cells: Remarkable Enhancement in Performance through Molecular Design of Indoline Sensitizers. *Angew Chem Int Ed* **2008,** *47*, 1923-1927.

12. Wu, Y.; Marszalek, M.; Zakeeruddin, S. M.; Zhang, Q.; Tian, H.; Grätzel, M.; Zhu, W. High-conversion-efficiency organic dye-sensitized solar cells: molecular engineering on D-A-π-A featured organic indoline dyes. *Energy Environ Sci* **2012,** *5*, 8261-8272.

13. Robel, I.; Subramanian, V.; Kuno, M.; Kamat, P. V. Quantum dot solar cells. Harvesting light energy with CdSe nanocrystals molecularly linked to mesoscopic TiO_2 films. *J Am Chem Soc* **2006,** *128*, 2385-2393.

14. Kamat, P. V. Quantum dot solar cells. Semiconductor nanocrystals as light harvesters. *J Phys Chem C* **2008,** *112*, 18737-18753.

15. Lee, Y. L.; Lo, Y. S. Highly Efficient Quantum-Dot-Sensitized Solar Cell Based on Co-Sensitization of CdS/CdSe. *Adv Funct Mater* **2009,** *19*, 604-609.

16. Nozik, A. J.; Beard, M. C.; Luther, J. M.; Law, M.; Ellingson, R. J.; Johnson, J. C. Semiconductor quantum dots and quantum dot arrays and applications of multiple exciton generation to third-generation photovoltaic solar cells. *Chem Rev* **2010,** *110*, 6873-6890.

17. Ma, W.; Yang, C.; Gong, X.; Lee, K.; Heeger, A. J. Thermally stable, efficient polymer solar cells with nanoscale control of the interpenetrating network morphology. *Adv Funct Mater* **2005,** *15*, 1617-1622.

18. Li, G.; Zhu, R.; Yang, Y. Polymer solar cells. *Nat Photon* **2012,** *6*, 153-161.

19. He, Z.; Zhong, C.; Su, S.; Xu, M.; Wu, H.; Cao, Y. Enhanced power-conversion efficiency in polymer solar cells using an inverted device structure. *Nat Photon* **2012,** *6*, 591-595.

20. Sargent, E. H. Colloidal quantum dot solar cells. *Nat Photon* **2012,** *6*, 133-135.

21. Kojima, A.; Teshima, K.; Shirai, Y.; Miyasaka, T. Organometal Halide Perovskites as Visible-Light Sensitizers for Photovoltaic Cells. *J Am Chem Soc* **2009,** *131*, 6050-6051.

22. Liu, M.; Johnston, M. B.; Snaith, H. J. Efficient planar heterojunction perovskite solar cells by vapour deposition. *Nature* **2013,** *501*, 395-398.

23. Lee, M. M.; Teuscher, J.; Miyasaka, T.; Murakami, T. N.; Snaith, H. J. Efficient Hybrid Solar Cells Based on Meso-Superstructured Organometal Halide Perovskites. *Science* **2012,** *338*, 643-647.

24. Zhou, H.; Chen, Q.; Li, G.; Luo, S.; Song, T.-b.; Duan, H.-S.; Hong, Z.; You, J.; Liu, Y.; Yang, Y. Interface engineering of highly efficient perovskite solar cells. *Science* **2014,** *345*, 542-546.

25. Chen, C.-W.; Hsiao, S.-Y.; Chen, C.-Y.; Kang, H.-W.; Huang, Z.-Y.; Lin, H.-W. Optical properties of organometal halide perovskite thin films and general device structure design rules for perovskite single and tandem solar cells. *J Mater Chem A* **2015,** *3*, 9152-9159.

26. Albrecht, S.; Saliba, M.; Baena, J. P. C.; Lang, F.; Kegelmann, L.; Mews, M.; Steier, L.; Abate, A.; Rappich, J.; Korte, L. Monolithic perovskite/silicon-heterojunction tandem solar cells processed at low temperature. *Energy Environ Sci* **2016,** *9*, 81-88.

27. Chen, Z. H.; Tang, Y. B.; Liu, C. P.; Leung, Y. H.; Yuan, G. D.; Chen, L. M.; Wang, Y. Q.; Bello, I.; Zapien, J. A.; Zhang, W. J.; Lee, C. S.; Lee, S. T. Vertically Aligned ZnO Nanorod Arrays Sentisized with Gold Nanoparticles for Schottky Barrier Photovoltaic Cells. *J Phys Chem C* **2009,** *113*, 13433-13437.

28. Rühle, S.; Shalom, M.; Zaban, A. Quantum-dot-sensitized solar cells. *ChemPhysChem* **2010,** *11*, 2290-2304.

29. Kim, H.-S.; Lee, C.-R.; Im, J.-H.; Lee, K.-B.; Moehl, T.; Marchioro, A.; Moon, S.-J.; Humphry-Baker, R.; Yum, J.-H.; Moser, J. E. Lead iodide perovskite sensitized all-solid-state submicron thin film mesoscopic solar cell with efficiency exceeding 9%. *Sci Rep* **2012,** *2*.

30. Kim, H.-S.; Lee, J.-W.; Yantara, N.; Boix, P. P.; Kulkarni, S. A.; Mhaisalkar, S.; Grätzel, M.; Park, N.-G. High Efficiency Solid-State Sensitized Solar Cell-Based on Submicrometer Rutile TiO_2 Nanorod and $CH_3NH_3PbI_3$ Perovskite Sensitizer. *Nano Lett* **2013,** *13*, 2412-2417.

31. Zhang, Q.; Myers, D.; Lan, J.; Jenekhe, S. A.; Cao, G. Applications of light scattering in dye-sensitized solar cells. *Physical chemistry chemical physics : PCCP* **2012,** *14*, 14982-14998.

32. Cooper, G. M., *The Cell: A Molecular Approach*. 2nd ed.; **2000**.

33. Ondersma, J. W.; Hamann, T. W. Recombination and redox couples in dye-sensitized solar cells. *Coord Chem Rev* **2013,** *257*, 1533-1543.

34. Brennan, B. J.; Llansola Portoles, M. J.; Liddell, P. A.; Moore, T. A.; Moore, A. L.; Gust, D. Comparison of silatrane, phosphonic acid, and carboxylic acid functional groups for attachment of porphyrin sensitizers to TiO2 in photoelectrochemical cells. *Physical chemistry chemical physics : PCCP* **2013,** *15*, 16605-16614.

35. Zhang, L.; Cole, J. M. Anchoring groups for dye-sensitized solar cells. *ACS Appl Mater Interfaces* **2015,** *7*, 3427-3455.

36. Gratzel, M. Recent Advances in Sensitized Mesoscopic Solar Cells. *Acc Chem Res* **2009,** *42*, 1788-1798.

37. Nazeeruddin, M. K.; Kay, A.; Rodicio, I.; Humphry-Baker, R.; Mueller, E.; Liska, P.; Vlachopoulos, N.; Graetzel, M. Conversion of light to electricity by cis-X2bis(2,2'-bipyridyl-4,4'-dicarboxylate)ruthenium(II) charge-transfer sensitizers (X = Cl-, Br-, I-, CN-, and SCN-) on nanocrystalline titanium dioxide electrodes. *J Am Chem Soc* **1993,** *115*, 6382-6390.

38. Nazeeruddin, M. K.; Zakeeruddin, S. M.; Humphry-Baker, R.; Jirousek, M.; Liska, P.; Vlachopoulos, N.; Shklover, V.; Fischer, C.-H.; Grätzel, M. Acid-Base Equilibria of (2,2‘-Bipyridyl-4,4‘-dicarboxylic acid)ruthenium(II) Complexes and the Effect of Protonation on Charge-Transfer Sensitization of Nanocrystalline Titania. *Inorg Chem* **1999,** *38*, 6298-6305.

39. Nazeeruddin, M. K.; Péchy, P.; Renouard, T.; Zakeeruddin, S. M.; Humphry-Baker, R.; Comte, P.; Liska, P.; Cevey, L.; Costa, E.; Shklover, V.; Spiccia, L.; Deacon, G. B.; Bignozzi, C. A.; Grätzel, M. Engineering of Efficient Panchromatic Sensitizers for Nanocrystalline TiO_2-Based Solar Cells. *J Am Chem Soc* **2001,** *123*, 1613-1624.

40. Mishra, A.; Fischer, M. K. R.; Bäuerle, P. Metal-Free Organic Dyes for Dye-Sensitized Solar Cells: From Structure: Property Relationships to Design Rules. *Angew Chem Int Ed* **2009,** *48*, 2474-2499.

41. Ludin, N. A.; Al-Alwani Mahmoud, A. M.; Bakar Mohamad, A.; Kadhum, A. A. H.; Sopian, K.; Abdul Karim, N. S. Review on the development of natural dye photosensitizer for dye-sensitized solar cells. *Renew Sust Energ Rev* **2014,** *31*, 386-396.

42. Hug, H.; Bader, M.; Mair, P.; Glatzel, T. Biophotovoltaics: Natural pigments in dye-sensitized solar cells. *Appl Energy* **2014,** *115*, 216-225.

43. van Hasselt, P. R. Photo-Oxidation of Leaf Pigments in Cucumis Leaf Discs during Chilling. *Acta Bot Neerl* **1972,** *21*, 539-548.

44. Gross, J., *Pigments in vegetables: chlorophylls and carotenoids*. Springer Science & Business Media: **2012**.

45. Liu, W.-L.; Lin, F.-C.; Yang, Y.-C.; Huang, C.-H.; Gwo, S.; Huang, M. H.; Huang, J.-S. The influence of shell thickness of Au@TiO2 core-shell nanoparticles on the plasmonic enhancement effect in dye-sensitized solar cells. *Nanoscale* **2013,** *5*, 7953-7962.

46. Yang, Y.; Jankowiak, R.; Lin, C.; Pawlak, K.; Reus, M.; Holzwarth, A. R.; Li, J. Effect of the LHCII pigment-protein complex aggregation on photovoltaic properties of sensitized TiO_2 solar cells. *Phys Chem Chem Phys* **2014,** *16*, 20856-20865.

47. Blankenship, R. E., *Molecular mechanisms of photosynthesis*. John Wiley & Sons: **2013**.

48. Fleming, G. R.; Schlau-Cohen, G. S.; Amarnath, K.; Zaks, J. Design principles of photosynthetic light-harvesting. *Faraday Discuss* **2012,** *155*, 27-41.

49. Duffy, C. D. P.; Ruban, A. V.; Barford, W. Theoretical Investigation of the Role of Strongly Coupled Chlorophyll Dimers in Photoprotection of LHCII. *J Phys Chem B* **2008,** *112*, 12508-12515.

50. Pascal, A. A.; Liu, Z.; Broess, K.; van Oort, B.; van Amerongen, H.; Wang, C.; Horton, P.; Robert, B.; Chang, W.; Ruban, A. Molecular basis of photoprotection and control of photosynthetic light-harvesting. *Nature* **2005,** *436*, 134-137.

51. Das, R.; Kiley, P. J.; Segal, M.; Norville, J.; Yu, A. A.; Wang, L.; Trammell, S. A.; Reddick, L. E.; Kumar, R.; Stellacci, F.; Lebedev, N.; Schnur, J.; Bruce, B. D.; Zhang, S.; Baldo, M. Integration of Photosynthetic Protein Molecular Complexes in Solid-State Electronic Devices. *Nano Lett* **2004,** *4*, 1079-1083.

52. den Hollander, M.-J.; Magis, J. G.; Fuchsenberger, P.; Aartsma, T. J.; Jones, M. R.; Frese, R. N. Enhanced Photocurrent Generation by Photosynthetic Bacterial Reaction Centers through Molecular Relays, Light-Harvesting Complexes, and Direct Protein–Gold Interactions. *Langmuir* **2011,** *27*, 10282-10294.

53. Sumino, A.; Dewa, T.; Sasaki, N.; Kondo, M.; Nango, M. Electron Conduction and Photocurrent Generation of a Light-Harvesting/Reaction Center Core Complex in Lipid Membrane Environments. *J Phys Chem Lett* **2013,** *4*, 1087-1092.

54. Gerster, D.; Reichert, J.; Bi, H.; Barth, J. V.; Kaniber, S. M.; Holleitner, A. W.; Visoly-Fisher, I.; Sergani, S.; Carmeli, I. Photocurrent of a single photosynthetic protein. *Nat Nano* **2012,** *7*, 673-676.

55. Narayan, M. R. Review: Dye sensitized solar cells based on natural photosensitizers. *Renew Sust Energ Rev* **2012,** *16*, 208-215.

56. Nagata, M.; Amano, M.; Joke, T.; Fujii, K.; Okuda, A.; Kondo, M.; Ishigure, S.; Dewa, T.; Iida, K.; Secundo, F.; Amao, Y.; Hashimoto, H.; Nango, M. Immobilization and Photocurrent Activity of a Light-Harvesting Antenna Complex II, LHCII, Isolated from a Plant on Electrodes. *ACS Macro Lett* **2012,** *1*, 296-299.

57. Mershin, A.; Matsumoto, K.; Kaiser, L.; Yu, D.; Vaughn, M.; Nazeeruddin, M. K.; Bruce, B. D.; Graetzel, M.; Zhang, S. Self-assembled photosystem-I biophotovoltaics on nanostructured TiO_2 and ZnO. *Sci Rep* **2012,** *2*.

58. Polman, A. Plasmonics Applied. *Science* **2008,** *322*, 868-869.

59. Zhang, X.; Chen, Y. L.; Liu, R.-S.; Tsai, D. P. Plasmonic photocatalysis. *Reports on progress in physics. Physical Society* **2013,** *76*, 046401.

60. Wang, P.; Huang, B.; Dai, Y.; Whangbo, M.-H. Plasmonic photocatalysts: harvesting visible light with noble metal nanoparticles. *Physical chemistry chemical physics : PCCP* **2012,** *14*, 9813-9825.

61. Atwater, H. A.; Polman, A. Plasmonics for improved photovoltaic devices. *Nat Mater* **2010,** *9*, 205-13.

62. Kelly, K. L.; Coronado, E.; Zhao, L. L.; Schatz, G. C. The Optical Properties of Metal Nanoparticles: The Influence of Size, Shape, and Dielectric Environment. *J Phys Chem B* **2003,** *107*, 668-677.

63. Jain, P. K.; Lee, K. S.; El-Sayed, I. H.; El-Sayed, M. A. Calculated Absorption and Scattering Properties of Gold Nanoparticles of Different Size, Shape, and Composition: Applications in Biological Imaging and Biomedicine. *J Phys Chem B* **2006,** *110*, 7238-7248.

64. Link, S.; Wang, Z. L.; El-Sayed, M. A. Alloy Formation of Gold−Silver Nanoparticles and the Dependence of the Plasmon Absorption on Their Composition. *J Phys Chem B* **1999,** *103*, 3529-3533.

65. Ghosh, S. K.; Pal, T. Interparticle Coupling Effect on the Surface Plasmon Resonance of Gold Nanoparticles: From Theory to Applications. *Chem Rev* **2007,** *107*, 4797-4862.

66. Anger, P.; Bharadwaj, P.; Novotny, L. Enhancement and quenching of single-molecule fluorescence. *Phys Rev Lett* **2006,** *96*, 113002.

67. Maier, S. A.; Atwater, H. A. Plasmonics: Localization and guiding of electromagnetic energy in metal/dielectric structures. *J Appl Phys* **2005,** *98*, 011101.

68. Cade, N. I.; Ritman-Meer, T.; Kwakwa, K. A.; Richards, D. The plasmonic engineering of metal nanoparticles for enhanced fluorescence and Raman scattering. *Nanotechnology* **2009,** *20*, 285201.

69. Brown, M. D.; Suteewong, T.; Kumar, R. S. S.; D'Innocenzo, V.; Petrozza, A.; Lee, M. M.; Wiesner, U.; Snaith, H. J. Plasmonic Dye-Sensitized Solar Cells Using Core-Shell Metal-Insulator Nanoparticles. *Nano Lett* **2011,** *11*, 438-445.

70. Du, J.; Qi, J.; Wang, D.; Tang, Z. Facile synthesis of Au@TiO_2 core-shell hollow spheres for dye-sensitized solar cells with remarkably improved efficiency. *Energy Environ Sci* **2012,** *5*, 6914-6918.

71. Ding, B.; Lee, B. J.; Yang, M. J.; Jung, H. S.; Lee, J. K. Surface-Plasmon Assisted Energy Conversion in Dye-Sensitized Solar Cells. *Adv Energy Mater* **2011,** *1*, 415-421.

72. Hagglund, C.; Zach, M.; Kasemo, B. Enhanced charge carrier generation in dye sensitized solar cells by nanoparticle plasmons. *Appl Phys Lett* **2008,** *92*.

73. Qi, J.; Dang, X.; Hammond, P. T.; Belcher, A. M. Highly Efficient Plasmon-Enhanced Dye-Sensitized Solar Cells through Metal@Oxide Core–Shell Nanostructure. *ACS Nano* **2011,** *5*, 7108-7116.

74. Sheng, X.; He, D.; Yang, J.; Zhu, K.; Feng, X. Oriented Assembled TiO_2 Hierarchical Nanowire Arrays with Fast Electron Transport Properties. *Nano Lett* **2014,** *14*, 1848-1852.

75. Tetreault, N.; Gratzel, M. Novel nanostructures for next generation dye-sensitized solar cells. *Energy Environ Sci* **2012,** *5*, 8506-8516.

76. Park, N. G.; van de Lagemaat, J.; Frank, A. J. Comparison of Dye-Sensitized Rutile- and Anatase-Based TiO2 Solar Cells. *J Phys Chem B* **2000,** *104*, 8989-8994.

77. Schattauer, S.; Reinhold, B.; Albrecht, S.; Fahrenson, C.; Schubert, M.; Janietz, S.; Neher, D. Influence of sintering on the structural and electronic properties of TiO_2 nanoporous layers prepared via a non-sol–gel approach. *Colloid Polym Sci* **2012,** *290*, 1843-1854.

78. Zheng, Y.; Klankowski, S.; Yang, Y.; Li, J. Preparation and Characterization of TiO_2 Barrier Layers for Dye-Sensitized Solar Cells. *ACS Appl Mater Interfaces* **2014,** *6*, 10679-10686.

79. Hagfeldt, A.; Boschloo, G.; Sun, L.; Kloo, L.; Pettersson, H. Dye-Sensitized Solar Cells. *Chem Rev* **2010,** *110*, 6595-6663.

80. Caffarri, S.; Kouřil, R.; Kereïche, S.; Boekema, E. J.; Croce, R. Functional architecture of higher plant photosystem II supercomplexes. *EMBO J* **2009,** *28*, 3052-3063.

81. Liu, Z.; Yan, H.; Wang, K.; Kuang, T.; Zhang, J.; Gui, L.; An, X.; Chang, W. Crystal structure of spinach major light-harvesting complex at 2.72 Å resolution. *Nature* **2004,** *428*, 287-292.

82. Johnson, M. P.; Goral, T. K.; Duffy, C. D. P.; Brain, A. P. R.; Mullineaux, C. W.; Ruban, A. V. Photoprotective Energy Dissipation Involves the Reorganization of Photosystem II Light-Harvesting Complexes in the Grana Membranes of Spinach Chloroplasts. *Plant Cell* **2011,** *23*, 1468-1479.

83. Holzwarth, A. R.; Miloslavina, Y.; Nilkens, M.; Jahns, P. Identification of two quenching sites active in the regulation of photosynthetic light-harvesting studied by time-resolved fluorescence. *Chem Phys Lett* **2009,** *483*, 262-267.

84. Belgio, E.; Duffy, C. D. P.; Ruban, A. V. Switching light harvesting complex II into photoprotective state involves the lumen-facing apoprotein loop. *Physical chemistry chemical physics : PCCP* **2013,** *15*, 12253-12261.

85. Ruban, A. V.; Berera, R.; Ilioaia, C.; van Stokkum, I. H. M.; Kennis, J. T. M.; Pascal, A. A.; van Amerongen, H.; Robert, B.; Horton, P.; van Grondelle, R. Identification of a mechanism of photoprotective energy dissipation in higher plants. *Nature* **2007,** *450*, 575-578.

86. Holzwarth, A. R.; Jahns, P., *NPQ mechanisms in intact organisms as derived from ultrafast fluorescence kinetics studies*. Springer Science: Advances in Photosynthesis and Respiration, **2014**; Vol. 40.

87. Miloslavina, Y.; Wehner, A.; Lambrev, P. H.; Wientjes, E.; Reus, M.; Garab, G.; Croce, R.; Holzwarth, A. R. Far-red fluorescence: A direct spectroscopic marker for LHCII oligomer formation in non-photochemical quenching. *FEBS Lett* **2008,** *582*, 3625-3631.

88. Magdaong, N.; Enriquez, M.; LaFountain, A.; Rafka, L.; Frank, H. Effect of protein aggregation on the spectroscopic properties and excited state kinetics of the LHCII pigment–protein complex from green plants. *Photosynth Res* **2013,** *118*, 18.

89. Kell, A.; Feng, X.; Lin, C.; Yang, Y.; Li, J.; Reus, M.; Holzwarth, A. R.; Jankowiak, R. Charge-transfer character of the low-energy Chl a Qy absorption band in aggregated light harvesting complexes II. *J Phys Chem B* **2014,** *118*, 6086-6091.

90. Lambrev, P. H.; Várkonyi, Z.; Krumova, S.; Kovács, L.; Miloslavina, Y.; Holzwarth, A. R.; Garab, G. Importance of trimer–trimer interactions for the native state of the plant light-harvesting complex II. *Biochim Biophys Acta-Bioenergetics* **2007,** *1767*, 847-853.

91. Porra, R. J.; Thompson, W. A.; Kriedemann, P. E. Determination of accurate extinction coefficients and simultaneous equations for assaying chlorophylls a and b extracted with

four different solvents: verification of the concentration of chlorophyll standards by atomic absorption spectroscopy. *Biochim Biophys Acta-Bioenergetics* **1989,** *975*, 384-394.

92. Müller, M. G.; Lambrev, P.; Reus, M.; Wientjes, E.; Croce, R.; Holzwarth, A. R. Singlet Energy Dissipation in the Photosystem II Light-Harvesting Complex Does Not Involve Energy Transfer to Carotenoids. *ChemPhysChem* **2010,** *11*, 1289-1296.

93. Magdaong, N.; Enriquez, M.; LaFountain, A.; Rafka, L.; Frank, H. Effect of protein aggregation on the spectroscopic properties and excited state kinetics of the LHCII pigment–protein complex from green plants. *Photosynth Res* **2013,** *118*, 259-276.

94. Gruszecki, W. a. I.; Janik, E.; Luchowski, R.; Kernen, P.; Grudzinski, W.; Gryczynski, I.; Gryczynski, Z. Supramolecular Organization of the Main Photosynthetic Antenna Complex LHCII: A Monomolecular Layer Study. *Langmuir* **2009,** *25*, 9384-9391.

95. Renger, T.; Madjet, M. E.; Knorr, A.; Müh, F. How the molecular structure determines the flow of excitation energy in plant light-harvesting complex II. *J Plant Physiol* **2011,** *168*, 1497-1509.

96. Mackowski, S. Hybrid nanostructures for efficient light harvesting. *Journal of physics. Condensed matter : an Institute of Physics journal* **2010,** *22*, 193102.

97. Carmeli, I.; Lieberman, I.; Kraversky, L.; Fan, Z.; Govorov, A. O.; Markovich, G.; Richter, S. Broad Band Enhancement of Light Absorption in Photosystem I by Metal Nanoparticle Antennas. *Nano Lett* **2010,** *10*, 2069-2074.

98. Czechowski, N.; Nyga, P.; Schmidt, M.; Brotosudarmo, T. P.; Scheer, H.; Piatkowski, D.; Mackowski, S. Absorption Enhancement in Peridinin-Chlorophyll-Protein Light-Harvesting Complexes Coupled to Semicontinuous Silver Film. *Plasmonics* **2012,** *7*, 115-121.

99. Mackowski, S.; Wörmke, S.; Maier, A. J.; Brotosudarmo, T. H. P.; Harutyunyan, H.; Hartschuh, A.; Govorov, A. O.; Scheer, H.; Bräuchle, C. Metal-Enhanced Fluorescence of Chlorophylls in Single Light-Harvesting Complexes. *Nano Lett* **2008,** *8*, 558-564.

100. Beyer, S. R.; Ullrich, S.; Kudera, S.; Gardiner, A. T.; Cogdell, R. J.; Köhler, J. Hybrid Nanostructures for Enhanced Light-Harvesting: Plasmon Induced Increase in Fluorescence from Individual Photosynthetic Pigment–Protein Complexes. *Nano Lett* **2011,** *11*, 4897-4901.

101. Govorov, A. O.; Carmeli, I. Hybrid Structures Composed of Photosynthetic System and Metal Nanoparticles: Plasmon Enhancement Effect. *Nano Lett* **2007,** *7*, 620-625.

102. Dang, X.; Qi, J.; Klug, M. T.; Chen, P.-Y.; Yun, D. S.; Fang, N. X.; Hammond, P. T.; Belcher, A. M. Tunable Localized Surface Plasmon-Enabled Broadband Light-Harvesting Enhancement for High-Efficiency Panchromatic Dye-Sensitized Solar Cells. *Nano Lett* **2013,** *13*, 637-642.

103. Zhang, W.; Saliba, M.; Stranks, S. D.; Sun, Y.; Shi, X.; Wiesner, U.; Snaith, H. J. Enhancement of Perovskite-Based Solar Cells Employing Core–Shell Metal Nanoparticles. *Nano Lett* **2013,** *13*, 4505-4510.

104. Saliba, M.; Zhang, W.; Burlakov, V. M.; Stranks, S. D.; Sun, Y.; Ball, J. M.; Johnston, M. B.; Goriely, A.; Wiesner, U.; Snaith, H. J. Plasmonic-Induced Photon Recycling in Metal Halide Perovskite Solar Cells. *Adv Funct Mater* **2015,** *25*, 5038-5046.

105. Adhyaksa, G. W. P.; Prima, E. C.; Lee, D. K.; Ock, I.; Yatman, S.; Yuliarto, B.; Kang, J. K. A Light Harvesting Antenna Using Natural Extract Graminoids Coupled with Plasmonic Metal Nanoparticles for Bio-Photovoltaic Cells. *Adv Energy Mater* **2014,** *4*, 1400470-1400477.

106. Zhang, Q.; Li, N.; Goebl, J.; Lu, Z.; Yin, Y. A Systematic Study of the Synthesis of Silver Nanoplates: Is Citrate a "Magic" Reagent? *J Am Chem Soc* **2011,** *133*, 18931-18939.

107. Yang, Y.; Jankowiak, R.; Lin, C.; Pawlak, K.; Reus, M.; Holzwarth, A. R.; Li, J. Effect of the LHCII Pigment–Protein Complex Aggregation on Photovoltaic Properties of Sensitized TiO_2 Solar Cells. *Physical chemistry chemical physics : PCCP* **2014,** *16*, 20856-20865.

108. Wang, Y.; Wen, C.; Hodgson, P.; Li, Y. Biocompatibility of TiO2 nanotubes with different topographies. *Journal of biomedical materials research. Part A* **2014,** *102*, 743-751.

109. Cushing, S. K.; Li, J.; Bright, J.; Yost, B. T.; Zheng, P.; Bristow, A. D.; Wu, N. Controlling Plasmon-Induced Resonance Energy Transfer and Hot Electron Injection Processes in Metal@TiO_2 Core–Shell Nanoparticles. *J Phys Chem C* **2015,** *119*, 16239-16244.

110. Cushing, S. K.; Wu, N. Progress and Perspectives of Plasmon-Enhanced Solar Energy Conversion. *J Phys Chem Lett* **2016,** *7*, 666-675.

111. Götze, J. P.; Kröner, D.; Banerjee, S.; Karasulu, B.; Thiel, W. Carotenoids as a Shortcut for Chlorophyll Soret-to-Q Band Energy Flow. *ChemPhysChem* **2014,** *15*, 3392-3401.

112. Wu, W.-Q.; Lei, B.-X.; Rao, H.-S.; Xu, Y.-F.; Wang, Y.-F.; Su, C.-Y.; Kuang, D.-B. Hydrothermal Fabrication of Hierarchically Anatase TiO2 Nanowire arrays on FTO Glass for Dye-sensitized Solar Cells. *Sci Rep* **2013,** *3*.

113. Roh, D. K.; Chi, W. S.; Jeon, H.; Kim, S. J.; Kim, J. H. High Efficiency Solid-State Dye-Sensitized Solar Cells Assembled with Hierarchical Anatase Pine Tree-like TiO2 Nanotubes. *Adv Funct Mater* **2014,** *24*, 379-386.

114. Wu, W.-Q.; Xu, Y.-F.; Su, C.-Y.; Kuang, D.-B. Ultra-long anatase TiO_2 nanowire arrays with multi-layered configuration on FTO glass for high-efficiency dye-sensitized solar cells. *Energy Environ Sci* **2014,** *7*, 644-649.

115. Oliveira, M. C. d.; Fraga, A. L. S.; Thesing, A.; Andrade, R. L. d.; Santos, J. F. L.; Santos, M. J. L. Interface Dependent Plasmon Induced Enhancement in Dye-Sensitized Solar Cells Using Gold Nanoparticles. *J Nanomater* **2015,** *2015*, 9.

116. García de Arquer, F. P.; Mihi, A.; Kufer, D.; Konstantatos, G. Photoelectric Energy Conversion of Plasmon-Generated Hot Carriers in Metal-Insulator-Semiconductor Structures. *ACS Nano* **2013,** *7*, 3581-3588.

117. Lee, H.; Lee, Y. K.; Hwang, E.; Park, J. Y. Enhanced Surface Plasmon Effect of Ag/TiO_2 Nanodiodes on Internal Photoemission. *J Phys Chem C* **2014,** *118*, 5650-5656.

118. Lee, Y. K.; Park, J.; Park, J. Y. The Effect of Dye Molecules and Surface Plasmons in Photon-Induced Hot Electron Flows Detected on Au/TiO_2 Nanodiodes. *J Phys Chem C* **2012,** *116*, 18591-18596.

119. Jiang, Z.; Zhu, J.; Liu, D.; Wei, W.; Xie, J.; Chen, M. In situ synthesis of bimetallic Ag/Pt loaded single-crystalline anatase TiO2 hollow nano-hemispheres and their improved photocatalytic properties. *CrystEngComm* **2014,** *16*, 2384-2394.

120. Jang, Y. H.; Jang, Y. J.; Kochuveedu, S. T.; Byun, M.; Lin, Z.; Kim, D. H. Plasmonic Dye-Sensitized Solar Cells Incorporated with Au-TiO_2 Nanostructures with Tailored Configurations. *Nanoscale* **2014,** *6*, 1823-1832.

121. Clavero, C. Plasmon-induced hot-electron generation at nanoparticle/metal-oxide interfaces for photovoltaic and photocatalytic devices. *Nat Photon* **2014,** *8*, 95-103.

122. Knight, M. W.; Sobhani, H.; Nordlander, P.; Halas, N. J. Photodetection with Active Optical Antennas. *Science* **2011,** *332*, 702-704.

123. McFarland, E. W.; Tang, J. A Photovoltaic Device Structure Based on Internal Electron Emission. *Nature* **2003,** *421*, 616-618.

124. Tian, Y.; Tatsuma, T. Mechanisms and Applications of Plasmon-Induced Charge Separation at TiO_2 Films Loaded with Gold Nanoparticles. *J Am Chem Soc* **2005,** *127*, 7632-7637.

125. Chen, Z. H.; Tang, Y. B.; Liu, C. P.; Leung, Y. H.; Yuan, G. D.; Chen, L. M.; Wang, Y. Q.; Bello, I.; Zapien, J. A.; Zhang, W. J.; Lee, C. S.; Lee, S. T. Vertically Aligned ZnO Nanorod Arrays Sentisized with Gold Nanoparticles for Schottky Barrier Photovoltaic Cells. *The Journal of Physical Chemistry C* **2009,** *113*, 13433-13437.

126. Son, M.-S.; Im, J.-E.; Wang, K.-K.; Oh, S.-L.; Kim, Y.-R.; Yoo, K.-H. Surface plasmon enhanced photoconductance and single electron effects in mesoporous titania nanofibers loaded with gold nanoparticles. *Appl Phys Lett* **2010,** *96*, 023115.

127. Mubeen, S.; Hernandez-Sosa, G.; Moses, D.; Lee, J.; Moskovits, M. Plasmonic Photosensitization of a Wide Band Gap Semiconductor: Converting Plasmons to Charge Carriers. *Nano Lett* **2011,** *11*, 5548-5552.

128. Yang, Y.; Gobeze, H. B.; D'Souza, F.; Jankowiak, R.; Li, J. Plasmonic Enhancement of Biosolar Cells Employing Light Harvesting Complex II Incorporated with Core-Shell Metal@TiO_2 Nanoparticles. *Adv Mater Interfaces* **2016**, DOI: 10.1002/admi.201600371.

129. Adachi, M.; Murata, Y.; Takao, J.; Jiu, J.; Sakamoto, M.; Wang, F. Highly efficient dye-sensitized solar cells with a titania thin-film electrode composed of a network structure of single-crystal-like TiO_2 nanowires made by the "oriented attachment" mechanism. *J Am Chem Soc* **2004,** *126*, 14943-14949.

130. Li, W.; Zhao, D. Extension of the Stöber Method to Construct Mesoporous SiO_2 and TiO_2 Shells for Uniform Multifunctional Core–Shell Structures. *Adv Mater* **2013,** *25*, 142-149.

131. Zhang, J.; Li, M.; Feng, Z.; Chen, J.; Li, C. UV Raman Spectroscopic Study on TiO2. I. Phase Transformation at the Surface and in the Bulk. *J Phys Chem B* **2006,** *110*, 927-935.

132. Kawahara, T.; Konishi, Y.; Tada, H.; Tohge, N.; Nishii, J.; Ito, S. A Patterned TiO_2(Anatase)/TiO_2(Rutile) Bilayer-Type Photocatalyst: Effect of the Anatase/Rutile Junction on the Photocatalytic Activity. *Angew Chem* **2002,** *114*, 2935-2937.

133. Di Valentin, C.; Pacchioni, G.; Selloni, A. Origin of The Different Photoactivity of N-Doped Anatase and Rutile TiO_2. *Phys Rev B* **2004,** *70*, 085116.

134. Li, Z.; Rochford, C.; Baca, F. J.; Liu, J.; Li, J.; Wu, J. Investigation into Photoconductivity in Single CNF/TiO_2-Dye Core-Shell Nanowire Devices. *Nanoscale Res Lett* **2010,** *5*, 1480-1486.

135. Rochford, C.; Li, Z.-Z.; Baca, J.; Liu, J.; Li, J.; Wu, J. The effect of annealing on the photoconductivity of carbon nanofiber/TiO_2 core-shell nanowires for use in dye-sensitized solar cells. *Appl Phys Lett* **2010,** *97*, 043102.

136. Subramanian, V.; Wolf, E. E.; Kamat, P. V. Catalysis with TiO_2/Gold Nanocomposites. Effect of Metal Particle Size on the Fermi Level Equilibration. *J Am Chem Soc* **2004,** *126*, 4943-4950.

137. Göpel, W.; Rocker, G.; Feierabend, R. Intrinsic defects of TiO_2 (110): Interaction with chemisorbed O_2, H_2, CO, and CO_2. *Phys Rev B* **1983,** *28*, 3427-3438.

138. Kell, A.; Bednarczyk, D.; Acharya, K.; Chen, J.; Noy, D.; Jankowiak, R. New Insight into the Water-Soluble Chlorophyll-Binding Protein from Lepidium virginicum. *Photochem Photobiol* **2016,** *92*, 428-435.

139. Horigome, D.; Satoh, H.; Itoh, N.; Mitsunaga, K.; Oonishi, I.; Nakagawa, A.; Uchida, A. Structural Mechanism and Photoprotective Function of Water-soluble Chlorophyll-binding Protein. *The Journal of biological chemistry* **2007,** *282*, 6525-6531.

140. Kashif, M. K.; Axelson, J. C.; Duffy, N. W.; Forsyth, C. M.; Chang, C. J.; Long, J. R.; Spiccia, L.; Bach, U. A New Direction in Dye-Sensitized Solar Cells Redox Mediator

Development: In Situ Fine-Tuning of the Cobalt(II)/(III) Redox Potential through Lewis Base Interactions. *J Am Chem Soc* **2012,** *134*, 16646-16653.

141. Yum, J.-H.; Baranoff, E.; Kessler, F.; Moehl, T.; Ahmad, S.; Bessho, T.; Marchioro, A.; Ghadiri, E.; Moser, J.-E.; Yi, C.; Nazeeruddin, M. K.; Grätzel, M. A cobalt complex redox shuttle for dye-sensitized solar cells with high open-circuit potentials. *Nat Commun* **2012,** *3*, 631.

142. Yella, A.; Lee, H.-W.; Tsao, H. N.; Yi, C.; Chandiran, A. K.; Nazeeruddin, M. K.; Diau, E. W.-G.; Yeh, C.-Y.; Zakeeruddin, S. M.; Grätzel, M. Porphyrin-Sensitized Solar Cells with Cobalt (II/III)–Based Redox Electrolyte Exceed 12 Percent Efficiency. *Science* **2011,** *334*, 629-634.

143. Xiang, W.; Huang, W.; Bach, U.; Spiccia, L. Stable high efficiency dye-sensitized solar cells based on a cobalt polymer gel electrolyte. *Chem Commun* **2013,** *49*, 8997-8999.

144. Xiang, W.; Huang, F.; Cheng, Y.-B.; Bach, U.; Spiccia, L. Aqueous dye-sensitized solar cell electrolytes based on the cobalt(ii)/(iii) tris(bipyridine) redox couple. *Energy Environ Sci* **2013,** *6*, 121-127.

145. Eperon, G. E.; Burlakov, V. M.; Docampo, P.; Goriely, A.; Snaith, H. J. Morphological Control for High Performance, Solution-Processed Planar Heterojunction Perovskite Solar Cells. *Adv Funct Mater* **2014,** *24*, 151-157.

146. Salim, T.; Sun, S.; Abe, Y.; Krishna, A.; Grimsdale, A. C.; Lam, Y. M. Perovskite-based solar cells: impact of morphology and device architecture on device performance. *J Mater Chem A* **2015,** *3*, 8943-8969.

147. Fu, K.; Nelson, C. T.; Scott, M. C.; Minor, A.; Mathews, N.; Wong, L. H. Influence of void-free perovskite capping layer on the charge recombination process in high performance CH3NH3PbI3 perovskite solar cells. *Nanoscale* **2016,** *8*, 4181-4193.

148. Snaith, H. J.; Abate, A.; Ball, J. M.; Eperon, G. E.; Leijtens, T.; Noel, N. K.; Stranks, S. D.; Wang, J. T.-W.; Wojciechowski, K.; Zhang, W. Anomalous Hysteresis in Perovskite Solar Cells. *J Phys Chem Lett* **2014,** *5*, 1511-1515.

Appendix A - Supplementary Information of Chapter 3

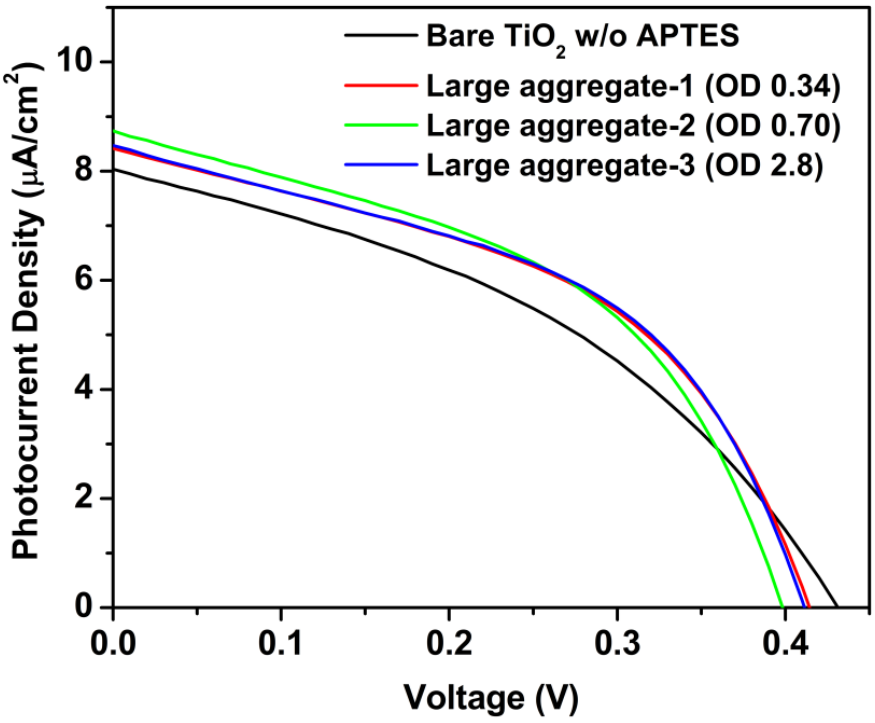

Figure A.1 I-V curves of the solar cells sensitized at different concentrations of LHCII aggregates through physisorption on the anodes with a bare TiO_2 thin layer (100~300 nm) without APTES modification.

Increasing the concentration of the LHCII aggregate solution by ~8 folds (shown with increased optical density) did not have much effect on the photocurrent of the solar cell, indicating that the physisorption of LHCII on bare TiO_2 was quite weak. (Reprinted with permission from supplementary information Y. Yang, R. Jankowiak, C. Lin, K. Pawlak, M. Reus, A. R. Holzwarthb and J. Li, *Phys. Chem. Chem. Phys.*, 2014, 16, 20856-20865.)

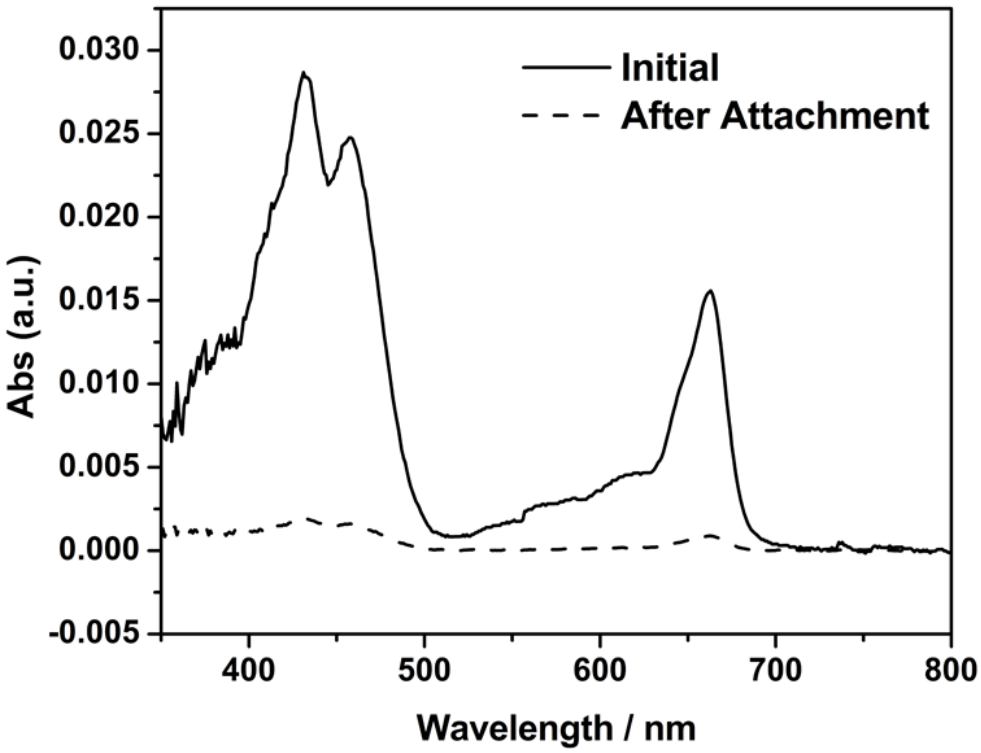

Figure A.2 UV-Vis absorption of the chlorophylls pigment extracted from LHCII aggregates in the solution before (solid line) and after (dashed line) being injected into the solar cell.

Pigment extraction and chlorophyll content calculation follows the method described in the experimental section of main text. Before injecting into the solar cell, the concentration of LHCII solution was 0.296 μg Chl/mL, which was reduced to 0.016 μg Chl/mL after incubating in the cell over 12 hrs. The lost LHCII was assumed to be adsorbed in the solar cell. The attachment efficiency (η_{attach}) can be calculated to be about 95% by $\eta_{attach} = 1 - C_{after}/C_{before}$. (Reprinted with permission from supplementary information Y. Yang, R. Jankowiak, C. Lin, K. Pawlak, M. Reus, A. R. Holzwarthb and J. Li, *Phys. Chem. Chem. Phys.*, 2014, 16, 20856-20865.)

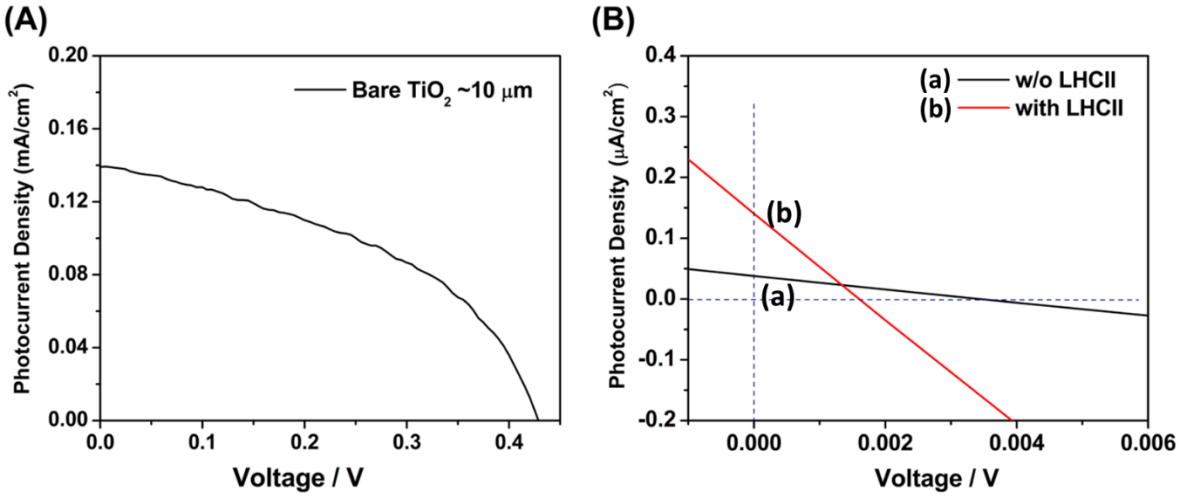

Figure A.3 (A) I-V curve of a solar cell based on a bare sintered TiO_2 nanoparticle film (~10 μm in thickness). (B) I-V curves of the solar cells built on bare APTES-FTO without the TiO_2 barrier layer, before and after sensitized with the small LHCII aggregates.

(Reprinted with permission from supplementary information Y. Yang, R. Jankowiak, C. Lin, K. Pawlak, M. Reus, A. R. Holzwarthb and J. Li, *Phys. Chem. Chem. Phys.*, 2014, 16, 20856-20865.)

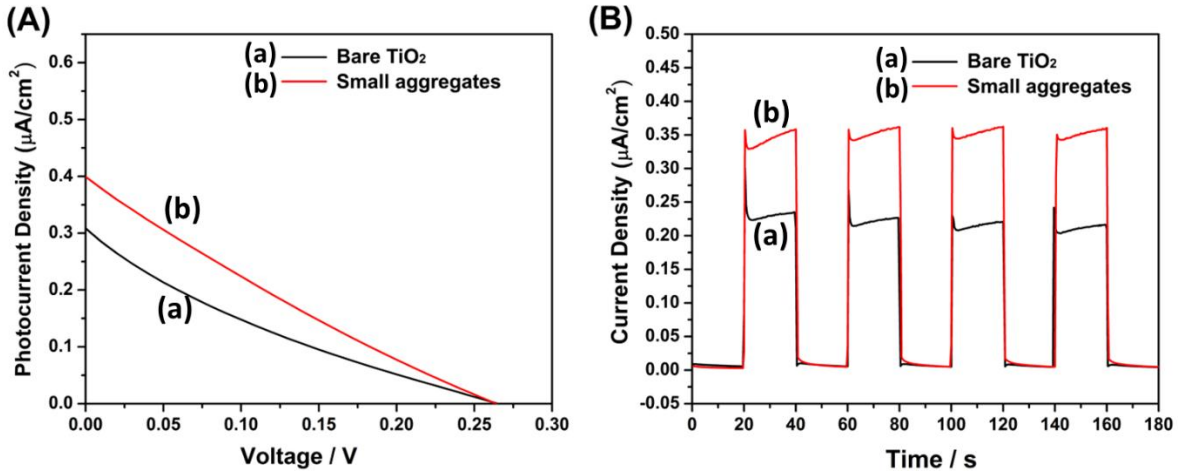

Figure A.4 (A) I-V curves and (B) photocurrent response plots of bare and small LHCII aggregate sensitized TiO_2 solar cells with an ionic liquid electrolyte (Mosalyte ADE-250, Solaronix).

(Reprinted with permission from supplementary information Y. Yang, R. Jankowiak, C. Lin, K. Pawlak, M. Reus, A. R. Holzwarthb and J. Li, *Phys. Chem. Chem. Phys.*, 2014, 16, 20856-20865.)

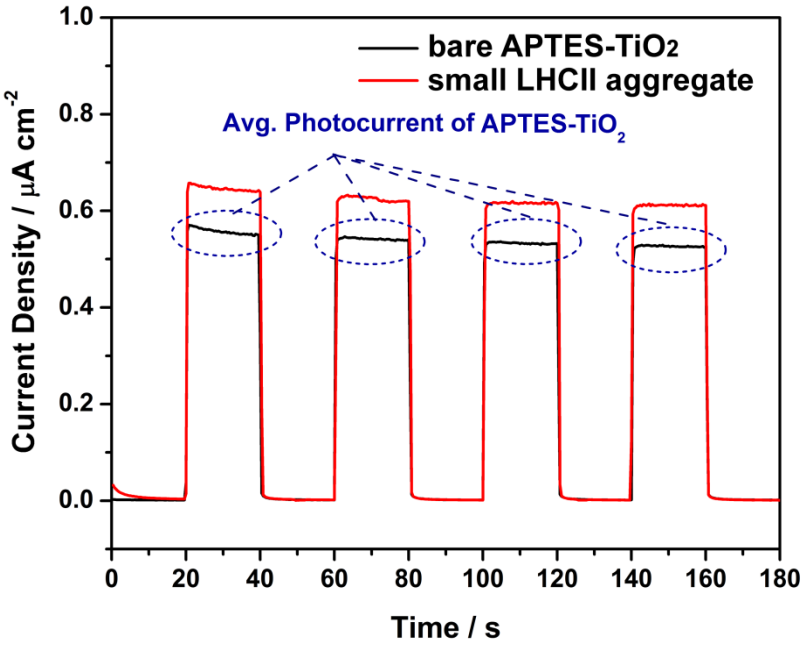

Figure A.5 Raw data of photocurrent response curves of an APTES-TiO_2 solar cell before and after being sensitized with small-size LHCII aggregates under one-Sun illumination.

(Reprinted with permission from supplementary information Y. Yang, R. Jankowiak, C. Lin, K. Pawlak, M. Reus, A. R. Holzwarthb and J. Li, *Phys. Chem. Chem. Phys.*, 2014, 16, 20856-20865.)

Normalization for all photocurrent response curves in Figure 3.7 in Chapter 3 is based on the equation below:

$$J_N = \frac{J_{LSSC} - J_{TiO_2}}{(J_{on\_TiO_2})_{avg.}}$$

J_N — Normalized current density of LSSC

J_{LSSC} — Raw current density of LHCII-sensitized solar cell (LSSC) (red line in Fig. A.5)

J_{TiO_2} — Raw current density of bare APTES-TiO_2 solar cell (black line in Fig. A.5)

$(J_{on\_TiO_2})_{avg.}$— Average of photocurrent density obtained from bare APTES-TiO_2 solar cell under illumination (blue dash circle regions shown in Fig. A.5)

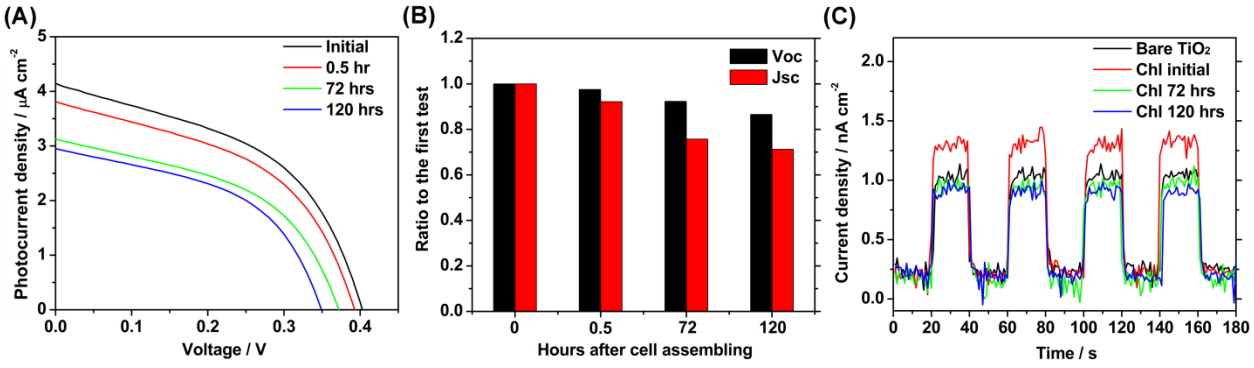

Figure A.6 Stability of Chlorophyll Sensitized Solar Cell.

(A) The time dependence of the I-V curves of a Chls sensitized TiO_2 solar cell after cell assembling (molar ratio of Chl *a* : Chl *b* = 8:6). (B) The changes of *J*sc and *V*oc obtained from the I-V curves in (A). The value of *J*sc dropped particularly fast. (C) Photocurrent responses of Chl *a* sensitized solar cell under the illumination with the interference bandpass filter at a wavelength of 675±25 nm (covering the Qy region), measured during 5 days (120 hrs) after cell assembly. (Reprinted with permission from supplementary information Y. Yang, R. Jankowiak, C. Lin, K. Pawlak, M. Reus, A. R. Holzwarthb and J. Li, *Phys. Chem. Chem. Phys.*, 2014, 16, 20856-20865.)

Appendix B - Supplementary Information of Chapter 4

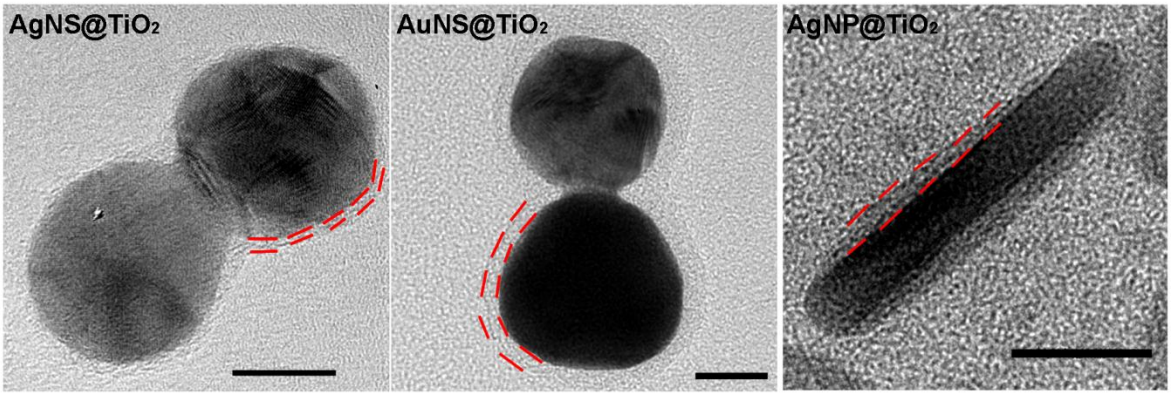

Figure B.1 HRTEM of the core-shell plasmonic nanoparticles (PNPs): AgNS@TiO_2, AuNS@TiO_2 and AgNP@TiO_2 (side view of the nanoplate).

The scale bars are 10 nm. The TiO_2 shells were 2~3 nm as highlighted with red dash lines. (Reprinted with permission from supplementary information Y. Yang, H. Gobeze, F. D'Souza, R. Jankowiak and J. Li, *Adv. Mater. Interfaces*, DOI: 10.1002/admi.201600371)

Table B.1 Parameters of the plasmonic nanoparticles (based on TEM images and ICP-AES results).

Nanoparticles	Dimension (nm)	Metal Mass Concentration (g/mL)	Particle Concentration (NPs/mL)	Particle Surface area (cm^2/mL)
AgNS@TiO_2	Ø23.4±2.5	3.9×10^{-5}	4×10^{11}	3.6
AuNS@TiO_2	Ø22.0±1.6	3.0×10^{-5}	1.2×10^{11}	3.9
AgNP@TiO_2	Ø27.3±10 H5.6±0.9	2.5×10^{-5}	1.3×10^{12}	3.5

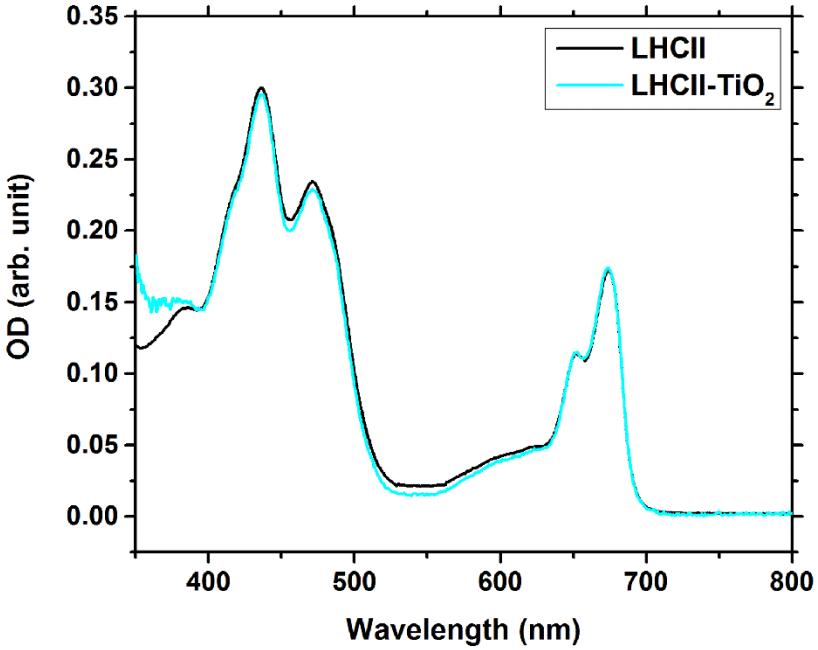

Figure B.2 The optical absorption spectra of LHCII trimers dispersed in solution (black) and the same amount of LHCII trimers attached to APTES-treated TiO_2 NPs suspended in aqueous solution (Cyan).

The cyan curve was subjected to the background correction (to subtract the absorption by TiO_2 NPs) to remove the strong scattering from TiO_2 particles. (Reprinted with permission from supplementary information Y. Yang, H. Gobeze, F. D'Souza, R. Jankowiak and J. Li, *Adv. Mater. Interfaces*, DOI: 10.1002/admi.201600371)

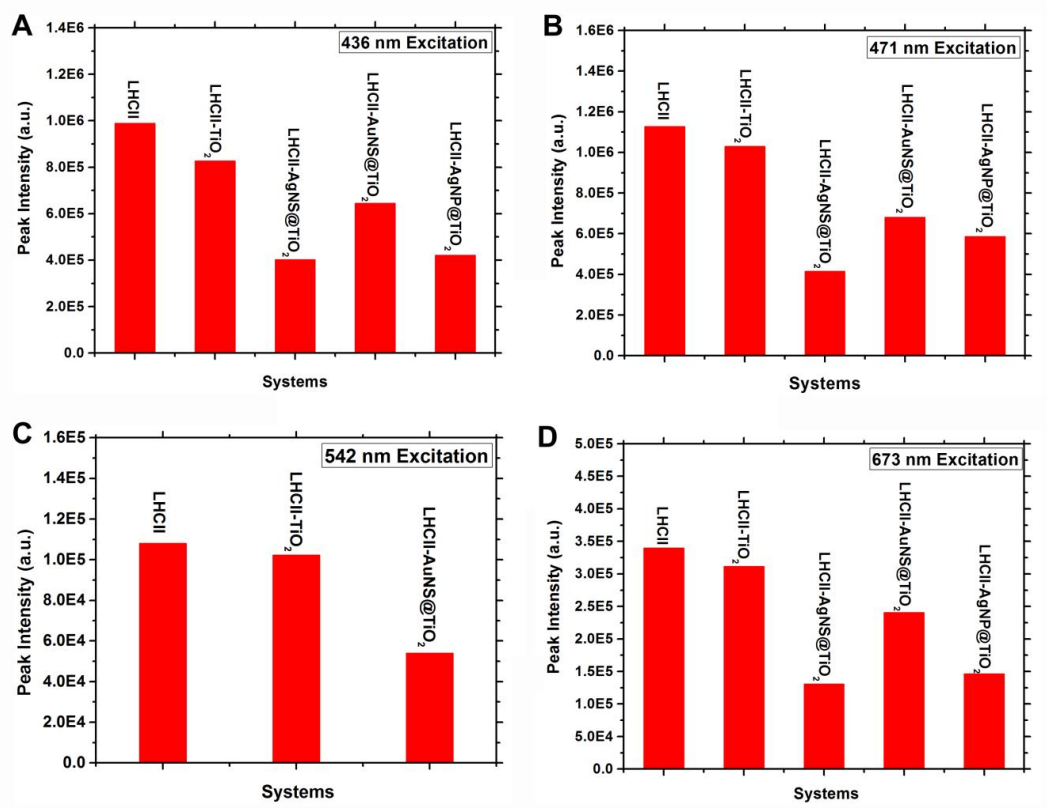

Figure B.3 Peak intensity of the fluorescence emissions of LHCII and LHCII-PNP hybrids excited at four different wavelengths. All emission peaks were at 683 nm.

(Reprinted with permission from supplementary information Y. Yang, H. Gobeze, F. D'Souza, R. Jankowiak and J. Li, *Adv. Mater. Interfaces*, DOI: 10.1002/admi.201600371)

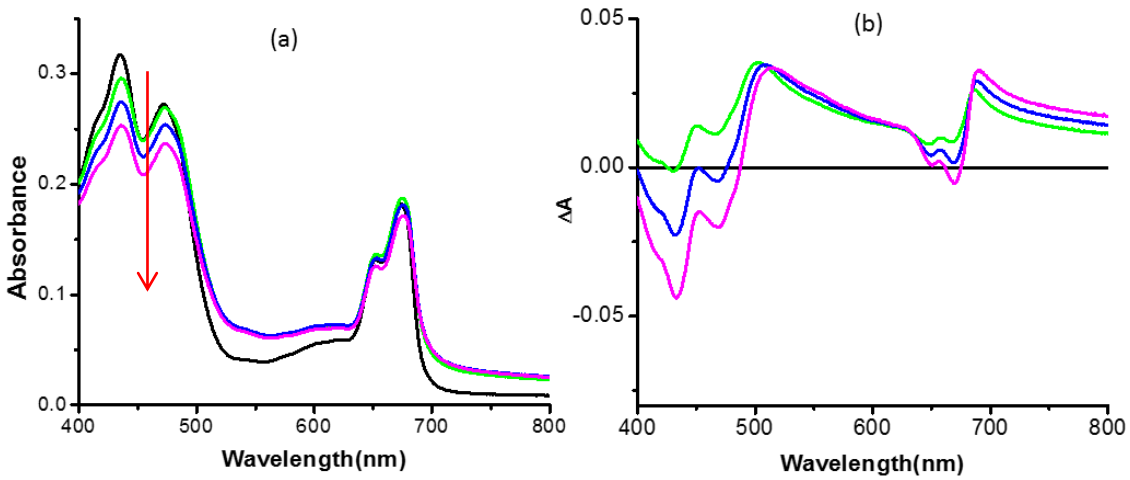

Figure B.4 Absorption spectra of the chemically oxidized LHCII.

(a) Spectral changes observed during increased addition of nitrosonium tetrafluoroborate (NTFB) to an aqueous solution of LHCII. The black curve is the absorption spectrum of neutral LHCII. The colored curves are the absorption spectra of oxidized LHCII, showing larger decrease of Chl Soret band absorption as more NTFB was added (following the direction of the red arrow). (b) Differential spectra (∆A = Abs(oxidized) - Abs(neutral)) generated to visualize the spectral features of the oxidized LHCII species (positive peaks). (Reprinted with permission from supplementary information Y. Yang, H. Gobeze, F. D'Souza, R. Jankowiak and J. Li, *Adv. Mater. Interfaces*, DOI: 10.1002/admi.201600371)

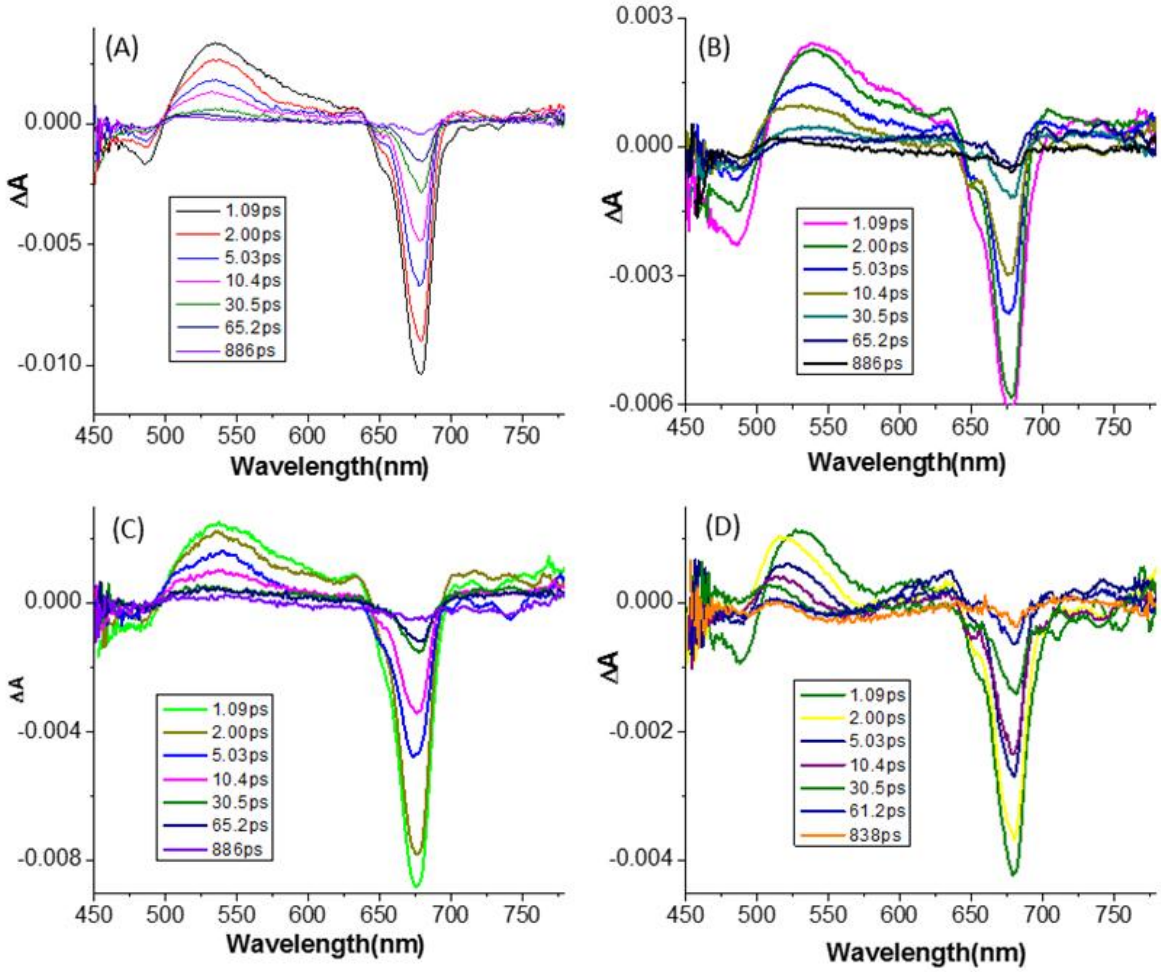

Figure B.5 Femtosecond transient absorption spectra at the indicated delay time.

(A) LHCII, (B) LHCII-AgNS@TiO_2, (C) LHCII-AuNS@TiO_2, and (D) LHCII-AgNP@TiO_2 in Ar-saturated water. (Reprinted with permission from supplementary information Y. Yang, H. Gobeze, F. D'Souza, R. Jankowiak and J. Li, *Adv. Mater. Interfaces*, DOI: 10.1002/admi.201600371)

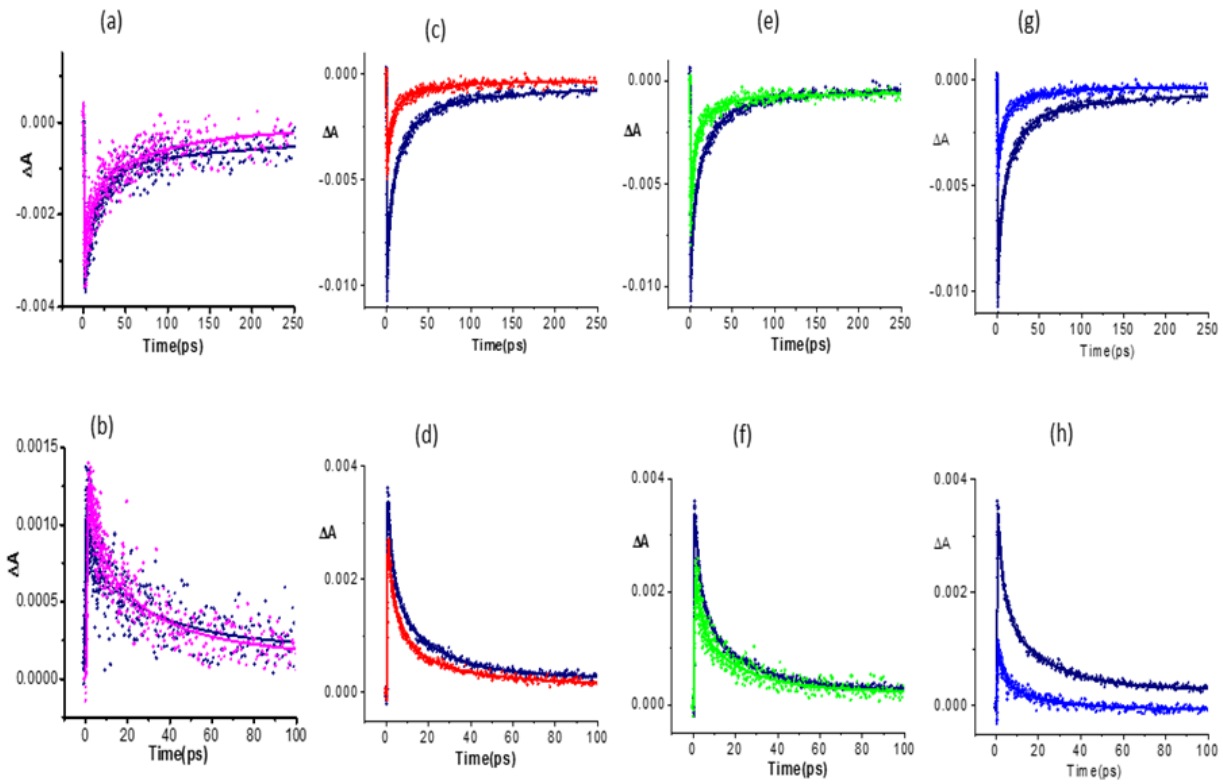

Figure B.6 Time profiles of the peak absorption at 680 nm (top panels) and 535 nm (bottom panels).

Notation: (a and b) LHCII and LHCII-TiO_2, (c and d) LHCII and LHCII-AgNS@TiO_2, (e and f) LHCII and LHCII-AuNS@TiO_2, and (g and h) LHCII and LHCII-AgNP@TiO_2 in Ar-saturated water. The LHCII time profiles are shown in navy blue. (Reprinted with permission from supplementary information Y. Yang, H. Gobeze, F. D'Souza, R. Jankowiak and J. Li, *Adv. Mater. Interfaces*, DOI: 10.1002/admi.201600371)

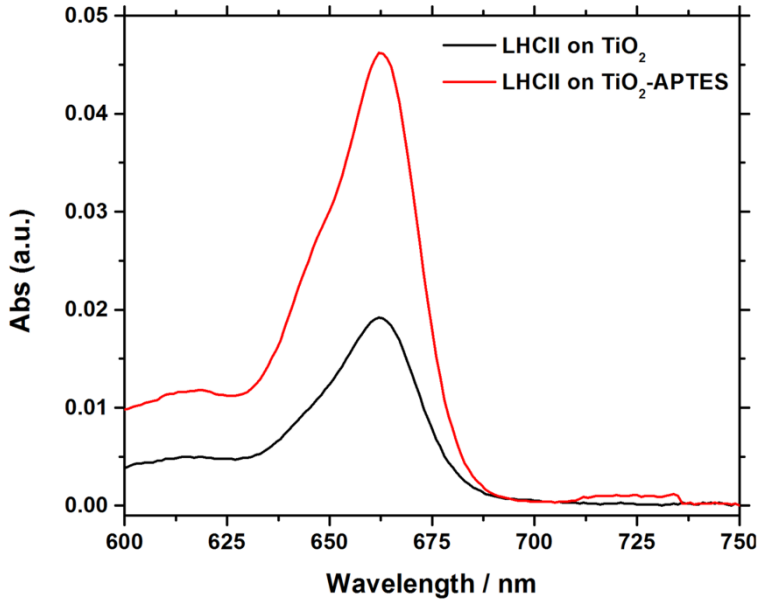

Figure B.7 UV-Vis absorption of the chlorophylls pigment extracted from the LHCII trimers adsorbed on TiO_2 nanotree photoanodes with and without APTES functionalization.

The pigment extraction followed the method described in our previous paper.[107] The adsorbed LHCII trimers in units of equivalent Chls was calculated using the absorbance at 646.6 nm and 663.6 nm based on the equation: $\mathrm{Chls}(a+b) = 17.6A^{646.6} + 7.34A^{663.6}$.[91] (Reprinted with permission from supplementary information Y. Yang, H. Gobeze, F. D'Souza, R. Jankowiak and J. Li, *Adv. Mater. Interfaces*, DOI: 10.1002/admi.201600371)

Table B.2 The characteristic values of the LHCII-sensitized solar cells with and without PNPs incorporated.

Solar cells	J_{sc} ($\mu A/cm^2$)	V_{oc} (V)	FF	η%	IPCE@665 nm
TiO_2 nanotrees	102±19	0.404±0.027	0.612±0.042	0.026±0.008	0±0.000
LHCII	135±12	0.443±0.018	0.622±0.067	0.037±0.005	0.023±0.002
LHCII-AgNS@TiO_2	201±3	0.459±0.039	0.629±0.067	0.058±0.010	0.048±0.002
LHCII- AuNS@ TiO_2	173±9	0.450±0.018	0.581±0.058	0.045±0.004	0.035±0.003
LHCII-AgNP@TiO_2	208±11	0.435±0.010	0.587±0.040	0.053±0.004	0.044±0.004

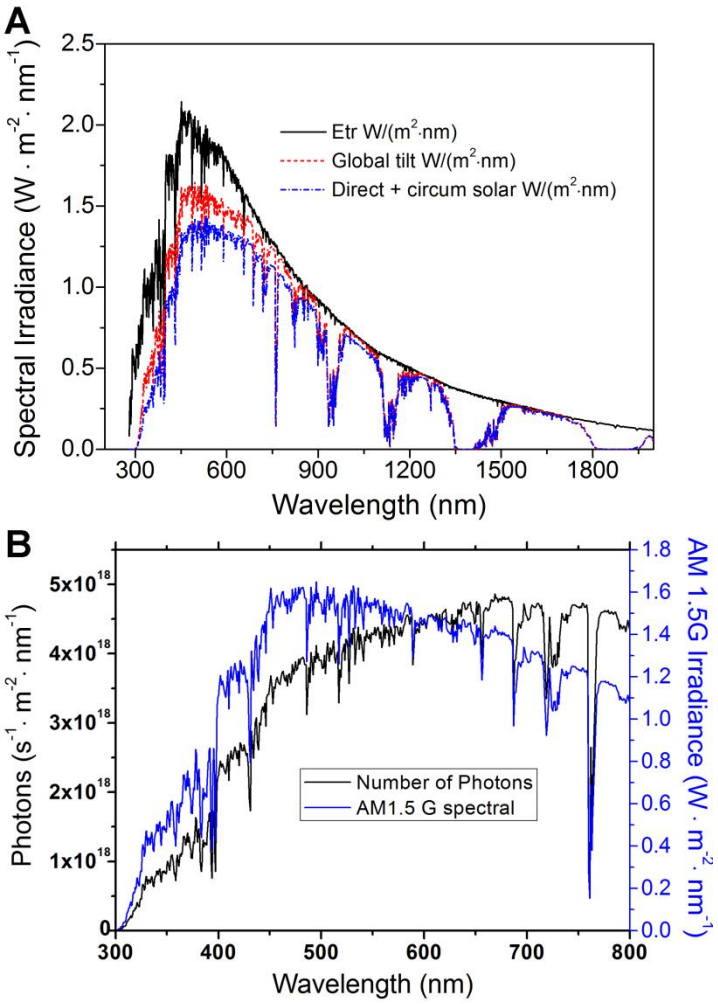

Figure B.8 The standard solar spectra.

(A) The standard solar spectra (from http://rredc.nrel.gov/solar/spectra/am1.5/ASTMG173/ASTMG173.html). The 1 sun AM1.5G standard is represented by the red curve. (B) The presentation of the AM1.5G spectrum in intensity with the unit of W/(m^2·nm) (blue line) and number of photons with the unit of s^{-1}·m^{-2}·nm^{-1} (black line). (Reprinted with permission from supplementary information Y. Yang, H. Gobeze, F. D'Souza, R. Jankowiak and J. Li, *Adv. Mater. Interfaces*, DOI: 10.1002/admi.201600371)

Appendix C - List of Publications and Presentations

PUBLICATIONS:

- **Yiqun Yang**, Judy Wu and Jun Li, Correlation of the Enhanced Photoconductance and Photovoltaic Properties of Core-Shell Au@TiO_2 Network, ***Applied Physics Letters***, submitted

- **Yiqun Yang**, Habtom Gobeze, Francis D'Souza, Ryszard Jankowiak and Jun Li, Plasmonic Enhancement of Biosolar Cells Employing Light Harvesting Complex II Incorporated with Core-Shell Metal@TiO_2 Nanoparticles, ***Advanced Materials Interfaces***, DOI: 10.1002/admi.201600371

- Gaind P. Pandey, Tao Liu, Emery Brown, **Yiqun Yang**, Yonghui Li, Xiuzhi Susan Sun, Yueping Fang and Jun Li, Mesoporous Hybrids of Reduced Graphene Oxide and Vanadium Pentoxide for Enhanced Performance in Lithium-Ion Batteries and Electrochemical Capacitors, ***ACS Applied Materials and Interfaces***, 2016, 8 (14), 9200-9210

- **Yiqun Yang**, Ryszard Jankowiak, Chen Lin, Krzysztof Pawlak, Michael Reus, Alfred R. Holzwarth, Jun Li, Effect of the LHCII Pigment-Protein Complex Aggregation on Photovoltaic Properties of Sensitized TiO_2 Solar Cells, ***Physical Chemistry Chemical Physics***, 2014, 16, 20856-20865

- Yicheng Zheng, Steven Klankowski, **Yiqun Yang**, Jun Li, Preparation and Characterization of TiO_2 Barrier Layers for Dye-Sensitized Solar Cells, ***ACS Applied Materials and Interfaces***, 2014, 6, 10679-10686

- Adam Kell, Ximao Feng, Chen Lin, **Yiqun Yang**, Ryszard Jankowiak, Charge-Transfer Character of the Low-Energy Chl *a* Q_y Absorption Band in Aggregated Light Harvesting Complexes II, ***The Journal of Physical Chemistry B***, 2014, 118 (23), 6086-6091

- Xunfu Zhou, Weijian Liu, Xiaoyuan Yu, Yingju Liu, Yueping Fang, Steven Klankowski, **Yiqun Yang**, James Emery Brown, and Jun Li, Tin Dioxide@Carbon Core-Shell Nanoarchitectures Anchored on Wrinkled Graphene for Ultrafast and Stable Lithium Storage, ***ACS Applied Materials and Interfaces***, 2014, 6 (10), 7434-7443

PRESENTATIONS

- **Yiqun Yang**, Adam Kell, Chen Lin, Michael Reus, Alfred R. Holzwarth, Jun Li, Ryszard Jankowiak; "On the charge-transfer character of the low-energy Chl *a* Qy absorption band in aggregated LHCII pigment–protein complexes: Effect of aggregation on photovoltaic properties of sensitized TiO2 solar cells", 248th ACS National Meeting, San Francisco, CA (2014)

- **Yiqun Yang**, Yichen Zheng, Steven Klankowski, Ryszard Jankowiak, Chen Lin, Krzysztof Pawlak, Michael Reus, Alfred R. Holzwarth, and Jun Li; "A Thin-film Dye-sensitized Solar Cell Platform to Tap into Photon Capture and Charge Transfer of Light Harvest Complexes", 49th Midwest Regional Meeting of ACS, Columbia, MO (2014)

- **Yiqun Yang**, Ryszard Jankowiak, Chen Lin, Alfred Holzwarth, and Jun Li; "The Effects of Light-Harvesting Complex II (LHCII) Structure on Photovoltaic Properties of Sensitized TiO2 Solar Cells", Kansas NSF EPSCoR Annual Meeting, Lawrence, KS (2013),

- **Yiqun Yang**, Ryszard Jankowiak, Chen Lin, Alfred Holzwarth, and Jun Li; "The Effects of Light-Harvesting Complex II (LHCII) Structure on Photovoltaic Properties of Sensitized TiO2 Solar Cells", Graduate Research Forum, Kansas State University, Manhattan, KS (2013)